AD772548

AD-772 548

WALL PRESSURE FLUCTUATIONS AT SMOOTH AND ROUGH SURFACES UNDER TURBULENT BOUNDARY LAYERS WITH FAVORABLE AND ADVERSE PRESSURE GRADIENTS

Thomas E. Burton

Massachusetts Institute of Technology

Prepared for:

Office of Naval Research

June 1973

DISTRIBUTED BY:

NTIS

National Technical Information Service
U. S. DEPARTMENT OF COMMERCE
5285 Port Royal Road, Springfield Va. 22151

DISCLAIMER NOTICE

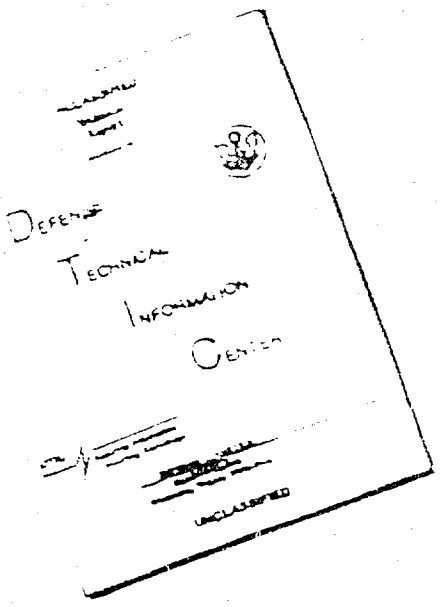

THIS DOCUMENT IS BEST QUALITY AVAILABLE. THE COPY FURNISHED TO DTIC CONTAINED A SIGNIFICANT NUMBER OF PAGES WHICH DO NOT REPRODUCE LEGIBLY.

REPRODUCED FROM
BEST AVAILABLE COPY

Unclassified
Security Classification

DOCUMENT CONTROL DATA - R & D

Security classification of title, body of abstract and indexing annotation must be entered when the overall report is classified)

1. ORIGINATING ACTIVITY (Corporate author)

Massachusetts Institute of Technology
Cambridge, Massachusetts 02139

2a. REPORT SECURITY CLASSIFICATION

Unclassified

2b. GROUP

3. REPORT TITLE

Wall Pressure Fluctuations at Smooth and Rough Surfaces Under Turbulent Boundary Layers with Favorable and Adverse Pressure Gradients

4. DESCRIPTIVE NOTES (Type of report and inclusive dates)

September 1971 through August 1972

5. AUTHOR(S) (First name, middle initial, last name)

Thomas E. Burton

6. REPORT DATE

June 1973

7a. TOTAL NO. OF PAGES

~~135~~ 138

7b. NO. OF REFS

30

8a. CONTRACT OR GRANT NO.

N00014-67-A-0204-0002

b. PROJECT NO.

SR 009 01 01

c.

d.

9a. ORIGINATOR'S REPORT NUMBER(S)

Acoustics and Vibration Laboratory
Report No. 70208-9

9b. OTHER REPORT NO(S) (Any other numbers that may be assigned this report)

10. DISTRIBUTION STATEMENT

Approved for public release; distribution unlimited.

11. SUPPLEMENTARY NOTES

12. SPONSORING MILITARY ACTIVITY

Naval Ship Research and Development Ctr.
Bethesda, Maryland 20034

13. ABSTRACT

Fluctuating wall pressures under turbulent boundary layers with favorable gradients were measured at both smooth and rough walls. Wall pressure intensity was found to vary in proportion to mean wall shear stress between no-gradient and favorable-gradient flows. The favorable gradient decreased longitudinal spatial decay rates and increased convection velocities; roughness had the opposite effects.

Adverse gradient boundary layers were also studied over smooth and rough walls. These flows were not self-preserving, and results are presented as functions of longitudinal position. The adverse gradient slowed convection velocities and increased longitudinal spatial decay rates. Pressure intensities were concentrated into a comparatively narrow band of frequencies. Pressure statistics were found to depend on local mean flow parameters and upstream flow conditions, but not on wall roughness.

DD FORM 1 NOV 65 1473 (PAGE 1)

1a

S/N 0102-014-6600

Security Classification

Unclassified

Security Classification

14 KEY WORDS	LINK A ROLE	LINK A WT	LINK B ROLE	LINK B WT	LINK C ROLE	LINK C WT
Boundary Layer						
Turbulence						
Aerodynamic Noise						
Wall Pressure Fluctuation						

DD FORM 1 NOV 65 1473 (BACK)

(PAGE 2)

ib

Security Classification

WALL PRESSURE FLUCTUATIONS AT SMOOTH AND ROUGH SURFACES UNDER TURBULENT BOUNDARY LAYERS WITH FAVORABLE AND ADVERSE PRESSURE GRADIENTS

by

Thomas E. Burton

ABSTRACT

Fluctuating wall pressures under turbulent boundary layers with favorable gradients were measured at both smooth and rough walls. Wall pressure intensity was found to vary in proportion to mean wall shear stress between no-gradient and favorable-gradient flows. The favorable gradient decreased longitudinal spatial decay rates and increased convection velocities; roughness had the opposite effects.

Adverse gradient boundary layers were also studied over smooth and rough walls. These flows were not self-preserving, and results are presented as functions of longitudinal position. The adverse gradient slowed convection velocities and increased longitudinal spatial decay rates. Pressure intensities were concentrated into a comparatively narrow band of frequencies. Pressure statistics were found to depend on local mean flow parameters and upstream flow conditions, but not on wall roughness.

TABLE OF CONTENTS

		Page
	Abstract	i
	Nomenclature	iii
I.	Introduction	1
	(A) Background	1
	(B) Experimental Facility	2
	(C) Quantities Measured	5
II.	Experimental Results and Discussion	8
	(A) Mean Flow Parameters	9
	(B) Broadband Statistics	16
	(C) Narrowband Statistics	34
III.	Conclusions	65
	Appendix--The Turbulent Momentum Integral Equation	68
	References	72
	Preface to the Figures	74
	Figures and Tables	75

NOMENCLATURE OF COMMONLY-USED SYMBOLS

C_f	friction factor: $C_f = 2\tau_w/(\rho\ U_\infty^2)$
H	shape factor, $H = \delta^*/\Theta$
k	wave number
$\bar{k}$	average wave number
$\bar{k}_g$	mean geometric roughness height
$p(x,t)$	instantaneous wall pressure fluctuation at position x and time t
$\overline{p^2}$	mean square pressure fluctuation
q, Q	freestream dynamic head, $(1/2)\rho\ U_\infty^2$
$R(r_1,r_3,\tau)$	space-time correlation of wall pressure, normalized so that $R(0,0,0) = 1$
Re_Θ	Reynolds number based upon momentum thickness: $Re_\Theta = U_\infty\ \Theta/\nu$
r	microphone separation vector, $r = (r_1,r_3)$
s	hotwire length
$U(y)$	mean velocity
U_c	convection velocity
U_g	group velocity
U_p	phase velocity
U_τ	friction velocity
U_∞	freestream velocity
u, v, w	longitudinal, normal, and lateral fluctuating velocity components
$\hat{u}$, $\hat{v}$, $\hat{w}$	root mean square fluctuating velocity components
x	streamwise coordinate
Δx	streamwise displacement: $\Delta x = x_2 - x_1$
y	normal coordinate
z	lateral (spanwise) coordinate

Δz	lateral displacement: $\Delta z = z_2 - z_1$
δ	boundary-layer thickness
$\delta_{.99}$	$U(y=\delta_{.99})/U_\infty = .99$
δ^*	displacement thickness
Θ	momentum thickness
ν	kinematic viscosity
ξ	nondimensional length scale, $dx = \delta^*(x)d\xi$
ρ	fluid density
τ	separation in time
τ_w	mean wall shear stress
$\Phi(\omega)$	pressure spectral density: $\int_{-\infty}^{+\infty} \Phi(\omega)d\omega = \overline{p^2}$
$\Phi(r,\omega)$	pressure cross spectral density: $\Phi(0,\omega) = \Phi(\omega)$
ω	radial frequency

CHAPTER I

INTRODUCTION

(A) BACKGROUND

This report is part of an effort to describe the nature of pressure fluctuations on panels under turbulent boundary layers so that panel responses may be predicted. P. Leehey (1969) has comprehensively reviewed this problem. Many experimenters have studied wall pressure fluctuations over smooth and rough walls. A particularly detailed study is that of Blake (1970). The effects of a freestream pressure gradient on the pressure statistics have been studied by Schloemer (1966) and Bradshaw (1967), among others. Schloemer studied both favorable and adverse gradients, and Bradshaw studied adverse gradients. This report combines the effects of wall roughness and freestream pressure gradient.

It is clear that a favorable gradient will reduce the thickness of the boundary layer. Schloemer found that the imposition of a favorable gradient reduced the displacement thickness by about a factor of five. Under these conditions, the effect of a roughened wall can be expected to be much more important in the favorable gradient case, as compared with the case with no gradient. This investigation used a flow with about the same favorable pressure gradient as that of Schloemer with a smooth wall. The flow geometry was held constant and roughened walls were substituted for the smooth ones, and the two sets of results were compared. The roughness used is identical with one used by Blake (1970) whose experiments were performed in the same facility as the current work.

The same roughness was used for both favorable and adverse gradient studies. Since the ratio of roughness size to boundary-layer thickness was expected to be much smaller with the adverse pressure gradient, a strong dependence on wall roughness seemed unlikely. More importantly, the author was not aware of any comprehensive studies of wall pressure fluctuations in the presence of very strong adverse gradients, where the flow is near or tending toward separation. For these reasons, it was decided to study a flow with adverse gradients much stronger than those of Schloemer, even if that caused the extra complication of flows whose properties depended upon longitudinal position. Again, both smooth and rough walls were studied and the results compared.

(B) EXPERIMENTAL FACILITY

All experiments were performed in the subsonic low-noise wind tunnel in the Acoustics and Vibration Laboratory of the Massachusetts Institute of Technology. A complete description of the facility was provided by Hanson (1969). The main components are the inlet, the flow straightener and screens, the contraction, the test section enclosed in an airtight blockhouse, the muffler-diffuser, and a variable-speed centrifugal blower. The blower is acoustically isolated from the test section by the muffler, and mechanically isolated by an air gap between the diffuser and the blower. Although the tunnel is of the open-flow type, the complete circuit is enclosed in a large quiet room of approximately uniform temperature, so that thermal gradients and resulting density variations and flow rotation are largely avoided.

Because of the airtight blockhouse surrounding the test section, open jets in the test section may be created. Figure 1 is a schematic of the test configurations used in this investigation. The closed test section is a rectangular duct, 15 inches on each side. In order to study the effects of favorable gradients, a two-dimensional baffle, as shown in the figure, was installed opposite the surface to be studied. The slope of the baffle in the test region was chosen so as to make pressure gradients approximately equal to those of Schloemer (1966). The baffle slope on the region of diverging flow was chosen to be gentle enough to prevent separation of the flow along the baffle. The tested surface was either rough or smooth. The smooth surface was formica, and rough surface was formed by cementing sand grains whose size varied randomly over narrow limits on wood planks in a random pattern. The resulting effect is like that of very coarse sandpaper. The sand grains had a mean height of about .09 inches. For a complete description of this roughened surface, see Blake (1970). In his report, Blake refers to this surface as D-L, standing for densely-packed large grains. The condition of the wall, either smooth or rough, was uniform from the downstream end of the contraction, where the boundary layer first became turbulent, all the way to the test section. Thus the boundary layer was in equilibrium just upstream of the region of converging flow. The flow reequilibrated quickly to the favorable gradient.

It was desired to study adverse pressure gradients of a considerably larger magnitude than those of Schloemer (1966), and it was judged that the baffle arrangement used to generate

favorable gradients would be unsatisfactory for strong adverse gradients because of possible flow separation from the baffle, and because of unacceptably high flow noise that might be present near the baffle. Figure 1 shows the configuration adopted instead. The bottom surface was fitted with a circular arc to allow the flow to diverge in the tested region. The radius of curvature of the arc was greater than 30 inches, large enough that centripetal acceleration around the arc can be neglected. The sides of the test section were extended as shown in the figure. A semiporous, blunt, two-dimensional collector, made of vermiculite surrounded by fiberglass, redirected the flow back into the channel. To minimize acoustic contamination from the collector, it was found advantageous to modify the collector so that its blunt leading edge was above the mean mass line of the jet, so that there was a tendency for some of the jet to spill out under the collector. Since the blockhouse containing the test section was airtight, this couldn't happen, and the pressure caused the mean streamlines in the open jet to curve upwards, as shown in the figure, so that the jet flow was more nearly aligned with the surface of the collector when it impinged upon that surface. It is believed that this curvature in the streamlines is partly responsible for the improved performance of the modified collector.

As with the favorable gradient cases, the boundary layer was self-similar over the smooth or rough wall just upstream of the gradient section. The flow did not become self-similar after the imposition of the adverse gradient, but rather tended toward separation. Strong adverse gradients were desired, but

flow separation at any point on the tested surface was avoided. It was anticipated that, for a given geometry, the rough-wall flow would have a greater tendency to separate so the roughened wall condition was studied first. The geometry was adjusted to eliminate any flow separation. Then the geometry was adjusted for the smooth study so that the nondimensional pressure gradient was about the same. The smooth-wall study required a larger angle of flow divergence, and the collector noise was more obtrusive. Wall pressures on the tested surface were found to be contaminated below 70 Hz ($\omega\delta^*/U_\infty \approx .2$) and had to be eliminated. Freestream rms turbulence levels above the tested boundary layer were always below 0.15% of the freestream velocity.

The temperature of the tunnel air was continually recorded. Its effects on the kinematic viscosity were built into the calculations. The variation of barometric pressure was negligible.

(C) QUANTITIES MEASURED

An attempt was made to measure all those quantities necessary to describe and explain the second-order wall pressure statistics. These measurements have been divided in this report into three major categories: mean parameters, broadband (in frequency) statistical results, and narrowband statistical results. The mean parameters include nondimensional freestream pressure gradients, mean velocity profiles, wall shear stress and friction factor, and related quantities. The broadband results include rms wall pressures, turbulent velocity intensity profiles, two-point wall-pressure correlations, broadband convection velocities, and pressure time-autocorrelations. The narrowband results include frequency spectra for both wall pres-

sure and turbulent velocities, narrowband two-point wall-pressure crosscorrelations, and narrowband convection velocities. Within each of the above-mentioned categories of data, a description of the instrumentation used in collection of the data, the experimental errors involved, and a discussion of the results are all included with the presentation of the data itself.

The crosscorrelation function is defined as follows:

$$R(r_1,r_3,\tau) \equiv \frac{\overline{p(x,z,t)\ p\ (x+r_1,z+r_3,t+\tau)}}{\left(\overline{p(x,z)^2}\cdot\overline{p(x+r_1,z+r_3)^2}\right)^{1/2}}$$

The crosscorrelation function is normalized to be unity when its arguments are all equal to zero. The normalization accommodates the possibility that pressure statistics are not homogeneous in x and z. The adverse gradient flows studied are, in fact, inhomogeneous in x. All flows are homogeneous in z.

Power cross-spectral density is defined as the time-frequency transform of the crosscorrelation:

$$2\pi\Phi(r_1,r_3,\omega) \equiv \left(\overline{p(x,z)^2}\ \overline{p\ (x+r_1,z+r_3)^2}\right)^{1/2} \int_{-\infty}^{+\infty} R(r_1,r_3,\tau)e^{i\omega\tau}d\tau \tag{1}$$

The cross-spectral density is not normalized on mean square pressure. It is complex quantity, and its phase can be written as follows:

$$\Phi \equiv |\Phi|e^{i\bar{k}\cdot r} \tag{2}$$

Equation (2) defines $\bar{k}$ as a function of r and ω. This representation of cross-spectral phase is useful to point up any wave-like nature of Φ when it occurs. The Fourier transform relation of equation (1) can be inverted and combined with equation (2) to obtain the following equation for the crosscorrelation:

$$\left(\overline{p(x,z)^2}\ \overline{p(x+r_1,z+r_3)^2}\right)^{1/2} R(r_1,r_3,\tau) = \int_{-\infty}^{+\infty} e^{i(\bar{k}\cdot r-\omega t)}\,d\omega \qquad (3)$$

Equation (3) is useful in assessing any oscillatory behavior of observed crosscorrelation functions.

CHAPTER II

EXPERIMENTAL RESULTS AND DISCUSSION

The boundary layers adjusted to the imposition of the favorable gradient and formed self-preserving layers in the tested region. No significant deviations in any mean parameter were found over a distance exceeding 10 boundary-layer displacement thicknesses. This feature of the favorable gradient flows is not due to any precise manipulation of the pressure gradient, but rather to the fact that the boundary layers were very thin in relation to the geometry of the wind tunnel and the baffle which induced the freestream pressure gradient. The self-similarity of the flow is also due to the fact that the changes that the boundary layer made in response to the imposition of the gradient were self-limiting; as the layer became thinner, the wall shear stress increased until the increased wall friction balanced the freestream pressure gradient. When this happened, the boundary layer reached a new equilibrium.

The adverse freestream pressure gradient flows were not self-similar, but tended toward separation with increasing streamwise distance. Therefore, all quantities measured were functions of the longitudinal coordinate. The origin x=0 was arbitrarily chosen to be the most upstream position at which data were taken for either of the adverse gradient flows. x=0 corresponds to about 6 inches downstream of the curved portion of the tested surface for all adverse gradient flows (see Figure 1). The nondimensional streamwise variable has been defined by $dx = \delta^*(x)d\xi$, and $\xi = 0$ when $x = 0$. This variable defines differential position in terms of the local boundary-layer

thickness. The smooth-wall data are superior to the rough-wall data for adverse freestream pressure gradient flows in that δ varies over a much wider range over the smooth wall, since the boundary layer is thinner.

For brevity, flows will be designated as FS (favorable smooth), FR (favorable rough), AS (adverse smooth), and AR (adverse rough) throughout the chapter.

(A) MEAN FLOW PARAMETERS

Since the favorable gradient flows were self-similar, the flows needed to be studied only at one longitudinal position.

The standard coordinate system is adopted, with x being the longitudinal (streamwise) coordinate, and y being the normal coordinate, defined to be zero at the wall and increasing into the boundary layer.

Mean flow parameters are displayed in Figures 2 through 8, and in Table 1. Figure 2 shows the boundary-layer profiles of the favorable gradient flows in law-of-the-wall form. Two flow speeds are shown for each of the two wall types. Most of the data were obtained with a flat-mouth tube with a width of .040 inches. Very near the wall a tube with a .020-inch width was used. Pressures were measured with a Betz manometer which could be accurately read to within .02 mm H_2O. The main errors in the profile measurement come not from errors in pressure determination, but rather from errors in probe positioning, which could have been as much as .01 inches, or about $y^+=25$. The smooth-wall data fall very nicely on the curve which defines the well-accepted law of the wall for turbulent boundary layers. The imposition of the favorable gradient did not have a

significant effect, except that the wake region of the flow, which would deviate from the logarithmic law, is apparently nonexistent. This feature of the profile is also present in the favorable gradient results of Schloemer (1966). Over the limited range of Reynolds numbers tested, no Reynolds number dependence was found. As can be seen in Figure 2, it was not possible to get data below $y^+=60$. Mean profiles were measured with both total head tubes and hot-wire anemometers. No significant differences between the two methods were found, and since the total head tube measurements are more accurate, they are the ones presented. It is possible that all measurements of position were biased by as much as 25 in y^+, but the scatter in the data is much less than that, as indicated in Figure 2. The rough-wall data also follow the law of the wall very well. The roughness caused a velocity defect which resulted in a much lower curve in Figure 2 than that for the smooth-wall data. These results are in quantitative agreement with Blake (1970). Here the very slight wake of the layer can be seen at about $y^+=8000$. The wake is less pronounced than that of Blake. The question of a bias in the positioning of the total head tube does not apply to the rough-wall measurements, because $y^+=0$ has been defined so as to make the data in Figure 2 follow a straight line as well as possible. This results in an apparent surface (y=0) which is about 1/3 $\bar{k}_g$ below the top of the roughness grains. For a full discussion of this procedure, see Burton (1971).

The favorable gradient profiles are replotted with outer variable scaling in Figure 3. Here some Reynolds number dependence is evident near the wall. This is expected, since the

wall region is better scaled on inner variables. The shape of smooth-wall profiles suggest that a viscous sublayer existed near the wall where the velocity varied rapidly with y, but the viscous sublayer was too thin to be investigated. Consistent with the results of other investigations (see, for example, Blake (1970)), there would appear to be no viscous sublayer over the roughened wall. Figure 3 shows clearly the difference between the smooth-wall flow, which is wakeless, and the rough-wall flow, whose wake region is apparent for y/δ^* of about 3 or 4.

Velocity profiles for the AS flows are shown in Figure 4, for three different longitudinal position. Between $\xi=0$ and $\xi=24.6$, there are very significant changes in profile shape, as indicated by the large change in shape factor. H=1.51 is not too different from that for most zero-gradient layers, and is quite similar to Schloemer's (1966) adverse gradient shape factor. Each of the profiles was logarithmic over a small region near the wall, but was generally wakelike, so that outer variable scaling is appropriate. Because the boundary layers were much thicker with the adverse gradient, probe positioning was not a significant source of error and the profiles are quite accurate. It is expected that there is a viscous sublayer very near the smooth wall, but it did not thicken along with the rest of the layer, and it was too small to investigate. The very thin viscous sublayer is probably caused by increased turbulent motion near the wall (see section B of this chapter).

Profiles of flows over the rough wall are shown in Figure 5. The curves are an average of those obtained at 80 ft/sec and 160 ft/sec. No significant differences between the two speeds

were found. These flows were much different from those over the smooth wall. Even the most upstream station, x=0, shows a shape factor which exceeds that of the most downstream point in the flow over a smooth wall. The shape factor reaches a high of 2.93. H=3 corresponds to a linear profile, and H greater than 3 implies an inflection or separation. There were no inflectional profiles in the region of measurement, although profile number 3 comes very close.

Table 1 summarizes the mean quantities measured. U_∞ is evaluated at x=0. Most of the AS flow measurements were made at 100 ft/sec, since this speed gave pressure data over a wider useful frequency range than others. Other combinations of wall type and gradient type were investigated with at least two flow speeds. Pressure gradients have been nondimensionalized on both wall shear stress and freestream dynamic head. Schloemer (1966) used wall stress scaling, and his nondimensional favorable gradient was -.36, midway between the values in this report for smooth and rough walls. As mentioned in the introduction, it was desired to measure favorable gradients on the same order as those of Schloemer. If wall stress scaling is also used to compare adverse gradients, then the gradients here are 5 to 10 times those of Schloemer. However, wall stress scaling is inappropriate in the case of rapidly growing boundary layers, as can be seen from the integrated momentum equation:

$$\tau_w + \delta^* \frac{dp}{dx} = \rho \frac{d}{dx} (U_\infty^2 \Theta) \qquad (4)$$

For favorable gradient flow, the two terms in the left ember of (4) are of equal order, and their ratio is a valid measure of

the magnitude of the pressure gradient. But in the adverse gradient cases studied here, the wall shear stress is very small and the pressure gradient term is of the same order as the right member of the equation. Therefore, it makes more sense to scale such gradients on freestream head. On the basis of this scaling, the adverse gradient reported here is 4 to 5 times that of Schloemer. It should be noted that τ_w and q are functions of x. q_o is evaluated at x=0.

Equation (4) is exact for steady (nonturbulent) two-dimensional mean flows on which three-dimensional turbulence is superimposed. Such flows are of interest here. Equation (4) is a sufficiently good approximation to the exact description of the favorable gradient flows for two reasons. Firstly, turbulent velocity magnitudes are much smaller than mean velocity magnitudes, so that the errors that turbulent motion cause in equation (4) are relatively small. Secondly, as was pointed out in the previous paragraph, τ_w and $\delta^* dp/dx$ are of the same order. Thus the errors due to unsteady flows are indeed small compared to τ_w. This reasoning applies only to the FS and FR flows; neither reason holds in the cases of AS and AR flows. Turbulence magnitudes are much higher in relation to mean flow magnitudes, and also τ_w is much smaller than the other terms in equation (4). Under these circumstances, equation (4) is in serious error. The appendix of this report discusses this problem and shows how equation (4) was modified in the case of adverse gradient flows to give better estimates of the wall shear stress. Because the term τ_w is relatively small in equation (4) for AS and AR flows, the uncertainty in estimating it is quite

high. This fact is an additional reason to scale pressures on freestream head rather than wall shear stress, for flows with adverse pressure gradients.

Re_Θ values are slightly larger than those of Schloemer, and comparable to those of Blake.

$\bar{k}_g$ is an average roughness height, obtained by averaging a large number of random measurements of sand grain diameter.

r/δ^* gives the ratio of the effective radius of the pressure transducer to the boundary-layer displacement thickness. This number is large in the favorable gradient cases, especially for smooth walls, because the gradient makes the layer so thin. It is this fact which will prevent study of stronger favorable gradients with the same instrumentation, since even the current investigation was limited by the experimental difficulties of small length scales. The transducer size has also been scaled on inner parameters. Emmerling (1972) and others have concluded that inner-scaled transducer size is also important in assessing the debilitating effect of finite transducer size.

Figure 6 shows how Θ, δ^*, and H vary with x or ξ for AS flow. Figure 7 shows how nondimensional pressure gradient depended on x or ξ. It also gives three estimates of the skin friction factor. Note that δ^* and Q are both functions of x. The cross-hatched area is the estimate (and estimated error limits) formed from equation (4), modified as explained in the appendix. The line labeled LT is from an empirical formula of Ludwig and Tillman (1950) which estimates the friction factor from the Reynolds number and the shape factor:

$$C_f/2 = \frac{.123}{10^{.678H} Re_\theta^{.268}}$$

The AS flow profile had a small logarithmic region near the wall. If one asserts that this region obeys von Kármàn's Law of the Wall with von Kármàn's constant κ=.41 (this choice of κ agrees with the equations on Figure 2), then one can infer the friction velocity and wall shear stress. The estimate of the friction factor using this method is labeled CP. The methods are not in agreement. Although the momentum integral method approach is the most rigorous, none of the three can be considered very reliable.

Figure 8 applies to AR flows. These quantities are an average of those obtained for the two flow speeds measured. Again, the cross-hatched region estimates the friction factor from equation (4). The solid line is the estimate of Ludwig and Tillman. No estimate from the logarithmic region could be made for AR flows because it was nonexistent.

In the FS and FR flows the logarithmic region of the layers extended throughout most of the layer, as can be seen in Figure 2. The roughness had a tremendous effect on the layer, because the geometrical size of the sand grains was larger than the displacement thickness of the FS layer. The FR layer was considerably thickened with respect to the FS layer, and there was a wake region which the FS layer seemed to lack. This latter difference accounts for the difference in H between the two cases. It is almost obvious that roughness will increase pressure intensity; but whether or not intensity will keep pace with the wall shearing stress is not clear from the foregoing discussion. The AS and AR flows are functions of x, and the mean parameters vary

widely, especially in the case of AS flows. However, the proportional changes in any of the mean quantities over one boundary-layer thickness ($\Delta\xi=1$) is never more than about 10%, and it is possible that the flow may be profitably viewed as locally homogeneous in the streamwise direction. As a function of x, the adverse gradient flows tended toward separation, as the generally decreasing estimates of friction factor indicate. The upstream part of the AS flow might be expected to behave similarly to a no-gradient flow, whereas the downstream portion of this flow, and most of the AR flow, might behave more like a free wake, since the effect of the wall should be rather small. In fact, because of the small shearing stresses, and because the AS and AR flows have thick layers in comparison to the roughness size, it is unlikely that the local roughness in the tested region had much effect. However, the AR boundary layer profile was retarded coming into the adverse gradient region. This caused it to react much more strongly to the adverse gradient, even though the angle of divergence was less than that for AS flow.

(B) BROADBAND STATISTICS

Wall pressure intensity--Wall pressure fluctuations were measured with Brüel and Kjaer type 4138 microphones with circular diaphragms of 1/16-in radius. The microphones were mounted flush with the surface of the wood board on which the sand was cemented.) The diaphragms were covered with caps with holes drilled through their centers of 1/30-in diameter. The diameter of these holes, referred to as d in this report, is the effective diameter of the transducers. The airspace between the diaphragm

and the cap of a microphone resonates with a fundamental frequency of about 17 kHz. The microphones have a flat ($\pm$7%) frequency response between 20 Hz and 14 kHz with the caps in place, and they were calibrated at 250 Hz to within 3% with a type 4220 Brüel and Kjaer pistonphone. Frequencies below 20 Hz and above 14 kHz were always filtered out of the data. RMS levels were measured with a Brüel and Kjaer type 2416 True RMS Meter, accurate $\pm$3%.

Total rms wall pressures are given in Table 1. FS flows had a higher rms pressure than Blake's (1970) no-gradient flows when scaled on dynamic head, but lower when scaled on wall shearing stress. As will be seen from the next section, considerable power is lost in the higher frequencies due to the finite size of the transducer or the finite high-frequency response of the transducer. The amount of power lost is greater for thinner boundary layers and for larger transducers. The FR flows, with a smaller ratio of r/δ^*, show a higher rms pressure scaled on shear stress. Schloemer had larger values of r/δ^* than those of the current investigation, and his values of p_{rms}/τ_w are smaller than those of this experiment, for both no-gradient and favorable gradient flows. It is likely that, if all the energy were measured, the rms pressure would be a constant multiple of the wall shear stress for varying favorable gradients, at least up to the magnitude of the gradients studied by Schloemer and the author. This constant multiple is probably about 3.5 over the smooth wall, and 2.9 over the rough wall, using the no-gradient results of Blake (1970).

Adverse pressure gradients are better scaled on freestream

head, rather than mean wall shear stress, since the values of shear stress are inaccurate. Another reason for not using wall stress scaling is that the AS and AR flows are wakelike and do not seem to be strongly affected by the wall. Neither Schloemer nor the author had as much experimental trouble getting broadband pressure data with adverse gradient, because the intensities were confined to a narrower frequency range. However, pressure crosscorrelation determined that the AS wall pressures were contaminated with acoustic noise below 70 Hz. Frequencies below 70 Hz were eliminated from the data. Removal of these frequencies reduced the total intensity, but never more than 15%. For the same reason, wall pressure data had to be limited to frequencies above 40 Hz with AR flows. This limitation had a negligible effect on the measured pressure intensity. The AS flow had about the same rms pressure level as Schloemer's. The AR flow's value was significantly higher. This result can be attributed to higher turbulent intensities over the roughened wall. It is not an effect of the condition of the wall in the tested region. Rather it is an indirect effect: the roughness retarded the flow upstream of the test section. This affected the mean velocity profile of the whole layer in the test section, giving a much higher shape factor in the AR flow as compared with the AS flow. This AR flow developed higher turbulent intensities, as described below, which are responsible for the higher rms wall pressures.

Table 1 gives a range of values of rms pressure as a function of displacement. Note that q_o is not a function of x. Considering the large changes with x of the mean parameters,

it is surprising that the variation of rms pressure is so slight in the AS and AR flows. Fluctuating pressures measured at several stations are listed in Table 2. When rms pressures are scaled on the variable q(x), they appear to increase with x; this is an artifact of the decreasing dynamic head. The pressure does not scale on local mean parameters, but tends to be constant. This surprising fact suggests that what was measured was actually acoustic contamination. Two-point pressure correlations, reported later in this section, eliminate this possibility. The data for the AR flows are not so convincing because the measurement stations do not span as large a range of ξ.

Turbulent velocity intensities--Turbulent velocities were measured with hot-wire x-probes and Disa 55D09 constant-temperature anemometers with Disa 55D15 linearizers. Longitudinal turbulent velocities were also measured with single-wire probes. The probe wires are about .03 inches long, and the two wires in the x-probe are separated by about .02 inches. This size reduces the sensitivity of the wires to small-scale disturbances, a problem in the FS and FR flows, in which the length scales are quite small. No attempt was made to correct for this deficiency, but it is further discussed in section C below. The greatest error in the velocity measurements is apt to be associated with the standard methods of extracting velocity components with an x-probe. This method, subtracting and adding signals of the oblique wires to obtain normal and streamwise velocities, relies on the assumption that turbulent velocities are small compared to the local mean flow velocity. The order of the error associated with this assumption is $\hat{u}(y)/U(y)$.

The rms velocity, or turbulent intensity, profiles are shown for the FS flows in Figure 9. The results of Blake (1970), measured with almost the same equipment, provide a no-gradient comparison. The curves attributed to Blake have been faired by the author from data of Blake. The longitudinal intensities are reduced by the favorable gradient. The same result was obtained by Schloemer (compare curves 3 and 4, which Schloemer faired through his own data). However, the normal intensities are not reduced nearly so much. It would appear that the assumption of local isotropy, which Schloemer had to make for lack of data, is not justified in the comparison of favorable and no-gradient data. The turbulent intensities are more isotropic in the FS case than in the no-gradient case. No spanwise intensities were measured in the FS and FR cases. For both $\hat{u}$ and $\hat{v}$, the data show a slight increase in outer wake intensity at the higher Reynolds number. Turbulent intensities for flows with no gradient or favorable gradient are consistently lower for Schloemer than for the author or Blake.

The same quantities are displayed for FR flows in Figure 10. Again, there is a tendency for more isotropy in the favorable gradient case. The longitudinal intensity is reduced sharply by the gradient, but the normal intensity is actually increased near the wall. Further away from the wall, however, it is sharply reduced. Again, the higher Reynolds numbers seem to have brought higher intensities near the outer edge of the boundary layer.

Turbulent intensities for AS flows are shown in Figure 11. Intensity is now scaled on freestream velocity rather than shear-

stress velocity. Longitudinal intensities are shown for two extreme values of x. At the upstream station, the profile shape is not too different from that of Blake, shown in Figure 9. And at the other end, there has been a considerable redistribution of energy away from the wall, and the total amount of turbulent energy in the profile is higher. Schloemer's adverse gradient intensity is much lower, perhaps in part because his gradient was not as strong. Also shown for comparison is the profile of Bradshaw (1966) for a self-preserving flow in an adverse pressure gradient. His result is more like the author's, except that the curve peaks at a lower value, farther away from the wall. A similar comment applies to a comparison of normal intensities of Bradshaw and the author. It cannot be fairly stated that these differences are the differences of a self-similar flow versus a non-self-similar flow, since Schloemer's flow was also self-similar, yet his longitudinal intensity profile is more similar in shape to the author's than it is to Bradshaw's. Note the fact that Bradshaw found the spanwise intensity to be midway between the other two in magnitude. The author did not measure spanwise intensities for AS flows.

The intensity profiles for AR flows are shown in Figure 12. The longitudinal AR intensity at both stations follows the pattern of the AS longitudinal intensity at the downstream station: the profile peaks about where $U(y)/U_\infty=1/2$. The longitudinal profile is more highly peaked at the downstream station. Note that the shape factor H is quite high for both of these measurement stations. All three components of turbulent intensity were measured at the downstream station. The spanwise intensity is

midway between the longitudinal and normal intensities in magnitude, the same as in Bradshaw's measurements over smooth walls. For the mean velocity profiles with shape factors greater than about 2, all three intensities would seem to have approximately the same profile shape, although the longitudinal intensity is always the largest of the three. It may also be noted that, for velocities with a large shape factor, the region where $U(y)/U_\infty$ is about 1/2 is also a region where the velocity profile is almost linear. This fact raises the possibility that local instantaneous inflections may develop in the velocity profile, resulting in inviscid instabilities and higher intensities.

Spatial crosscorrelations--Many two-point space-time correlations of wall pressure were measured. The correlations have been normalized by the product of the rms pressures at the two points $[\overline{(p(x)p(x+r))}/(p_{rms}(x)p_{rms}(x+r))]$ so that the normalized correlation is always unity when its arguments are all zero. Some of the results are shown in Figures 13 through 22. Correlations were performed with two Brüel and Kjaer model 4138 1/8-in microphones and a Princeton Applied Research (PAR) model 100 correlator. The microphones had the same phase response to within 10° between 20 Hz and 14 kHz. Power at other frequencies was removed with a pair of Khron-hite model 330 bandpass filters. These filters were always adjusted for identical ($\pm 3°$) phase response before use. This could be done by fine-tuning the passing frequencies of one of the units until its phase response matched that of the other unit. Statistical errors associated with the finite averaging time of the correlator were the dominant errors in measurement. The correlator has an exponential

averager with a time constant of 50 seconds. Assuming the pressure signals to be gaussianly distributed, the 70% confidence limits of the normalized correlations are $\pm 1/\sqrt{2BT}$, where T is 50 seconds and B is the approximate bandwidth of the pressure signal. The favorable gradient pressures were spread over the whole frequency range of 20 Hz to 14 kHz, giving an approximate 70% confidence limit spread of $\pm .0013$. This result only holds when the sampling rate of the correlator, which is variable, was greater than about 30,000 samples per second. The correlator is constructed so as to require a lower sampling rate when a longer time delay between the two correlated signals is desired. At worst, the sampling rate was depressed to 1000 samples/sec, for FS and FR flows. To prevent errors due to insufficient sampling, all frequencies above 500 Hz had to be removed in this worst case. This gives a worst-case 70% confidence tolerance of approximately $\pm .004$, for these flows. As will be seen in section C, the AS and AR wall pressures were more restricted in frequency. The approximate bandwidth B is about 250 Hz in the worst case, giving $\pm .007$ for the 70% confidence limits. A more reliable estimate of the statistical error of the correlator is obtained by forming successive correlations and checking for repeatability. Observed confidence limits may be established in this manner. Figures 13 through 22 contain no data for which the 70% confidence limits (either calculated or observed) were larger than about one-third the observed correlation level. The exception to this rule is that contours of zero correlation are sometimes included. Such contours are always flanked by contours of opposite sign and sufficient magnitude to satisfy the criteria laid down above.

Figures 13 through 16 show lines of constant correlation. The abscissa and ordinate are separations of one transducer relative to the other. Spot checks for negative values of the ordinate verified that the contours, as expected, are symmetric with respect to the Δx axis, so that only one quadrant needed to be shown. The FS and FR flows are virtually independent of x, and so their contours are symmetric with respect to the Δz axis as well. Figure 13 compares contours for the FS flow, at 120 ft/sec, with no-gradient flow, as measured by Blake (1970), and extended to include oblique separations by the author. Figure 13a is contours with no time delay, while in Figure 13b the convecting correlation contours are plotted. These contours are obtained by showing the maximum (positive) correlation observed as a function of time, when observing a space-time correlation between two points on the wall, of fixed positions. This procedure recognizes the observed fact that fluctuating disturbances propagate longitudinally, so that two-point correlations between points which are longitudinally separated should be much higher if one delays the signal from the upstream transducer to account for the transit time of the convecting disturbance. Where the longitudinal separation of the two measurement points is zero, the convecting correlation is the same as the purely spatial one. Thus, for example, the contours of Figures 13a and 13b are the same near $\Delta x=0$. Figure 13 illustrates an experimental problem: getting the two microphones close enough together relative to δ^* when the boundary layer is so thin. It was not possible to get closer than about $3\delta^*$ for the FS flows. The following observations can be made in comparing the solid and dashed curves of Figure 13a. The contours are more nearly

elliptical for the FS flow. That is, the solid contours have less of a tendency to curve away from the Δz axis for large Δx. Otherwise, the two sets of curves are quite similar, suggesting that δ^* is an appropriate scale for comparison. The negative correlation contours for larger values of Δx suggest disturbances oscillating in the x-direction. Consider what this means in terms of equation (3) in Chapter I. The variable vector x can be ignored for FS flows because they are homogeneous in the (x,z) plane. $\tau=0$, and the vector r has the components (Δx, Δz) in the notation of Figure 13. Φ is even in the lateral coordinate. The vector $\bar{k}$ is probably aligned with the longitudinal axis for all frequencies because the correlation is symmetric in the Δx-axis, but one can't be sure from the broadband data alone. Oscillation comes from the term $\exp(\bar{k}\cdot r)$, and it is so quickly damped because $\bar{k}$ is a strong function of ω, and waves of different frequency therefore destructively interfere. The oscillations are more nearly confined to the Δx-axis with no-gradient flows. If the wave packets were frozen, then the convecting contours would all be horizontal lines. For small values of x, this is seen to be a good approximation except for the contours of very high correlation which are of very small extent due to viscous dissipation. It appears from Figure 13b that the FS flow decays a bit more slowly in time than the no-gradient flow. This suggests that $\Phi(r,\omega)$ decays more slowly with r_1/δ^*, at typical values of ω. One might also expect that Φ might decay with increasing r_2/δ^* at about the same rate in both the FS and no-gradient flows. It is expected that increased viscous dissipation, not accounted for with displacement thickness scaling,

would cause the convecting contours to be closer to the Δz axis for the smaller separations. This effect could not be measured because sufficiently small separations could not be obtained.

Figure 14 compares FR flows with no-gradient rough flows. Figures 13a and 14a show almost exactly the same effects. However, Figure 14b does not indicate that convecting decay is slower over rough walls with the imposition of a favorable gradient. In fact, it seems to be slightly faster at the smaller separations. This differs from the smooth-wall result shown in Figure 13b. This result suggests that the longitudinal cross-spectral density has about the same dependence on r_1/δ^* for both gradients over rough walls.

Contours for AS flows are shown in Figure 15. Note the change in scale from Figures 13 and 14. The boundary layer was not longitudinally homogeneous, and it cannot be assumed that the contours shown have mirror images across the Δz axis. Here, δ^* was evaluated at the local origin $\Delta x=\Delta z=0$, and held independent of Δx and Δz. Two different origins were used: the upstream (U) and the downstream (D) origins. δ^* is different for the two origins. In both Figures 15a and 15b, one can see that the correlation at lateral separations is much greater for the AS flow. This probably reflects higher cross-spectral density magnitudes at lateral separations at typical frequencies. The contours for the AS flow measured at the upstream origin (dashed line) are similar to the no-gradient contours (dashed line in Figure 13a). The downstream measurement of the AS flow (solid line in Figure 15a) differs from the upstream measurement in two principal ways. First, the longitudinal correlation decays far more rapidly, and second, the correlation is far more oscilla-

tory, as can be seen by the existence of the -.2 contour line. Going back to equation (4), the stronger oscillations suggest that $\bar{k}(\omega)$ does not vary so much over the integral in that equation, for the flow over the AS downstream measurement point. This could be due either to $\bar{k}$ being a weak function of ω, or that Φ is significantly different from zero only for a small range of ω, and hence $\bar{k}$. More will be said on this matter in section C. The AS convecting contours are shown in Figure 15b. They show that the convecting turbulence decays faster with adverse gradient. Interestingly, the differences between upstream and downstream measurement results are not as great in Figure 15b as they are in Figure 15a. Decay is a bit faster at short distance, but a bit slower at longer distances. This suggests that the cross-spectral density decays with r_1/δ^* at about the same rate at both ends of the layer, so that outer variable scaling accounts for most of the difference between upstream and downstream, as far as Figure 15b goes. In Figure 15a, the solid and dashed curves would have been more similar if the longitudinal displacement Δx had not been normalized by $\delta^*(x)$, which is much larger at the downstream origin. It is possible that there is some mechanism that has maintained a constant eddy size in the AS flow.

The AR flow contours are shown in Figure 16. The boundary layer was so thick, and the scales were therefore so long, that measurements from just one origin covered all of the longitudinal extent of the test region. Therefore, it made no sense to try to compare spatial correlations with two different origins. The correlations for spanwise separations decay even more slowly than those of the downstream AS flow, but the behavior as a func-

tion of Δx is quite similar to the upstream AS flow. Clearly, the behavior of the adverse gradient spatial correlations is not a simple function of H or the local mean flow conditions, but rather is a function of both local mean flow conditions and the upstream flow. The AS flow began upstream ($\xi=0$) with a shape factor and a longitudinal intensity profile which is not too different from no-gradient flows, and changed fundamentally as a function of x. The AR flow began as a retarded flow with a high shape factor and a peaked longitudinal intensity profile, which changed only qualitatively as a function of x. The higher lateral correlations seem to be characteristic of the rough-wall flow, and are probably caused by the condition of the flow at the onset of the adverse gradient. This conclusion results from the observation that even as the shape factor increases in the AS flow the lateral correlations do not broaden; they do not, in other words, approach the correlations of the AR flow, which has, among other differences, an even higher shape factor than at any position in the AS flow. The position of the contours near the x-axis is not explained on the basis of local mean flow either. The AR flow, with its high shape factor, behaves like the upstream AS flow, with its low shape factor. The AS flow deviates from the no-gradient flows much more than the AR flow. This is not easy to rationalize. Figure 16L shows that the longitudinal decay of the correlation, and probably the cross-spectral density, is very gradual in the AR flow at typical frequencies.

At this point it should be noted that the cross-spectral density has been discussed as a function of r/δ^*. In section C

below, it is discussed in terms of $\bar{k}_1 \cdot r$, where $\bar{k}_1$ is the longitudinal component of $\bar{k}$. The results will be different.

Convection velocities--When Figures 13b, 14b, 15b and 16b were being prepared, the correlation was maximized in time for each longitudinal displacement Δx. Let this time be labeled $\tau_m(\Delta x)$. Then a convection velocity may be defined by $U_c = \Delta x/\tau_m$. These velocities may be thought of as group velocities because they are defined in terms of the rate at which the total wave packets propagate, that is, the rate at which turbulent pressure energy propagates. These velocities are plotted as a function of longitudinal separation in Figures 17 and 18. Figure 17 applies to FS and FR flows, and also shows the no-gradient results of Blake and Schloemer for comparison. There is little Reynolds number dependence, as one would expect. For all separations, velocities are slightly higher than those for no-gradient flows. For most separations, agreement with Schloemer is excellent. As Schloemer has explained, the higher convection velocities are due to the fact that mean velocities are higher in the FS and FR flows than in the no-gradient flows throughout the boundary layer, as evidenced by the lower shape factors. This conclusion holds for both smooth and rough walls.

Figure 18 shows broadband convection velocities for the adverse gradient flows. Figures 18a and 18b pertain to the AS flow, and to Figure 15. Figure 18a corresponds to the dashed lines in Figure 15, and the upstream origin; Figure 18b goes with the solid lines and the downstream origin. The results of Schloemer are shown dashed in Figure 18a. Separations which

were strictly longitudinal are marked with x's. These velocities are lower than Schloemer's at the upstream measurement point, and even lower at the downstream point. This is undoubtedly due to the fact that the AS flow was more retarded than Schloemer's, as indicated by the larger shape factors for the AS flow. Velocities are smaller for smaller separations, as are Schloemer's. This is probably due to the faster decay of the smaller disturbances, which are closer to the wall and therefore travel more slowly. At larger separations, mainly large, faster-moving disturbances are left. For data marked with circles, the indicated streamwise separation was accompanied by an equal spanwise separation. It is important to note that only the longitudinal component of the velocities measured between diagonally-separated points is shown here, not the magnitude of the convection velocity, which was larger by a factor of $\sqrt{2}$. It is the longitudinal component of these velocities which is larger than the velocities of strictly longitudinally-separated points, when separations of equal magnitude in the longitudinal direction are compared, as they are in Figure 18. Not only are the velocities for diagonally-spaced points larger, but, at their largest, they exceed by a significant amount the large separation limit of the velocities for strictly longitudinal displacements. There are two obvious physical explanations for this result. One is that at large $\Delta\xi$ the disturbances which are left are not the largest and the fastest; perhaps the longest lasting are intermediate in size and speed. The diagonal spacing would discriminate against all but the largest eddies because only they would be correlated over the spanwise component of the separation. This is especially

true of the large diagonal spacings. If all this were true, then the large diagonal spacings might have velocities even higher than those of the largest, strictly streamwise separations. The other possible explanation is that there are wave packets moving obliquely in the (x,z) plane, which move faster than the mean flow, and which do not correlate well in the direction perpendicular to their direction of propagation so that they are not readily detected by correlating points which are separated purely streamwise or purely spanwise. This second possibility is further discussed in section C of this chapter. The AR velocities are shown in Figures 18c and 18d. Results are similar to Figures 18a and 18b except that velocities are generally lower, reflecting the lower mean velocities in the rough-wall boundary layers.

For favorable gradient flows, diagonally-spaced correlations gave the same convection velocities as purely longitudinally-spaced correlations.

Time autocorrelations--The last set of broadband measurements to be reported is the time autocorrelations of wall pressure, Figures 19 through 22. Figure 19 compares autocorrelations of FS and no-gradient flows. Except for large times, the two curves collapse well on outer variable scaling. The symbols are data transplanted from the solid lines of Figure 13a, using the convection velocities shown in Figure 17. If the calculated convection velocities actually give the rate at which disturbances propagate, and if these disturbances are approximately frozen, that is, if they do not decay appreciably in the time it takes for them to traverse the distance $\Delta x = \tau U_c$, then the x's

would fall approximately on the solid curve. The comparison in Figure 19 is not very enlightening because of the lack of data at small separations.

Figure 20 compares FR flow with no-gradient rough-wall flow. Again, outer variable scaling accounts well for the differences between the two flows. The check on convection velocities and frozen turbulence is slightly more convincing here. Note that the correlations appear to drop more quickly from 1 in the FR flow case than in the FS case. This is an artifact, caused by the more severe high-frequency limitations imposed by the experimental apparatus in the FS flows, due to the extremely thin boundary layers. This artificial difference illustrates why correlation microscales, formed by studying the detailed shape of the curves near the origin, are often not useful numbers. They define the limits of the apparatus, rather than some physical aspect of the flow.

Figure 21 shows the time autocorrelations for the AS flow. Five curves correspond to different longitudinal measurement positions. These curves, perhaps more than any others, show how much the AS flow changes along the streamwise direction. Curve 1 is similar to those in Figures 19 and 20, while successive curves in Figure 21 become more oscillatory, suggesting that more and more power is being concentrated in a comparatively narrow band of frequencies centered near $\omega\delta^*/U_\infty = .3$ or so. This conclusion is quantitatively verified in section C, where wall pressure spectra are displayed. The circles use the dashed data from Figure 15a and the convection velocities from Figure 18a. The x's use the solid lines from Figure 15a and the

convection velocities from Figure 18b. The convection velocities varied considerably from point to point. Note that the correspondence of circles with curves 1 and 2, which refer to approximately the same longitudinal location, is decent; but the x's are a bit too close to the abscissa in comparison to curves 4 and 5 to which they should approximately correspond. This indicates significant decay of the disturbances over one wavelength, and is reflected in lower longitudinal cross-spectral densities when they are plotted against $\bar{k}_1 r$, as they are in section C.

Figure 22 shows the time autocorrelation for the AR flow. The measurement points were not distributed over enough longitudinal distance to show any changes in the curve. This means that outer variable scaling is adequate to compensate for the changes that occurred. Only the curves which correspond to the minimum and maximum values of ξ are presented, and they are virtually identical. The x's come from Figure 16a with convection velocities from Figure 18c. The lack of fit between the curves and the x's is similar to the case of Figure 21, and for the same reason.

The discrete symbols on these graphs are compared with the curves on the basis of a convection velocity, U_c, which differs from the acoustic speed by a factor of at least 7 for all data shown. If the dominant source of wall pressure had been acoustic waves, then the discrete symbols on Figures 21 and 22 would have described a virtually straight horizontal line at R=1.

Additionally, significant traveling acoustic wave contribution to the fluctuating wall pressure power (at least 1% of the

total) would have resulted in detectable crosscorrelation maxima at the time delays equal to the separation divided by the sound speed. No such maxima were detected. For these reasons, it is concluded that acoustic contamination of the adverse gradient pressure data was not present in significant quantity.

(C) NARROWBAND STATISTICS

All spectra are defined as even functions of frequency. Thus $\overline{p^2} = \int_{-\infty}^{\infty} \Phi(\omega)\, d\omega$. Autospectra were obtained with one of two machines. The favorable gradient work was done with a Brüel and Kjaer type 2107 wave analyzer which has a range of 20 to 20,000 Hz, which measured the amount of power in proportional bands of 6% width as a continuous function of frequency. The pressure spectra were not limited by the range of the analyzer since the range of the microphones was less. On the other hand, the hot-wire anemometers were useful to 35,000 Hz and, although their finite physical size degraded the signal at the higher frequencies, it still would have been useful to have the spectral data to 35 kHz. Between the time that the FS and FR flows were investigated and the time that the AS and AR flows were done, a Federal Scientific model UA-15A real-time analyzer and spectrum averager was purchased. In addition to being much faster, this instrument allows analysis to 50,000 Hz. Therefore, turbulent velocity spectra convey a much wider frequency range for AS and AR flows. The Federal Scientific machine measured power in each of 500 equal bands between 0 Hz and the upper limit set by the user. Both the Brüel and Kjaer and the Federal Scientific machines were capable of enough time averaging so that 70% confidence could be set at 3% of the measured value, which

exceeds the linearity and repeatability of the microphones which were used, so that the analyzers did not contribute significantly to errors in spectrum shape. The exception to this is that 70% confidence limits rose to ±5% when using the Brüel and Kjaer unit at the very lowest frequencies where the proportional bandwidths were extremely narrow. In this case, broader bandwidths were used and the results compared. No discrepancies occurred. Both analyzers were calibrated in absolute gain with white noise to within ±8% for all measurements. Usually agreement was ±4%.

Pressure autospectra--Pressure spectra are shown beginning with Figure 23. It is important to note that no corrections for transducer size are made in the data except where the legend on the page specifically says that the curve is corrected. The "Corcos correction" referred to in Figures 23 through 29 is that proposed by G. M. Corcos (1963) to estimate the attenuation of measured wall-pressure fluctuations by the finite size of the transducers. The triangles on the curves indicate where the Corcos correction would have added three db to the existing curves.

A comparison of pressure spectra for flows over smooth and rough walls with no pressure gradients is given in Figure 23. The curve labeled 1 was obtained by the author at a flow speed of 100 ft/sec. The curve labeled 2 was obtained by averaging the data of Blake (1970) over the several flow speeds for which smooth-wall data were reported. Schloemer's data for no-gradient flows are shown in curves 3 and 4. The Corcos-corrected curve is Schloemer's own. With the Corcos correction applied, the Schloemer data are still below the author's and Blake's data.

Part of the explanation is that the Corcos correction is probably not large enough. The rough-wall data which are shown in curve 5 were obtained at 120 ft/sec. Curve 6, attributed to Blake, was obtained by averaging the data of Blake over the several flow speeds at which data were measured. Figure 23 shows that the rough-wall spectrum is approximately equal to the smooth-wall spectrum near $\omega\delta^*/U=1$, but is slightly lower at other frequencies.

Figure 24 shows the same data as does Figure 23, but with scaling on τ_w for the ordinate. Since curves 1, 2, 5 and 6 were all obtained from the same facility with substantially identical boundary layers, curves 1 and 2 are in the same relative positions as they are in Figure 23, and so are curves 5 and 6. Schloemer's data have moved down, and are appreciably below data of Blake and the author at all frequencies.

Figure 25 shows FS and FR spectra, with ordinate scaling of τ_w. Again, Schloemer's results are much lower than the author's, at all frequencies. The discrepancy in this figure is about the same as the one in Figure 24. It appears that differences between curves 2 and 3 in Figure 25 are due to differences in instrumentation or facilities between Schloemer and the author, rather than an effect of the favorable pressure gradient. With ordinate scaling on τ_w, the rough-wall results (curves 5 and 6) are again below the smooth results (curves 1 and 2) except at the very highest frequencies; curve 1 is probably depressed slightly above $\omega\delta^*/U_\infty \approx 1$ from viscous dissipation, because the smooth-wall boundary layers were so thin. The ordinate scaling on τ_w forms a good collapse between flows of the same wall type

and the two different gradients. Curves 1 and 2 in Figure 25 have been averaged to form the solid line in Figure 26. The dashed line in Figure 26 is the same as curve 1 in Figure 24. The agreement is very good, and the effect of viscous dissipation at the higher frequencies in the FS flow is evident. The collapse between the FR flows and the no-gradient rough-wall flows is slightly better because viscous dissipation does not depress the spectrum of the FR flows. The spectra of both FS and FR flows is severely curtailed by the high-frequency limit of the microphone used. This unfortunately makes the comparison of favorable gradient flows with those with no gradient less satisfying. However, it seems clear from the data presented here that outer abscissa scaling and inner ordinate scaling collapses data for both smooth and rough walls within 2 db or so. It is also clear that a large amount of pressure power has been lost at the higher frequencies in both FS and FR flows. The problem is much more severe than with flow with no gradient, and the FS flow measurements have lost the most high-frequency power. These differences in experimental inadequacy make the comparison of broadband pressure power more difficult, as noted by Schloemer (1966).

The pressure spectra for AS flows are shown in Figure 27 with outer variable scaling for both axes. The adverse gradient flows have wall law regions which extend a small fraction of the boundary-layer thickness away from the wall. Therefore, outer scales make more physical sense. But outer scaling does not collapse curves 1 through 5. These curves all describe the same AS flow at several measurement stations. As was predicted in

section B from the correlations, more and more power is concentrated at a nondimensional frequency of .3 or so, at progressively downstream stations. Each curve corresponds to an entry in Table 2. In Figure 27, q is a function of x. The lower frequency limits indicated in Figure 27 were electronically imposed to remove frequencies at which the pressure signal was contaminated by acoustic noise from the wind tunnel; these same limits were used in measuring the rms values in Table 2. A negligible amount of power could be lost from the high-frequency limits indicated in Figure 27, because the figure shows that very little power was present above a nondimensional frequency of 10. Therefore, the area under the curves in Figure 27 should equal the numbers given in Table 2. Curves 1 and 5 were checked against the table by hand calculation and found to agree within $\pm 12\%$. The numbers in Table 2 are more accurate since they were obtained with an rms meter accurate to $\pm 3\%$, while the frequency analyzer had been calibrated only to within 8% in absolute gain. Between measurement points 1 and 5, the total power in the wall-pressure signal remains about the same, while redistributing itself to lower frequencies. One obvious explanation for this would be that the turbulent intensities and wavenumber spectra remained about the same between the two points, while the progressively retarded mean flow converted the wavenumber spectra into wall-pressure frequency spectra with progressively more power in the lower frequencies. This idea makes sense only if the pressure depends linearly on the turbulent velocities, because only then can one begin to imply the pressure spectra from the velocity in a simple way. This linearity assumption is equivalent to assuming that

the dominant pressure sources in the boundary layer are the mean shear-turbulence interaction terms, rather than the turbulence-turbulence terms. For an explanation of this concept, and partial experimental verification, see Willmarth and Wooldridge (1963) for smooth-wall flows and Burton (1971) for rough-wall flows. This idea turns out to have some merit, and is revived below, where the velocity spectra are discussed.

Schloemer's adverse gradient results are given in Figure 27 for comparison. There is qualitative agreement. The Corcos-corrected curve almost coincides with curve number 3. This is a coincidence. The shape factors of the two flows are significantly different. But it does verify the results in Table 1 which show that, scaled on outer parameters, the rms pressures for adverse gradient flows are about the same for Schloemer and the author.

The two extreme curves from Figure 27 are replotted in Figure 28. Schloemer's data (uncorrected) are shown again, and Bradshaw's are added. Bradshaw's flow was self-similar with a rather strong adverse gradient. Bradshaw's spectrum is similar to Schloemer's, but much higher in level. This difference can be explained in terms of the higher turbulent intensities in Bradshaw's flow, as displayed in Figure 11. Figure 11 also shows that the AS flow of the author has generally higher intensities than those of either Schloemer or Bradshaw. However, sources were closer to the wall, and should be expected to produce higher wall pressures. The fact that total rms wall pressures were about the same for Schloemer and the author is probably a combination of two opposing effects: (1) the author's

thicker boundary layer, and (2) Schloemer's lower turbulent intensities.

When scaled on outer parameters, the wall-pressure spectra of AS flows did not collapse with the no-gradient spectra. Neither did the different spectra (curves 1-5 in Figure 27) collapse among themselves. On the theory that nondimensionalizing frequency on U_∞ does not take into account the flow retardation near the wall in adverse gradient flows, inner frequency scaling was tried in Figure 29. There is qualitative collapse between the AS and no-gradient flows except at the highest nondimensional frequencies, where viscous dissipation causes the no-gradient spectrum to drop sharply. The inner variable scaling cannot be expected to collapse the high-frequency data in this case, because the wall-shearing stress is not a reliable measure of the boundary-layer profile in the AS flow, the way it is in flows with a large logarithmic region. Still, the reduced shearing stress is a crude measure of the more retarded flows, and, in fact, for most frequencies the inner frequency scaling does a better job than the outer frequency scaling of Figure 27 in collapsing curves 1 through 5. Of course, the low-frequency peaking of curves 4 and 5 cannot be collapsed because it represents qualitatively different behavior. Mixed abscissa scaling, $\omega\delta^*/U_\tau$, gives similar results.

Figure 30 shows the spectra for the AR flows with outer variable scaling. As expected, there is very little Reynolds number dependence. Three different measurement points were used. The only significant difference between the curves of the three measurements is that the high-frequency power is somewhat higher

for the upstream (x=6") measurement point. This same difference shows up between curves 4 and 5 in Figure 27, which describes AS flow. These curves are very similar to the AR curves, except that they are about 5 db below the AR curves at all frequencies. This difference is reflected in Table 2, where the rms values are about 70% higher for the AR flows. The higher pressure intensity is due in part to the higher turbulent velocities of the AR flows, as can be seen in Figures 11 and 12. All power below 40 Hz was removed from both the spectra in Figure 30 and in Table 2. This frequency is lower than the 70 Hz cutoff for the AS flow, and so there is more low-frequency information in Figure 30 than there is in Figure 27.

As in sections A and B of this chapter, it is seen that the character of the AS flow changes markedly between measurement points, whereas the AR flow changes only slightly, behaving like the downstream part of the AS flow.

Turbulent velocity spectra--Turbulent velocity spectra for the FS and FR flows are shown in Figures 31 and 32. Hot-wire probes were used, as explained in section B of this chapter, and spectral analysis was performed by the same Brüel and Kjaer type 2107 wave analyzer that was used for the FS and FR pressure spectra. The method of abscissa scaling is based upon the fact that the turbulence convecting past a hot-wire probe may be considered as approximately frozen. In analogy with equation (3), Chapter I, the turbulent velocity can be approximately represented by a traveling wave with frequency ω and wavenumber $\bar{k}$. If $|\Phi|$ is weakly varying in r_1 (nearly frozen turbulence), then the range of wavenumbers belonging to each frequency will be

narrow. The group velocity of such packets has been experimentally shown by Willmarth and Wooldridge (1963) to be approximately equal to the local mean velocity U(y). Since this experimental result is independent of frequency, one may conclude that the group and phase velocities are equal, and that therefore $\omega/\bar{k} \simeq U(y)$. Thus the abscissa in Figures 31 through 37 may be interpreted as $\bar{k}\delta^*$, where now the graphs are viewed as longitudinal wavenumber spectra. Without the assumption of frozen turbulence, the view is still valid, but it must be remembered that the abscissa is an average wavenumber, as defined in connection with equation (2).

The hot-wires have linear response well beyond the 20 kHz limit of the analyzer, but the finite size of the wires can cause attenuation of high wavenumber turbulence. A characteristic length for the probe is s=.03 in., the length of one sensing wire. For the FS flows, s/δ^* is about .5, so that significant loss can be expected for wavenumbers such that $\bar{k}\delta^*$ is above $2\pi/.5 \simeq 10$.* In the FR flows, loss can be expected for $\bar{k}\delta^*$ above about 40. Examination of the data in Figure 31 shows that no measurements were taken at high enough average wavenumber for the probe size to be a significant limitation. The overriding limitation in Figures 31 and 32 is the upper-frequency response limit of the analyzer. The velocity spectra are normalized to unity by dividing by the mean square intensity. The areas under the curves (when doubled, since all spectra are two-sided) are less than 1 because the intensities were measured with a bandwidth of 2 Hz to 40,000 Hz. Even though probe size attenuated

*It is assumed here that $k_1 \simeq k_3$.

the higher frequencies as described above, the intensity measurements contain on the order of 15% more power for the FR flows, due to frequency limitations imposed by the range of the analyzer.

Figure 31 shows longitudinal turbulent velocity spectra for FS and FR flows. Blake's data for flows without gradient is provided for comparison, and agreement is good. Little Reynolds number dependence can be found. There is some tendency, at the highest wavenumbers, for the spectra measured closest to the wall to have slightly lower spectral levels. Slightly lower levels, at wavenumbers on the order of 1, for the FS flow as compared with Blake's smooth-wall data, can be attributed to viscous dissipation in the FS flow. The effect is not present in the rough-wall data. As with Blake, wavenumber scaling collapses the longitudinal spectra very well.

Normal velocity spectra are shown in Figure 32. The rough-wall data behaves very much like the longitudinal rough-wall data. The smooth-wall spectral data are somewhat different. The collapse between the FS data and Blake's data is not as good, and the tendency for the spectral levels to be lower near the wall in the vicinity of $\bar{k}\delta^*=1$ is much more pronounced in both the FS and the no-gradient flow. The presence of the wall is more important for the normal velocities, for they are required to vanish at the wall. As was seen in connection with Figures 9 and 10, the rough wall does not have this effect.

The spectral analysis for the AS and AR flows was performed with the Federal Scientific analyzer, which operated to 50 kHz. The dynamic range of the analyzer, 55 db, limited the useful frequency range. s/δ^* was about .03 for the AS and AR flows,

so that probe-size attenuation is significant for wavenumbers higher than about $\bar{k}\delta^* = 2\pi/.03 \simeq 400$. Using the argument similar to Corcos' (1963) for wall-pressure measurements, one may argue that below $\bar{k}\delta^*=200$ attenuation from finite probe size is less than about 50%, and below $\bar{k}\delta^*=100$, less than about 20%. The hot-wire and anemometers are linear to within $\pm$15% in the frequency range used. The error associated with extracting u and v components from an x-probe is on the order of $\hat{u}(y)/U(y)$, as discussed in section B. Unfortunately, the turbulent intensities are more than 10% of the mean flow speed over much of the AS and AR layers. The errors incurred in the intensity profiles are not severe, but errors in the spectra are difficult to estimate, and may be considerable.

Figure 33 shows longitudinal turbulent intensity spectra for the AS flow. Three longitudinal measurement points are sampled, each approximately the same distance away from the wall. Except for the much higher level of curve 1 at low frequencies, the curves collapse within experimental error. Without more data to confirm or deny the low-frequency rise of curve 1, which appears anomalous, the validity of this data must remain in doubt. Other differences between the curves are minor. Curves 1, 2 and 3 correspond respectively in longitudinal position to curves 1, 3 and 5 in Figure 27. It is immediately apparent that the vast differences between the pressure spectra are not due to differences in the wavenumber spectra of the longitudinal velocities shown here. Of course, it is possible that the normal intensity spectra are much different, and measurements of v and w are not available to directly dispute this possibility; however,

spectra of all three components of velocity are available for AR flow, and spectral shapes are not markedly different at any flow position although the intensities are different, as shown in Figure 12. It is therefore suggested that the wavenumber spectra remain almost constant along streamlines in the AS flow. The differences in pressure spectra are caused by the changes in mean velocity profiles.

Longitudinal spectra at two positions in the AR flow are shown in Figure 34. The collapse is excellent. Figure 35 compares u spectra at one x-position for several values of y. Note the changes in scale. δ^* has been replaced by L, which is equal to δ^* except very near the wall. L has been set equal to δ^* for the curve numbered 1 which corresponds to $y/\delta^*=1.74$, the largest value of y for which data are shown. The purpose of L is to show that turbulent length scales are measurably smaller near the wall. For curves 2, 3 and 4, representing measurements made successively closer to the wall, L has been determined so as to produce the best possible fit with curve 1. Turbulent velocities measured at a position of $y/\delta^*=1.74$ are presumed to have turbulent length scales that are not affected by the wall. Then the fact that L/δ^* is less than unity for curves 3 and 4 indicates that the proximity of the wall reduced turbulent velocity length scales. Collapse is excellent, well within experimental error except at the very highest frequencies. It is clear that the wavenumber spectra shift to higher wavenumbers when y/δ^* is below about 1. This fact comes as no surprise, and the idea that wavenumbers are inversely proportional to distance from the wall has widespread support (see, for example, Morrison and

Kronaure (1969)). Similar graphs for normal and spanwise turbulent velocities are shown in Figures 36 and 37. Collapse is again excellent and within experimental error. With the x-probes required to measure v and w, it was not possible to get close enough to the wall to obtain data for $y/\delta^*=0.11$. Therefore, it is not possible to see that the wavenumbers near the wall are indeed higher for these turbulent velocities. (For the same reason, such an effect could not be measured, if indeed it is present, in the favorable gradient flows for which the displacement thicknesses were much smaller.) But it is clear that all three types of wavenumber spectra are independent of position in the flow except possibly very near the wall. Comparing Figures 35, 36 and 37, the three types of spectra have exactly the same shapes. The w spectra are shifted up about 30% in wavenumber relative to the u spectra, and the v spectra are shifted up another 35% in wavenumber relative to the w spectra. Although these differences are slight, there is enough data to be sure of them.

The longitudinal velocity wavenumber spectra are uniform throughout all flows measured. The normal spectra are uniform throughout the adverse gradient flows, but not the FS flows. The anisotropy of the favorable gradient turbulence is due to the presence of the smooth wall. In light of the low wall stress in the adverse gradient flows, and the low influence of the wall in terms of the mean profiles, it is expected that adverse gradient anisotropy would be less.

Assuming, again, that the mean-shear turbulence interaction pressure sources are responsible for most of the fluctuating

wall pressure, then the wall pressure depends linearly on the turbulent velocities. Equation (7) from Burton (1971) is reproduced here:

$$4\pi p(o,t) = \int_V \frac{dU}{dy_2} \frac{\partial v}{\partial y_1} \frac{dV(\vec{y})}{|\vec{y}|} \tag{5}$$

where the volume V is the entire boundary layer, and pressure is measured at the origin. This equation expresses the pressure as a spatial integral of mean shear-turbulence sources, after Lilley and Hodgson (1960). It allows qualitative explanation of the observed pressure spectra. In the FS and no-gradient smooth-wall flows, with shape factors below H=1.4, mean velocities are close to U_∞ except in the viscous sublayer where the turbulent intensities are low. If the turbulent intensity is contained in higher wavenumbers nearer the wall, and lower wavenumbers farther away from the wall, then the convection of these waves at local mean speed will create fluctuating wall pressures over a wide range of frequencies. The rough wall retards flow near the wall, and increases shape factors to about H=1.6. With the convection speeds lower for the wave packets of highest wavenumber, the amount of fluctuating pressure energy that is generated at the higher frequencies will be less in rough-wall flows. This conclusion holds for both no-gradient and favorable gradient flows, and is borne out in Figures 23, 24 and 25. The AS flow for ξ greater than about 15 and all the AR flow had an approximately linear profile over much of the boundary layer, that is, $U(y) \approx U_\infty y/\delta$. In this case, a shift to higher wavenumbers of the turbulent velocity at points closer to the wall is countered by a drop in local convection velocity which leaves the frequency spectrum that is generated at a fixed point by the convecting

turbulence unshifted. This idea explains the concentration of power into a narrower range of frequencies that is apparent in curves 4 and 5 of Figure 27, and all the curves of Figure 30. It should be emphasized that the value of the shape factor alone is not sufficient to predict the approximate bandwidth of pressure spectra. Bradshaw (1967) measured a shape factor of 1.54, which is less than the shape factor of any of the AS and AR flows. Nevertheless, Figure 28 shows that the upstream pressure measurement of AS flow showed power spread over a wider range of frequencies than the power spectral density measurements of Bradshaw, also shown in the figure. Also, the AS and AR data suggest that increases of H above 2 for disequilibrium flows in adverse gradients have little effect on the shape of the wall pressure spectrum.

Cross-spectral densities--Cross-spectral densities were computed by passing the two pressure signals through a pair of tracking filter, Spectral Dynamics model 101A, and then correlating the resulting narrowband signals. The filter bandwidth was either 5 Hz or 50 Hz. The correlation was performed one of two ways. With one method, signals were correlated using the Princeton Applied Research model 100 correlator. The form of the resulting correlogram is obtained from a modification of equation (3), Chapter I, where it is assumed that the filters used are unity gain over a bandwidth $\Delta\omega$ centered at ω_o, and zero gain outside that band:

$$(\Delta\omega)^{-1} R_{\omega_o,\Delta\omega}(x,r,\tau) = \int_{\omega_o-\frac{1}{2}\Delta\omega}^{\omega_o+\frac{1}{2}\Delta\omega} |\Phi(x,r,\omega)| \, e^{i(\bar{k}\cdot r-\omega\tau)} \, d\omega$$

Following Blake (1970), $|\Phi|$ and $\bar{k}$ can be expanded in a Taylor series around $\omega=\omega_o$, and then the integration can be performed. The result to third order in $\Delta\omega$ is

$$(\Delta\omega)^{-1}R_{\omega_o,\Delta\omega}(x,r,\tau) = |\hat{\Phi}|\ e^{i(\bar{k}\cdot r-\omega\tau+\Theta)} + O((\Delta\omega)^4) \qquad (6)$$

where

$$|\hat{\Phi}| = |\Phi_o|\left(1 - (\Delta\omega)^2 \frac{(\bar{k}_o'\cdot r-\tau)^2}{24}\right)$$

and

$$\Theta = (\Delta\omega)^2 \left(\frac{\bar{k}_o''\cdot r}{24} + \frac{(\bar{k}_o'\cdot r-\tau)}{12}\frac{|\Phi_o|'}{\Phi_o} + \frac{1}{24}\frac{|\Phi_o|''}{|\Phi_o|}\right)$$

Primes denote differentiation by ω, and the zero subscript means evaluation at $\omega=\omega_o$. The angle Θ is of the order $(\Delta\omega)^2$. Estimation even of its sign requires considerable knowledge of the function Φ. The form of $|\hat{\Phi}|$ shows the well-known conclusion that the wave envelope of narrowband correlations has its maximum where $\tau=\bar{k}_o'\cdot r$, where $(\bar{k}_o')^{-1}$ can be thought of as the group velocity U_g at frequency ω_o. This velocity need not be equal to the phase velocity $U_c=\omega/\bar{k}_o$. Neglecting Θ, equation (60 shows that the real part of R is a maximum when $\tau_n=(\bar{k}_o'\cdot r+2\pi n)/\omega_o$, where n is an integer, and $|\bar{k}_o'\cdot r-\tau_n|$ is as small as possible. At worst, this latter quantity is π/ω_o, so that this maximum correlation value, at worst, is less than $|\Phi|$ by the factor $(1-(\Delta\omega)^2/(24\omega_o^2))$. Even when third octave filters are used, this factor is very nearly unity, so that the maximum correlation level gives an excellent estimate of $|\Phi(x,r,\omega)|$. The other method of correlation was to compute $R(x,r,0)\equiv$Co, and $R(x,r,\pi/(2\omega_o))\equiv$Quad, using a Spectral Dynamics model 109A Co-Quad analyzer. The the square root of the sum of the squares of those quantities was used as the estimate of $|\Phi|$. Equation

(6) shows this estimate to be approximately equal to $|\hat{\Phi}|$ evaluated at $\tau=0$, and it is less than the true magnitude $|\Phi|$ by the factor $(1-(\Delta\omega\cdot r/(24U_g))^2)$. For small separations, the Co-Quad method is as good as the space-time correlation; but, for large separations, the error can be larger. For the filters used, this error was always quite small.

It is not possible to find the convection time τ_c from a measurement of R at a single frequency and separation. R is real and positive for an infinity of values of τ because the phase is defined modulo 2π. Some experimenters suggest that the convection time is that τ_m for which R is its maximum value, but this method is reliable only if the phase and group velocities are equal. If not, one obtains some combination of the phase and group velocities by forming $U_c=r/\tau_m$. The method used here to find the phase velocity $\omega/\bar{k}$ is to observe that Φ is a smooth function of $\omega\cdot r$. Arg Φ is set equal to zero at $\omega\cdot r=0$, which uniquely defines the phase. Then the convection velocity is just $U_c=\omega_o/\bar{k}_o\approx\omega r/\text{Arg }\Phi=\omega r/\tan^{-1}(\text{Quad/Co})$ to first order in $\Delta\omega$.

U_c is defined to be in the direction of the displacement vector r. When $r_3 \neq 0$, the longitudinal component of U_c is taken as the convection velocity in the data that follow. When $r_1=0$, U_c is not defined.

All narrowband filters were calibrated with white noise, and it was found that the nominally 50 Hz filters had a noise bandwidth of about 43 Hz, while the nominally 5 Hz filters had a noise bandwidth of about 4.1 Hz. The two filters being used were always phase-matched to within 3° (50 Hz filters) or 7° (5 Hz filters) at the common center frequency of the two filters

being used. The two 50 Hz filters were phase-matched within 8° at all frequencies at all times, while the two 5 Hz filters were a maximum of about 15° out of phase. This maximum error occurred at the half-power points of the filter curves, and was due to the slightly different center frequencies of the two filters. To assess the effect of these errors, cross-spectral density measurements were repeated with the filters interchanged with no apparent difference resulting. More significant errors come from statistical inaccuracy. When the PAR correlator was used for correlation, the true averaging time was a fixed 100 seconds. With 50 Hz filters, one statistical standard deviation in the normalized cross-spectral density is then $1/\sqrt{2BT}=.011$. 50 Hz filters were used when $\omega r/U_g$ was large, and allowed normalized correlations as low as .03 to be measured with confidence. This method was used to spot-check the results obtained by the other method. With this other method, the Co and Quad parts of the correlation, defined above, were obtained as a continuous function of frequency for a fixed displacement r. (Thus Arg Φ was obtained as a continuous function of ωr.) This method was faster than the point-by-point method using the correlator at fixed frequencies, and was therefore used to obtain more of the data. With either method, the nominally 5 Hz filters were used for lower frequencies so that $\Delta\omega/\omega_o$ was never more than .2. The Co-Quad averager was modified to obtain true averaging times continuously variable up to 200 seconds. At the maximum averaging time, $1/\sqrt{2BT}$ was .008 with the 50 Hz filters. Each PAR correlogram supplied the amplitude and phase of Φ for a single value of each of its arguments. Each correlogram was statistically independent. When the Co-Quad method was employed,

frequency was swept at a rate not exceeding $\Delta\omega/(3\pi T)$ Hz/sec, where T is the true averaging time, equal to twice the exponential averaging time constant. Thus, data separated in frequency by at least $\Delta\omega$ could be considered statistically independent. Therefore, the scatter in the raw data was a good measure of the statistical errors. The scatter in the data presented in this report is not only from statistical errors, as is explained below.

In addition to statistical errors, the normalized cross-spectral data is biased by errors in normalization of up to 8%. An additional bias error of approximately .012 in the normalized cross-spectral density is due to a drifting bias error in the Co-Quad analyzer.

Cross-spectral magnitudes--Cross-spectral density magnitudes are plotted in Figures 38 through 44. In the notation of these figures, $|\Phi|$ is a function of two components of microphone separation and angular frequency: $|\Phi(r_1,r_2,\omega)|$. In all figures the displacement r is either purely longitudinal or purely lateral. Spot checks of cross-spectral densities with equal displacements in the longitudinal and lateral directions ($r_1=r_2=d$) were made, and the following relation was found to hold within experimental error:

$$\Phi(0,0,\omega)\cdot\Phi(d,d,\omega) = \Phi(d,0,\omega)\cdot\Phi(0,d,\omega)e^{i\Theta} \qquad (7)$$

It should be noted, however, that for some adverse gradient flows, the errors, chiefly excessive scatter, prevent this conclusion from being convincingly shown. This relation includes both phase and magnitude. $\Theta=0$ in all favorable gradient flows. $\Theta\neq0$ for adverse gradient flows with diagonal separations. The phase of

lateral cross-spectral densities was always found to be real, which means that convection velocities are either indefinite or irrelevant. They are taken to be irrelevant. For experimental evidence that equation (7) holds and a discussion of its implication with respect to Corcos' pressure model, see Bakewell (1968).

The cross-spectral densities depend roughly exponentially on their arguments. For this reason, Figures 38 to 44 are plotted with logarithmically-spaced ordinate scales. This has the advantage that the curves are almost straight lines over much of their graphs. Semilog plots of cross-spectral magnitudes are not common; some experimenters complain that they accentuate the relative errors for small values of the ordinate, while compressing the most accurate part of the graph, that part with large values of the ordinate. This complaint, while valid, is not serious, considering the 8% normalization error discussed above. This error makes any detailed consideration of the shapes of the curves for small values of the abscissa very speculative anyway.

Following the usual convention, we define $|\Phi(r_1,0,\omega)|/\Phi(0,0,\omega) \equiv A(r_1,\omega)$ and $\Phi(0,r_3,\omega)/\Phi(0,0,\omega) \equiv B(r_3,\omega)$. In terms of these definitions, equation (7) may be rewritten

$$\frac{\Phi(d,d,\omega)}{\Phi(0,0,\omega)} = A(d,\omega)B(d,\omega)\exp(i\omega d/U_c) \tag{7a}$$

where $U_c(r_1,r_2,\omega)$ is the phase velocity defined by this relation. The two magnitudes in the right-hand member of equation (7a) will be referred to as the A-function and the B-function for brevity. The angle Θ is built into the definition of U_c.

The nondimensionalization of the abscissa in all these illustrations implies a wavenumber scaling. Since U_c is defined in connection with equation (4), Chapter I, as $\omega/\bar{k}$, the abscissa

may be renamed $r \cdot \bar{k}$. Thus, when $\omega r/u_c$ is 2π, then r equals one wavelength at frequency ω. Therefore, good collapse of the data with this abscissa scaling means that all waves have the same spatial decay function when distance is scaled on the wavelength of the waves.

The A-function for FS and FR flows is shown in Figure 38. The scatter in the data is partly due to statistical errors. Estimates of the size of such errors were given earlier. The scatter is also partly due to the imperfection of the wavenumber scaling law imposed on the data by combining r and ω into a single argument. The abscissa scaling collapses all the data very well. No significant Reynolds number dependence is found. This is true for all the cross-spectral data.

Figure 39 compares A-functions for several conditions. Curves 3 and 6 were obtained by fairing lines through the middle of the data points of Figure 38. Curve 2 was obtained by fitting a curve to Schloemer's data. Curve 5 is a curve that Schloemer faired through his own data. Curves 1 and 4 were obtained by fairing curves through the middle of Blake's data. The differences between curves 1 and 2, which both apply to smooth-wall no-gradient flow, are barely within experimental error. Curves 3 and 5, which both describe FS flows, are in excellent agreement. The effect of the favorable gradient with the smooth wall is slight, but quite distinct, since the collapse of the data is so good. By comparison, the degrading effect of roughness is overwhelming. The addition of the favorable gradient decreases this degradation, as expected.

Figure 40 shows B-functions for FS and FR flows. Again,

the data collapse very well. In Figure 41, curves 3 and 6 were obtained by fairing lines through the data in Figure 40. Within experimental error it is not clear whether the addition of roughness has any effect on the B-function. Evidently, if there is an effect, it is to slightly increase the rate of decay. Curves 1 and 4 were obtained by fairing lines through Blake's data. Curve 2 was obtained by fairing a line through Schloemer's data, while curve 5 is Schloemer's own. Blake and the author show that roughness has little effect on the B-function, in both no-gradient and favorable gradient situations. Curves for the FS and FR flows are somewhat below Schloemer's favorable gradient flow. Blake's no-gradient curve is lower. Schloemer is in substantial agreement with both Willmarth (1962) and Bakewell (1968). His B-function is only slightly higher than that of Bull (1967). Thus it is probable that Blake's curves are just a bit too low. The imposition of a favorable gradient reduces the decay of the B-function slightly, whether the wall be smooth or rough. Differences among the B-functions are much less than among the corresponding A-functions.

Data for AS flows are shown in Figure 42. The dashed line was obtained by fairing through Schloemer's data. The data scatter for the AS flow is somewhat worse than for favorable gradient flows. The cause is not increased statistical errors in $|\Phi|$, but rather the irregular dependence of U_c on ω and r, which will be shown below. Replacing U_c with U_∞ in the abscissa in Figure 42 reduced scatter significantly, but the data for different separations did not collapse with this scaling. Data points labeled A, B, and E agree within the scatter. The value of ξ

given in the legend for Figure 42 is that corresponding to the midpoint between the two measurement points. Data points A, B, and E all correspond to about the same value of ξ. A and E differ only in the bandwidth of the filter used. Data points C and D also agree within the scatter. Therefore, the combination of ω and r used for the abscissa is appropriate at least within the scatter of the data. The data for the two values of ξ are markedly different. The A-function of the AS flow deteriorates very rapidly at the downstream measurement area.

Figure 43 gives the A-function for AR flows. Only one value of ξ was used in this flow. The boundary layer was so thick in comparison to the area available to measure the statistics that an insufficient range of ξ was available to make presentation of the two sets of data worthwhile. Data for two separations are presented. The differences in the line of circles and the line of x's is difficult to interpret. At lower values of the abscissa, the AR A-function is slightly higher than that for the AS flow (ξ=11), while at larger values of the abscissa the AR A-function is slightly lower. However, the AS A-function for ξ=23 is much lower than either of the others. A similar effect was observed in section B in connection with broadband correlations: the longitudinal correlation dropped most rapidly with distance with the downstream section of the AS flow.

The adverse gradient B-functions are presented in Figure 44. The dashed line was obtained by fairing through the data of Schloemer. No dependence on separation was found. Points A, B and C agree within the scatter. Comparing Figures 41 and 44, it can be seen that the adverse gradients caused some reduction

of the B-functions, but the effect is not very great. Schloemer's B-function is somewhat lower.

Cross-spectral phases--The FS phase velocities used to scale the abscissa of Figure 38 are shown in Figure 45. Little Reynolds number dependence is found. This result is true for all convection velocities measured. There is very little scatter in the favorable gradient data. Above $\omega\delta^*/U_\infty=1$, there is no dependence on separation. This result is in agreement with Blake (1970), but in disagreement with Schloemer's favorable gradient results. At lower frequencies, there is a slight separation dependence, with smaller separations showing slightly lower phase velocities. The peak in velocity for $\omega\delta^*/U_\infty\approx1$ which appears in Blake's no-gradient results is absent in the FS results. The tendency to lower phase velocities at very low frequencies, first reported by Blake, is even more pronounced here since δ^* was smaller in the FS case, which allowed smaller values of the abscissa in Figure 45 to be reached. The low-frequency behavior of the data is much different than that obtained by Schloemer and many other experimenters (see Blake (1970) for a discussion of this discrepancy).

Figure 46 shows phase velocities for the FR flows. The peak around $\omega\delta^*/U_\infty=1$ which Blake's smooth- and rough-wall data show is present here, although the effect in the FR flow is not as pronounced. Of the four flow types, formed by using smooth and rough walls with zero and favorable gradients, only one flow fails to show this peak in the phase velocity. It is the same flow which Figure 2 shows to contain no wake region in the mean velocity profile. This suggests that the faster wake portion of

the boundary layer is responsible for the increase in phase velocities. At the smallest separations, the high-frequency asymptote is slightly lower for rough walls than for smooth walls. This difference is in agreement with Blake. The data aren't available to show how this asymptote varies with separation distance in the FS flow, or in either the smooth- or rough-wall flows of Blake. However, the FR data show that this high-frequency limit is slightly higher at larger separations. Figure 46c shows a limit of $U_c/U_\infty \approx .63$, exactly equal to the limit for FS flows. So it appears that the rough wall, which causes a retarded logarithmic region in the velocity profile, reduces the convection velocity only at small separations.

AS phase velocities are presented in Figure 47. The behavior of the adverse gradient phase velocities is much different from those of the favorable gradient flows. At all separations, the downstream measurements show slower velocities than the upstream measurements do. This is expected because the adverse gradient slowed the mean velocity throughout the whole boundary layer between the two measurement points. There is considerable separation dependence, with smaller separations consistently showing slower velocities, at all frequencies. Measurements of phase velocity with oblique separations were made for FS, FR and AS flows. Only the AS flows showed any dependence of the phase on the lateral component of separation. This difference shows up in Figure 47 as higher phase velocities for oblique separations.* Compare this with the conclusion in section B

*Only the longitudinal component of each velocity is considered. Thus, if, for example, it is stated here that a 45° oblique convection velocity was 1.414 times as high as the corresponding purely longitudinal one, then the total magnitude of the oblique velocity is actually twice that of the longitudinal one.

of this chapter that broadband convection velocity, which is defined in Chapter I, is similar to the group velocity U_g defined in connection with equation (6) above. Of course, comparison is clouded by the fact that the expression in Chapter I is an integration over a much larger band. Intuitively it is clear, however, that the broadband convection velocity, as defined in Chapter I, is the rate at which energy is convected; and this rate is a weighted average of the various groups of a broadband wave packet. This means that a disturbance which is larger, and therefore of mainly lower frequency, should be observed to move faster. In this sense, the two possible explanations for the observance of high oblique velocities in AS and AR flow, put forth in section B, are really the same explanation. Each says that the large lateral component of the separation selects only the packets of largest spatial extent. These, of course, will on the average have their energies distributed over the lowest frequencies. They are observed to move faster than other packets. Physically, this means that they are positioned further away from the wall where the mean flow is faster. They can therefore be expected to convect faster. This convection velocity is a group velocity, so the physical explanation is consistent with Blake's prediction of high group velocities at lower frequencies. That this effect was not observed in FS and FR flows means that most pressure is generated from regions in the flow where the convection velocities are approximately the same.

Figure 48 shows phase velocities for the AR flow. There is considerable dependence on separation. Data for the smaller

separation show a peak near $\omega\delta^*/U_\infty=3$. This is difficult to interpret. The frequency dependence for lower frequencies, although superficially similar to the low-frequency drop in the favorable and no-gradient flows, is probably not from the same physical cause. The favorable gradient data peaked around $\omega\delta^*/U_\infty=1$, not 3.

Phase velocities depend upon frequency differently for AS and AR flows than they do for the other flows. But their most obvious characteristic is the increased data scatter. This reflects the experimental difficulty that was encountered in repeatably measuring the cross-spectral phases in the adverse gradient flows in spite of the long averaging times that were used. It is this problem which generated most of the scatter in the magnitude data of Figures 42, 43 and 44. The scatter is significantly more than what was estimated earlier, using formulas which assume that gaussian random signals were being multiplied and averaged. The explanation for this increased scatter is not known. Perhaps the wall-pressure fluctuations in strong adverse gradients cannot be treated as a gaussian random process. It was observed in section B that several fluctuating velocity sources at several elevations (and mean velocities) contributed to the measured fluctuating wall pressure. Since it is established that the group velocities of the fluctuating velocity packets are equal to the local mean convection velocities, then it is clear that near $\omega\delta^*/U_\infty=1$, where most of the AS and AR fluctuating pressure power is, there are several group velocities contributing to the pressure, at a single frequency. Perhaps this makes experimental measurement of the phase velocity more diffi-

cult in some way.

Adverse gradient velocities are compared in Figure 49. Curves 2, 3 and 4 were obtained by fairing the data from Figures 47 and 48. Curves 5 and 6 are curves that Schloemer drew through his own data. Bradshaw (1967) transformed the measured cross-spectral density to get $\Phi(k,\omega)$, the wavenumber-frequency spectrum. (Only purely longitudinal separations were used.) He then defined a phase velocity by $U_c(,k,\omega)=\omega/k$. Curve 7 was obtained by the author by graphically computing the following weighted average convection velocity:

$$U_c(\omega) = \int U_c(k,\omega)\ \Phi\ (k,\omega)dk/ \int \Phi(k,\omega)dk$$

The data corresponds to Bradshaw's strongest adverse pressure gradient. This technique does not measure any spatial dependence of the convection velocity. Schloemer's adverse gradient data, like his favorable gradient data, show a low-frequency dependence which differs sharply from the data of Blake and the author. It is possible that curves 3, 4 and 7 actually measure the same thing, where Bradshaw's curve is dominated by longer separations at lower frequencies (where it resembles curve 4) and shorter separations at the higher frequencies (where it resembles curve 3). The much lower convection velocities in the AR flow are due to the very retarded profile which results from the combination of the gradient and the rough wall upstream of the gradient. Curves 1 and 2 correspond to the upstream measurement point of the AS flow, and therefore can be expected to behave much differently than curves 3 and 4. Only Schloemer's data shows an increase of velocities below $\omega\delta^*/U_\infty=1$. The data in Figure 49 are in poor agreement, and detailed explanations of the differences

will not be attempted.

The cross-spectral density experimental results can be summarized as follows: Equation (7a) is verified for all flows. (Additionally, $|\Phi|$ depends only upon the similarity group $\omega r/U_c$ for favorable gradient flows.) The B-functions are not significantly affected by roughness, and only moderately affected by pressure gradient. Favorable pressure gradients moderately increase the A-functions. The A-function is moderately decreased in the AR flow, and in the upstream AS flow, and considerably decreased in the downstream AS flow.

In section B of this chapter, the following predictions were made about the spatial dependence of the longitudinal and lateral cross-spectral density magnitudes. These predictions were based upon scaling separation distance on displacement thickness, and they applied to typical frequencies of each flow. Longitudinal magnitudes were expected to increase with the imposition of the favorable gradient, while lateral magnitudes were expected to remain about the same. This conclusion holds for smooth walls. With rough walls, no significant change in either cross-spectral magnitude was expected. The lateral magnitudes were expected to increase with the imposition of adverse gradient, for both smooth and rough walls. The longitudinal magnitude was projected to be slightly larger for AR flows and slightly smaller for AS flows.

The imposition of the favorable pressure gradient does not alter the nondimensionalized frequency content of the pressure autospectrum, when the frequency is scaled on outer variables. Very crudely, then, "typical" frequencies should be about the

same. Phase velocities are slightly increased with the favorable gradient, so that the implied wavevector spectrum is slightly shifted to lower values of $\bar{k}\cdot\delta^*$, and therefore typical wavenumbers are slightly lower. Thus the experimental fact that the A-function decreases more slowly as a function of $\bar{k}\cdot d$ with the imposition of the favorable gradient implies that longitudinal magnitude also decreases more slowly as a function of r_1/δ^*. This qualitatively agrees with the prediction made in section B for the smooth wall, but not for the rough wall. By the same reasoning, one concludes that the lateral cross-spectral magnitude should decrease more slowly with r_3/δ^* with the application of favorable gradients. This was not predicted in section B from the broadband data. The adverse gradient situation is quite different. In all cases the phase velocities were lowered. In the upstream case, Figure 28 shows that the pressure frequency spectrum is only slightly altered from the no-gradient case. Since $A(\bar{k}\cdot r_1)$ decreases somewhat more rapidly in this case relative to the no-gradient case, and with the typical wavenumber somewhat higher, $|\Phi|$ can be expected to decrease more rapidly with r_1/δ^* at typical frequencies, as predicted in section B. In the AR case, $A(\bar{k}\cdot r_1)$ and $B(\bar{k}\cdot r_3)$ again decrease somewhat faster than for no-gradient flows. But typical frequencies, and therefore typical wavenumbers, are much lower because $\Phi(\omega)$ is concentrated in a low-frequency peak. Thus $\Phi(r_1,r_2,\omega)$ should decrease more slowly in r_1/δ^* and r_2/δ^* at typical frequencies in AR flow, as compared with no-gradient flow. This effect is verified by the broadband data in section B. By the same logic, $\Phi(r_1,r_2,\omega)$ should also decrease more slowly at typical frequen-

cies in the downstream AS case. This result was predicted for lateral displacements, but not for longitudinal displacements. It could be argued that the very fast decay of $A(\bar{k}\cdot r_1)$ outweighs the shift toward lower wavenumbers in this case. However, $A(\bar{k}\cdot r_1)$ in this case does not decrease much more rapidly than $A(\bar{k}\cdot r_1)$ for the no-gradient rough-wall case; and the large difference between A-functions of the no-gradient flows with the two wall types, measured by Blake, are not predicted from the broadband data.

It is clear from this discussion that casual prediction of broadband correlations from cross-spectral densities, or vice versa, is a hit-or-miss proposition. Computation of the broadband results from the narrowband results is possible, but it must be carried out in detail if the result is to be reliable. This task was not done for this report, and the narrowband and broadband results are therefore best viewed as separate and independent.

CHAPTER III

CONCLUSIONS

1. Turbulent boundary layers adjust quickly to the imposition of a favorable pressure gradient, and can be described in the gradient region as homogeneous in the plane of the wall. This conclusion holds for both smooth and rough walls.

2. Turbulent boundary layers do not become self-similar after the imposition of strong adverse gradients, but rather tend toward separation. They may not be considered homogeneous in the longitudinal direction. If the region of examination is confined to those parts of the flow which have noninflectional mean velocity profiles (as was done in this paper), and if separation of the flow is avoided (this was done by terminating the wall to which the layer adhered and allowing a free surface to form), then the layer can be considered homogeneous in the lateral dimension, and the mean flow is two-dimensional. That is, significant three-dimensional effects associated with flow separation are avoided. This conclusion holds for smooth- and rough-wall flows.

3. Wall-pressure spectra can be successfully predicted for favorable gradient flows by scaling amplitude on mean wall-shear stress and frequencies on freestream speed and displacement thickness. This conclusion holds for both smooth and rough walls, except with smooth walls at the highest frequencies where viscous dissipation is important.

4. Adverse gradient wall-pressure spectra are best scaled on outer variables. Prediction of the spectrum shape requires detailed consideration of the mean velocity profile. The profile

shape is a function of pressure gradient and upstream flow conditions. Therefore, adverse pressure gradients which are equal at some longitudinal measurement position, but unequal upstream, will give rise to different mean profiles and different pressure spectra. It is therefore not sufficient to consider only the value of the local pressure gradient, together with such common parameters as the local displacement thickness, freestream velocity, and mean shearing stress at the wall, to predict the pressure spectrum. This conclusion holds for both smooth and rough walls.

5. In the presence of strong adverse pressure gradients, the value of the wall shear stress and the local amount of roughness on the wall are not important in predicting the wall-pressure statistics. This is because the boundary layer is thickened from the adverse gradient, so that the roughness is not normally very large compared to the displacement thickness. This is also because the wall shear stress is small, and the logarithmic portion of the mean profile, which depends upon the value of the wall shear stress, makes up a small portion of the total layer. The effect of upstream roughness on the local wall pressure is to retard the mean flow upstream of the adverse gradient region and therefore affects the pressure statistics. (This conclusion cannot hold if the roughness size is so large that particles project well into the thickened boundary layer.)

6. Broadband spatial coherence of the wall pressure fluctuations is only moderately affected by imposition of the favorable gradient, when lengths are scaled on displacement thickness. Coherence is improved markedly in the adverse gradient flows,

which are dominated by disturbances which are large compared to the displacement thickness, and therefore decay more slowly. Adverse gradient flows are much more oscillatory; that is, they have much stronger negative spatial correlations than the other flow. This is due to a concentration of power into a smaller range of frequencies and wavenumbers.

7. Broadband convection velocities are found to be higher between points with an oblique separation than between points separated only longitudinally, but only in adverse gradient flows. The same result was found for narrowband phase velocities.

8. Lateral cross-spectral densities are only moderately affected by wall roughness or pressure gradient. (Separation is scaled on computed wavenumbers.)

9. Longitudinal cross-spectral densities are considerably lower with adverse gradients and slightly higher with favorable gradients. Favorable gradient magnitudes and no-gradient magnitudes are strongly reduced when a rough wall is substituted for a smooth wall. Adverse gradient magnitudes are not measurably affected by local wall roughness. (Separation is scaled on computed wavenumbers.)

10. Phase velocities are only moderately affected by roughness and favorable gradients. The effect on phase velocities of adverse gradients is strong and complex. Detailed behavior cannot be easily predicted from local mean flow measurements. However, adverse gradients always lower phase velocities considerably.

APPENDIX

THE TURBULENT MOMENTUM INTEGRAL EQUATION

In Chapter II, equation (4) was shown not to hold in turbulent flow. Bidwell (1951) derived the following corrected formula:

$$\frac{\tau_w}{\rho} + \delta^* \frac{dp}{dx} - \frac{d}{dx}(U_\infty^2\Theta) = -\int_0^\delta \frac{\partial}{\partial x}\bar{u}^2 dy - \int_0^\delta\int_0^y \frac{\partial}{\partial x}\left(\frac{\partial\overline{uv}}{\partial x}+\frac{\partial\overline{v}^2}{\partial y'}\right)dy'dy+\delta\int_0^\delta \frac{\partial^2\overline{uv}}{\partial x^2}dy \tag{A1}$$

This equation is valid if the mean flow is two-dimensional. τ_w is evaluated at the wall, and U_∞ and p are evaluated in the flow at an elevation $\delta(x)$. (The exact value of δ is important only to the last term in equation (A1).) δ is large enough that all turbulent quantities can be neglected for $y > \delta(x)$, allowing equation (A1) to be rewritten:

$$\frac{\tau_w}{\rho} + \delta^* \frac{dp}{dx} - \frac{d}{dx}(U_\infty^2\Theta) = -\frac{d}{dx}\int_0^\delta \overline{u^2}+\overline{v^2}dy - \frac{d^2}{dx^2}\int_0^\delta\int_0^y \overline{uv}dy'dy-\delta\int_0^\delta\overline{uv}dy \tag{A2}$$

The longitudinal fluctuating velocities also contribute another kind of error. Impact tubes were used to measure the time-averaged dynamic pressure in the flow:

$$\bar{p}d = \frac{1}{2}\rho\ \overline{(U_a+u)^2} = \frac{1}{2}\rho\ [U_a^2(y) + \overline{u^2}(y)] \tag{A3}$$

where U_a is the actual mean flow speed.* In this report, the measured value of the mean velocity is given by the following

*Viscous errors in this formula have been shown by Hurd et alii (1953) to be less than 0.2% when $Ud/\nu > 250$. Here d is the width of the tube port. This condition was always satisfied, except very near the wall in adverse gradient flow over the roughened wall. No attempt was made to apply the correction suggested by Hurd because their experimental results were for laminar flow only. However, their estimates of errors are reflected in the confidence limits shown in Figures 7 and 8 for the friction factor. This source contributes little to the total error.

expression:

$$U_m(y) = (2\bar{p}_d/\rho)^{1/2} \tag{A4}$$

Comparing equations (A3) and (A4), the measured mean velocity exceeds the actual mean velocity:

$$\frac{U_m - U_a}{U_a} \simeq \frac{1}{2}\frac{\overline{u^2}}{U_a^2} \tag{A5}$$

This formula was derived by Goldstein (1936), among others.

For the purpose of applying equation (A2), the following approximations were made for adverse gradient flows:

$$\begin{aligned} \overline{u^2}(y) &\simeq \varepsilon_1\, U(y)\,(U_\infty - U(y)) \\ \overline{v^2}(y) &\simeq \varepsilon_2\, U(y)\,(U_\infty - U(y)) \end{aligned} \tag{A6}$$

where the ε's are independent of y. These approximations are very good for $\overline{U^2}$, and fair for $\overline{V^2}$ (see Figures 11 and 12).

Combining equations (A5) and (A6), one can get the following estimate of the error in mean velocity measurements:

$$\frac{U_m - U_a}{U_\infty} \simeq \frac{1}{2}\,\varepsilon_1\,\frac{U_\infty - U}{U_\infty} \tag{A7}$$

If a profile shape

$$U(y)/U_\infty = (y/\delta_o)^{1/\alpha} \tag{A8}$$

is assumed, then

$$\delta^* = \frac{\delta_o}{\alpha+1}\ ;\ \Theta = \frac{\alpha\delta_o}{(\alpha+1)(\alpha+2)}\ ;\ H = \frac{\alpha+2}{\alpha} \tag{A9}$$

From measured values of δ^* and Θ, the values of α and δ_o were computed using equation (A9). Combining equations (A7) and (A8) yields the following correction formulas for δ^* and Θ:

$$\delta_m^* - \delta_a^* = \frac{\varepsilon_1\alpha\delta_o}{2(\alpha+1)}\ ;\ \Theta_m - \Theta_a = \frac{\varepsilon_1\delta_o(2-\alpha)}{2(\alpha+1)(\alpha+2)} \tag{A10}$$

where terms in ε_1^2 have been dropped. Corrections (A10) were used

to improve the values of δ^* and Θ appearing in the left-hand member of equation (A2). Examining equation (A6), one sees that the first term in the right-hand member of equation (A2) can be written as

$$-\frac{d}{dx}\left[(\varepsilon_1+\varepsilon_2)\ \Theta\ U_\infty^2\right]$$

Then, neglecting the terms in $\overline{uv}$, equation (A2) may be rewritten in the following form:

$$\frac{\tau_w}{\rho} + \delta^* \frac{dp}{dx} - \frac{d}{dx}\left[U_\infty^2\ \Theta(1-\varepsilon_1-\varepsilon_2)\right] = 0 \qquad \text{(A11)}$$

This form of the momentum equation is used in the body of this report to calculate wall shear stress for adverse gradient flows.

A very crude estimate of the magnitude of the neglected terms in equation (A2) is

$$\frac{\delta(A_2-A_1)}{(x_2-x_1)^2} \qquad \text{(A12)}$$

where A_1 and A_2 are values of $\int_0^\delta \overline{uv}\ dy$ evaluated at two longitudinal positions x_1 and x_2. With the aid of Figure 50, one can write (A12) for the smooth wall flow:

$$\frac{3\text{ in. x}(45.8\text{ in. ft}^2/\text{sec}^2 - 26.3\text{ in. ft}^2/\text{sec}^2)}{(6\text{ in.})^2} \simeq 2.25\ \frac{\text{ft}^2}{\text{sec}^2}$$

Similarly for the rough wall flow:

$$\frac{4\text{ in. x }(189\text{ in. ft}^2/\text{sec}^2 - 98\text{ in. ft}^2/\text{sec}^2)}{(3\text{ in.})^2} \simeq 40\ \frac{\text{ft}^2}{\text{sec}^2}$$

The two rightmost terms in equation (A11) are both of order U_∞^2. Relevant values of U_∞^2 are given in Figure 50. It's clear that the ignored terms are at least three orders of magnitude smaller than the dominant terms in the smooth-wall case. Thus they are truly negligible. In the rough-wall case, the ignored terms are

at least two orders of magnitude smaller, but, given the small magnitude of the first term in equation (A11), the dropped $\overline{uv}$ term is not totally negligible in the rough-wall case. The error estimate in Figure 8 of the friction factor includes an error which was arbitrarily set at 60 ft^2/sec^2, or ± 1.5 times the amount derived above.

REFERENCES

H. P. Bakewell (1968), J. Acoust. Soc. Am., 43:6, p. 1358.

J. M. Bidwell (1951), "Application of the Von Karman Momentum Theorem to Turbulent Boundary Layers," NACA rept. TN 2571.

W. K. Blake (1970), "Turbulent Boundary Layer Wall Pressure Fluctuations on Smooth and Rough Walls," J. Fluid Mech., 44:4, p. 637.

P. Bradshaw (1966), "The Turbulence Structure of Equilibrium Boundary Layers," J. Fluid Mech., 29, p. 625.

P. Bradshaw (1967), "Inactive Motion and Pressure Fluctuation in Turbulent Boundary Layers," J. Fluid Mech., 30, p. 241.

M. K. Bull (1967), J. Fluid Mech., 28, p. 719.

T. E. Burton (1971), "On the Generation of Wall Pressure Fluctuations for Turbulent Boundary Layers over Rough Walls," M.I.T. Acoustics and Vibration Lab. rept. 70208-4.

G. M. Corcos (1963), J. Acoust. Soc. Am., 35, p. 192.

R. Emmerling (1972), Dissertation, Max Planck Institute, Gottingen, West Germany.

S. Goldstein (1936), Proc. Roy. Soc. London, Ser. A, 155, p. 896.

C. E. Hanson (1969), "The Design and Construction of a Low-Noise, Low-Turbulence Wind Tunnel," M.I.T. Acoustics and Vibration Lab. rept. no. 79611-1.

Hurd, Chelsey, and Shapiro (1953), J. Appl. Mech., 20, p. 253.

P. Leehey (1969), "Trends in Boundary Layer Noise Research," in Aerodynamic Noise, H. S. Ribner, ed.

G. M. Lilley and T. H. Hodgson (1960), "On Surface Pressure Fluctuations in Turbulent Boundary Layers," AGARD rept. no. 276.

H. Ludwieg and W. Tillman (1950), "Investigations of the Wall-Shearing Stress in Turbulent Boundary Layers," NACA rept. TM 1285.

W. R. B. Morrison and R. E. Kronaure (1969), "Structural Similarity for Fully Developed Turbulence in Smooth Tubes," J. Fluid Mech., 39:1, p. 117.

H. H. Schloemer (1966), "Effects of Pressure Gradient on Turbulent Boundary-Layer Wall-Pressure Fluctuation," USN Underwater Sound Lab. rept. no. 747.

W. W. Willmarth and C. E. Wooldridge (1962), "Measurements of the Fluctuating Pressure at the Wall Beneath a Thick Turbulent Boundary Layer," J. Fluid Mech., 14, p. 187.

W. W. Willmarth (1963), "Corrigendum: Measurements of the Fluctuating Pressures at the Wall Beneath a Thick Turbulent Boundary Layer," J. Fluid Mech., 21:1, p. 187.

W. W. Willmarth and C. E. Wooldridge (1963), "Measurements of the Correlation Between the Fluctuating Velocities and the Fluctuating Pressures in a Thick Turbulent Boundary Layer," AGARD rept. no. 456.

PREFACE TO THE FIGURES

The following conventions were followed in the preparation of these illustrations. Whenever symbols (circles, triangles, etc.) are placed on a graph, they represent actual data. This method of data presentation is used in Figure 2. Sometimes solid lines are faired through the data, as in Figure 2. In such cases, the symbols, not the line, always represent the data. This method of data presentation is always used when the data were obtained point by point unless the points are so close together in relation to the radius of curvature of the line of data that there can be no doubt whatsoever as to the exact shape of the continuous curve. In this case, the data are often shown as a solid line, as in Figure 4. Curves which represent actual data are always labeled by numerals (1, 2, etc.), never by symbol. Thus the numerals 1, 2 and 3 do not represent data points in Figure 4. This method of data presentation is also used when data were obtained as a continuous function of the abscissa. For example, the wall pressure spectrum in Figure 23 was obtained with a continuously sweeping wave analyzer, and is shown as a solid line. Data of other experimenters which are shown for comparison are always represented by lines. Sometimes these are that experimenter's own lines. When this author has faired a line from the other experimenter's data points, this fact is noted in the text of this report.

The contours of constant correlation in Figures 13 through 16 are the exception to these conventions. They were obtained by interpolating only about 40 data points per figure.

SIDE VIEWS - ALL DIMENSIONS IN INCHES

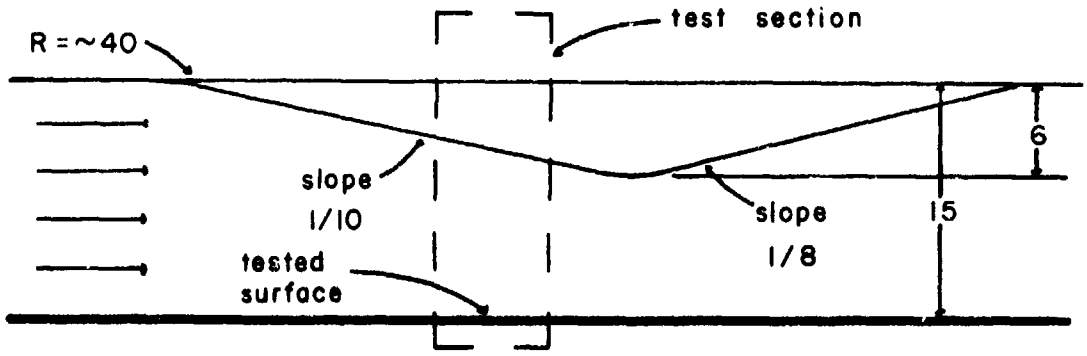

FAVORABLE GRADIENT GEOMETRY CLOSED DUCT

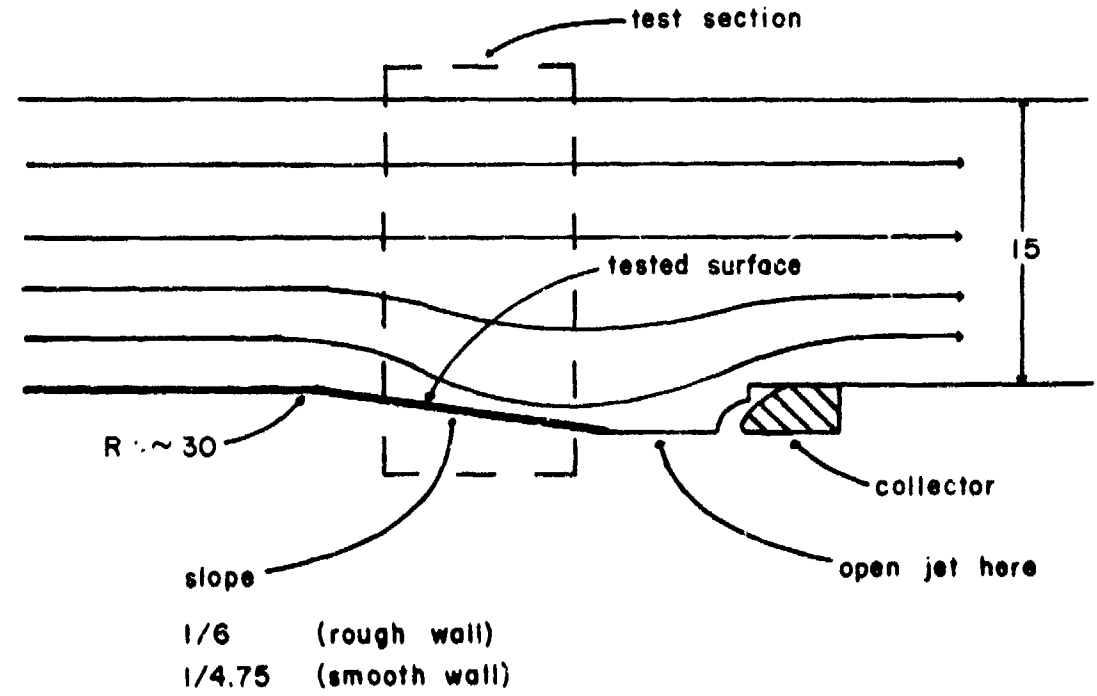

ADVERSE GRADIENT GEOMETRY OPEN DUCT

Figure 1. Wind Tunnel Test Section Schematic Diagram

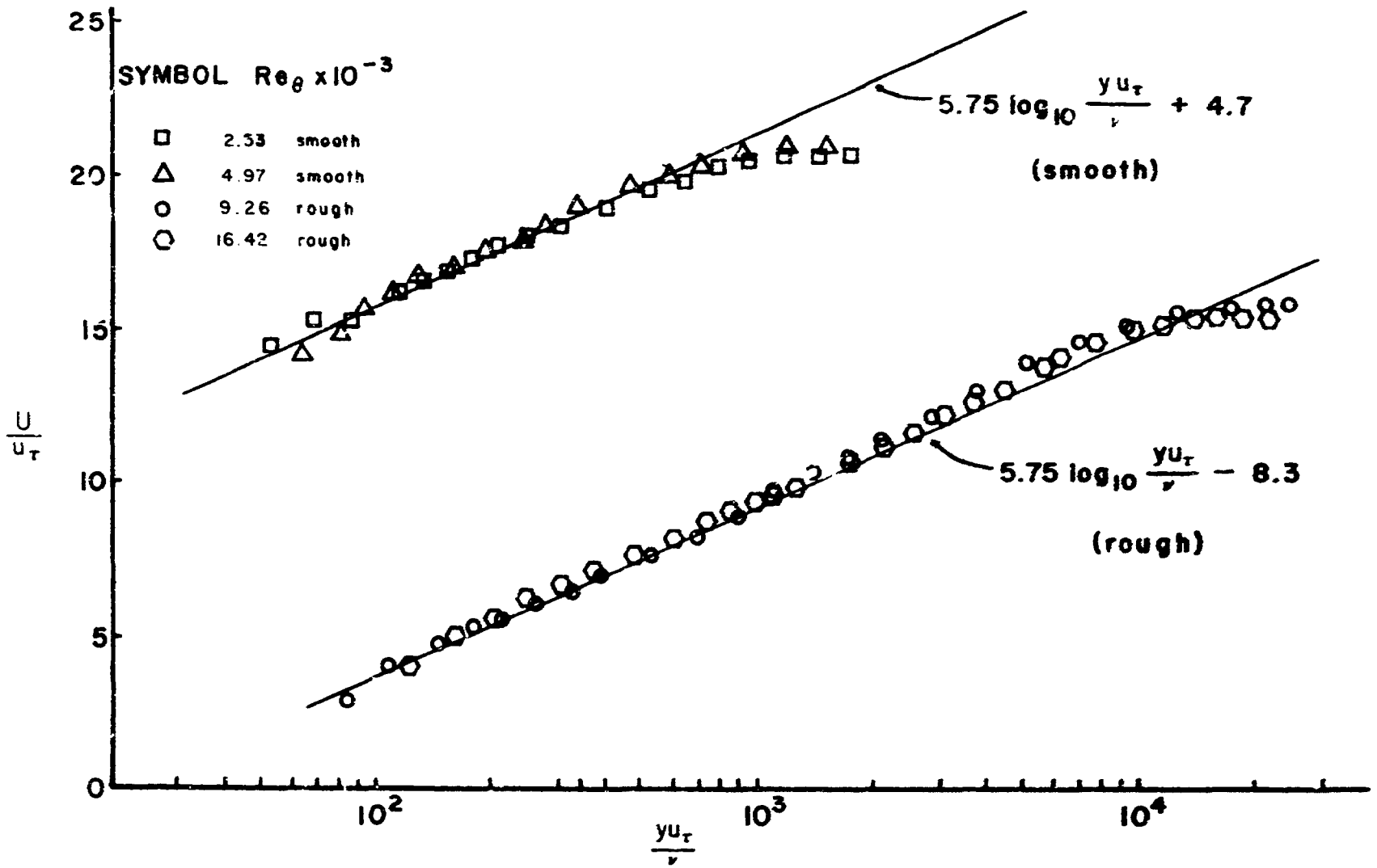

Figure 2. Mean Velocity Profiles with Inner Parameter Scaling. Favorable Gradients.

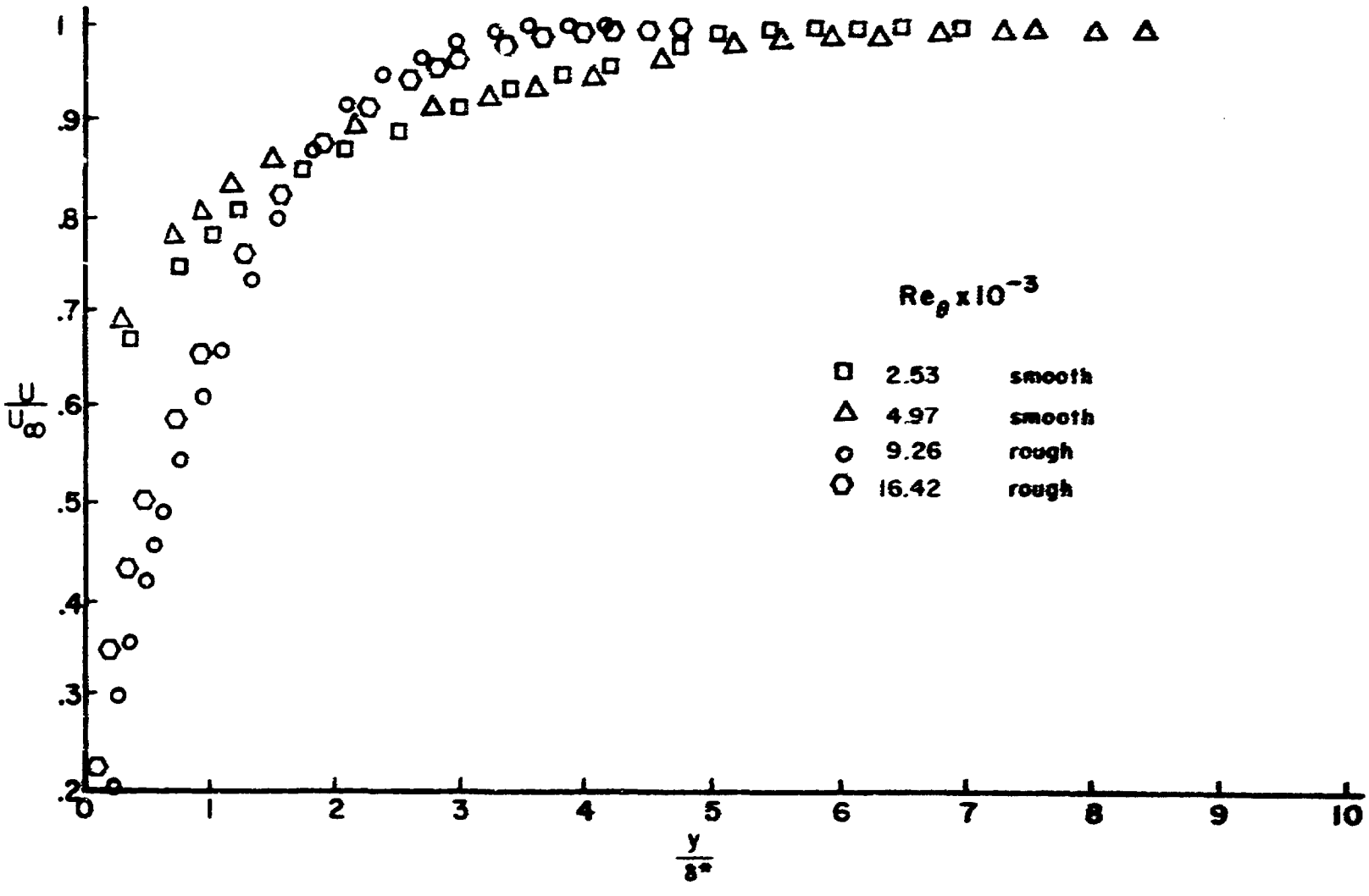

Figure 3. Mean Velocity Profiles with Outer Parameter Scaling. Favorable Gradient.

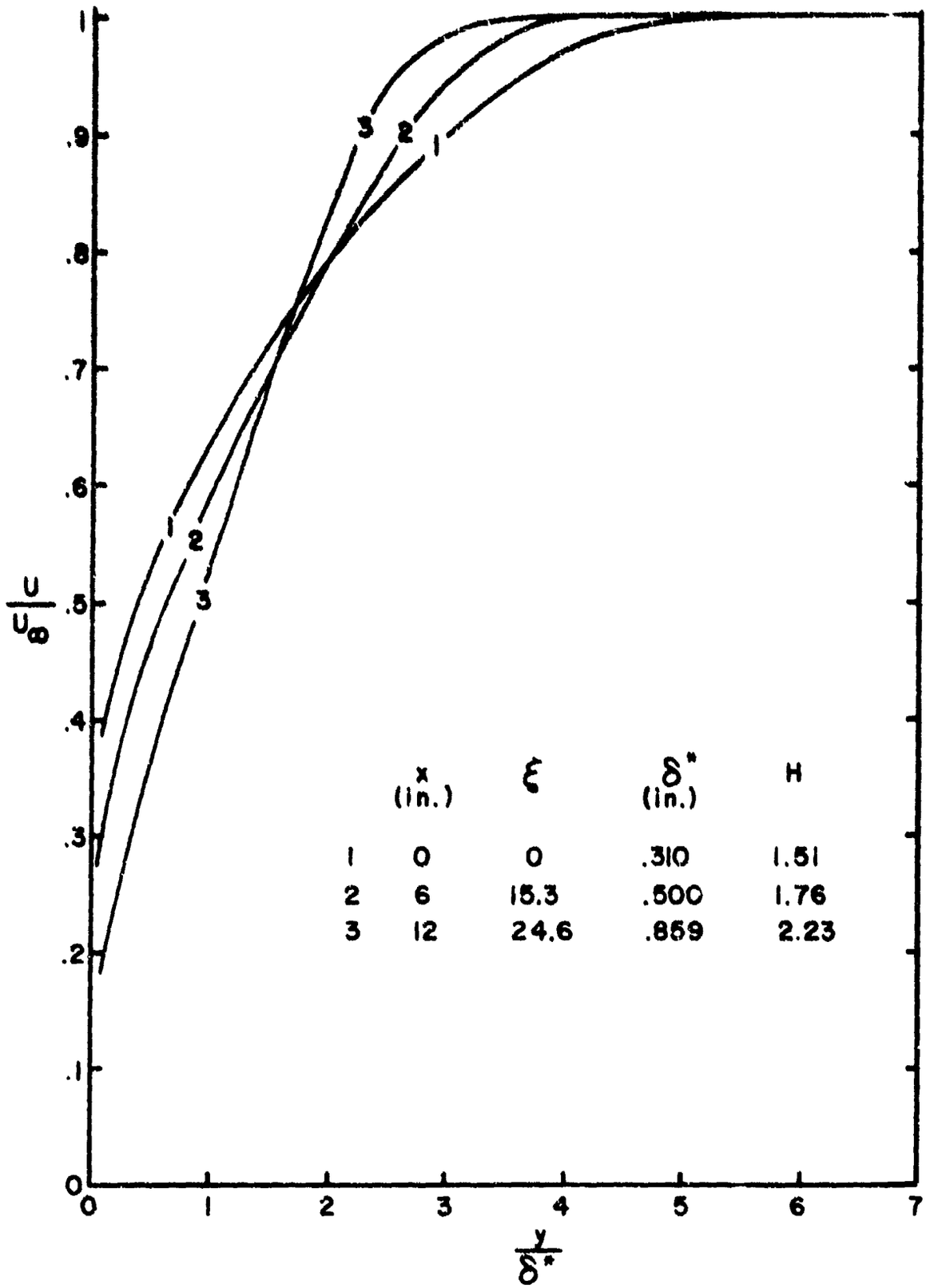

Figure 4. Mean Velocity Profiles with Outer Parameter Scaling. Adverse Gradient and Smooth Wall.

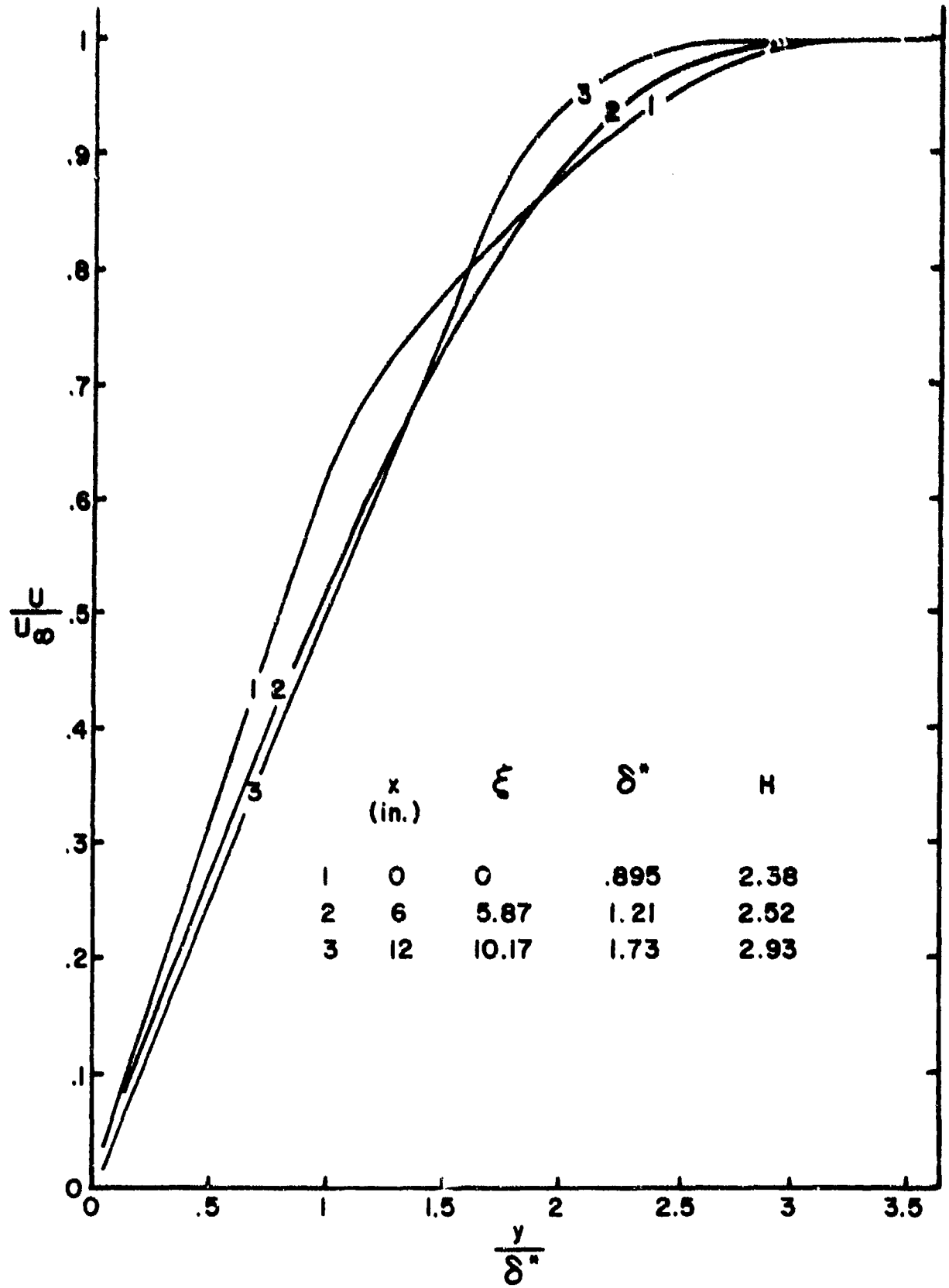

Figure 5. Mean Velocity Profiles with Outer Parameter Scaling. Adverse Gradient and Rough Wall.

TABLE 1

GRADIENT	FAVORABLE						ADVERSE		
Wall Type	Smooth			Rough			Smooth	Rough	
U_∞ (ft/sec)	80	120	164	80	120	160	100	80	160
$\delta^*/\tau_\omega \cdot dp/dx$	-.21	-.18	-.19	-.44	-.43	-.44	13*	36*	37*
$\delta^*/q \cdot dp/dx \times 10^2$	-.10	-.097	-.092	-.35	-.37	-.35	1.3*	1.5*	1.5*
δ^* (in.)	.064	.061	.059	.234	.230	.224	.5*	1.2*	1.2*
Θ (in.)	.051	.049	.045	.140	.142	.138	.28*	.45*	.45*
H	1.30	1.31	1.28	1.53	1.59	1.59	1.8*	2.5*	2.5*
$Re_\Theta \times 10^{-3}$	2.15	3.09	3.88	5.90	8.9	11.6	26*	20*	40*
U_τ (ft/sec)	3.9	6.2	8.0	5.0	7.7	10.0	2.2	1.1*	2.2*
$C_f \times 10^3$	4.8	5.3	4.7	7.8	8.2	7.8	1*	.4*	.4*
$\bar{k}_g$ (in.)	0	0	0	.092	.092	.092	0	.092	.092
d/δ^*	.50	.50	.52	.134	.134	.142	.064*	.026*	.026*
dU_τ/ν	60	102	134	84	130	168	38*	18*	36*
$(\overline{p^2})^{1/2}/\tau_w$	2.15	1.92	2.08	2.26	2.11	2.19	8.0*	31*	32*
$(\overline{p^2})^{1/2}/q_o \times 10^2$	1.03	1.0	.98	1.76	1.74	1.71	(.78-.84)	(1.3-1.5)	

*This number is a function of x; a typical value is shown.

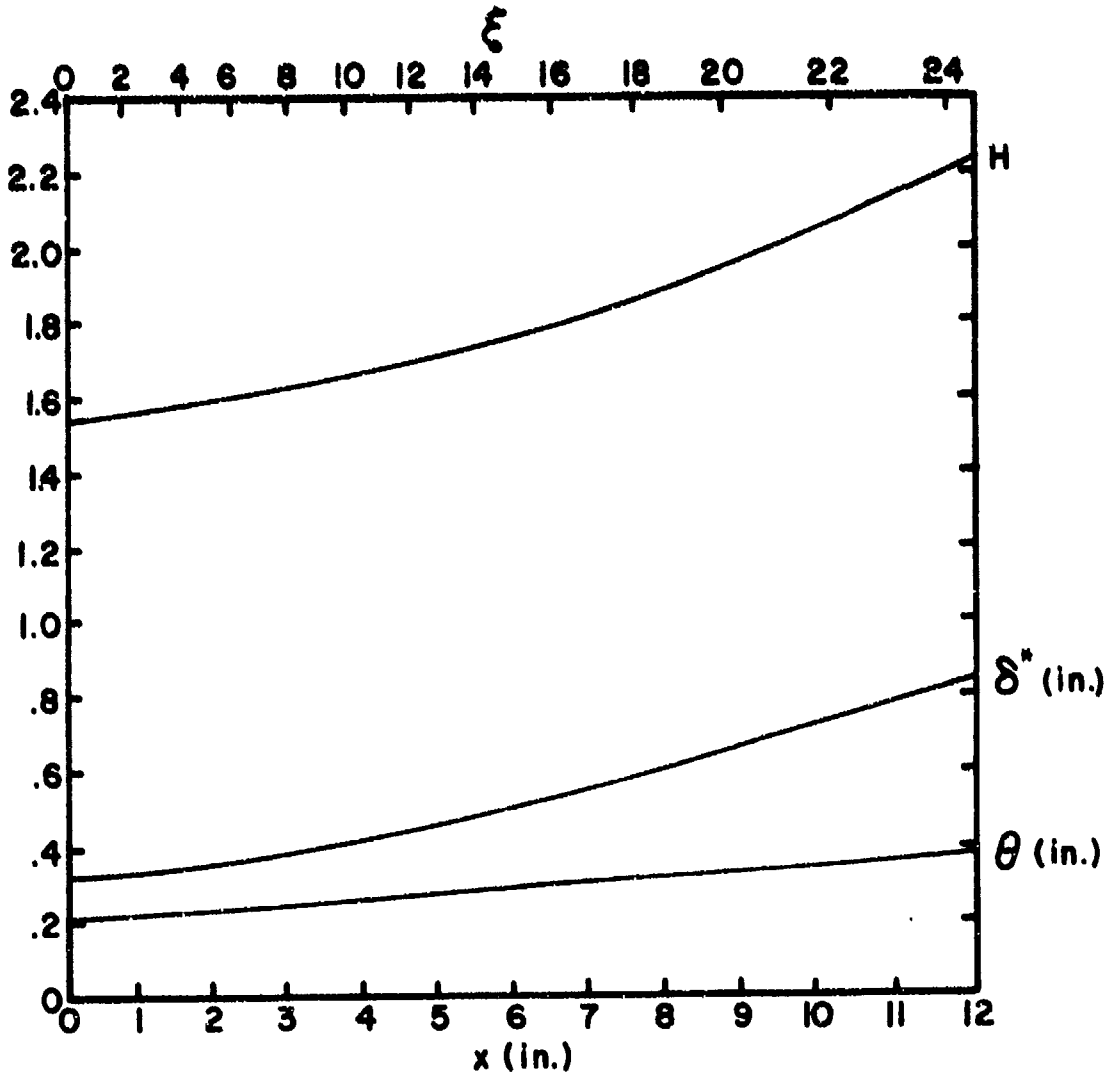

Figure 6. Mean Boundary Layer Properties.
Adverse Gradient and Smooth Wall.

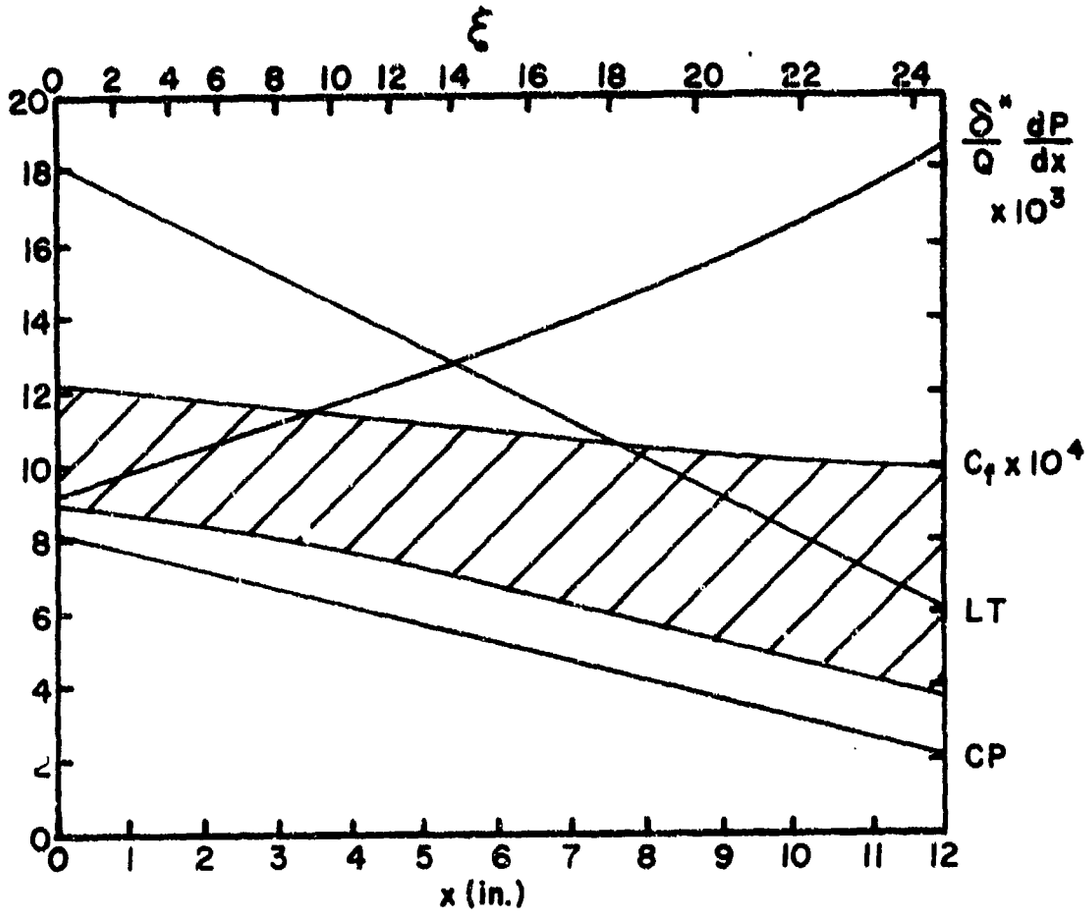

Figure 7. Mean Boundary Layer Properties.
Adverse Gradient and Smooth Wall.

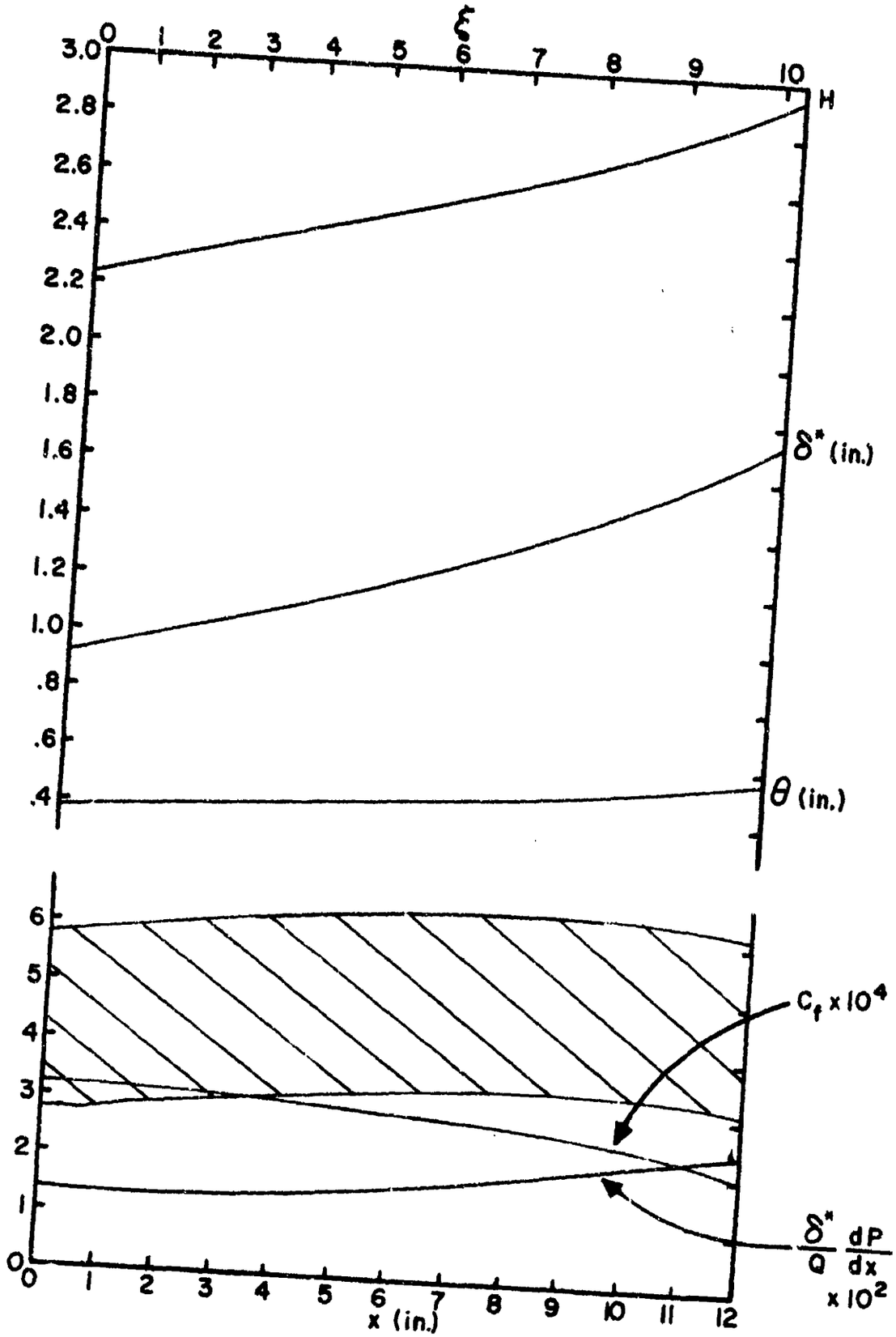

Figure 8. Mean Boundary Layer Properties. Adverse Gradient and Rough Wall.

TABLE 2

ADVERSE GRADIENTS

Total rms Pressures as a Function of ξ

Wall Type	ξ	$(\overline{p^2})^{1/2}/q$	$(\overline{p^2})^{1/2}/q_o$
Smooth	0	.0077	.0077
	10.7	.0088	.0078
	15.3	.0100	.0084
	22.0	.0100	.0077
	24.6	.0101	.0075
Rough	6.07	.013	.013
	8.85	.017	.015
	10.62	.018	.015

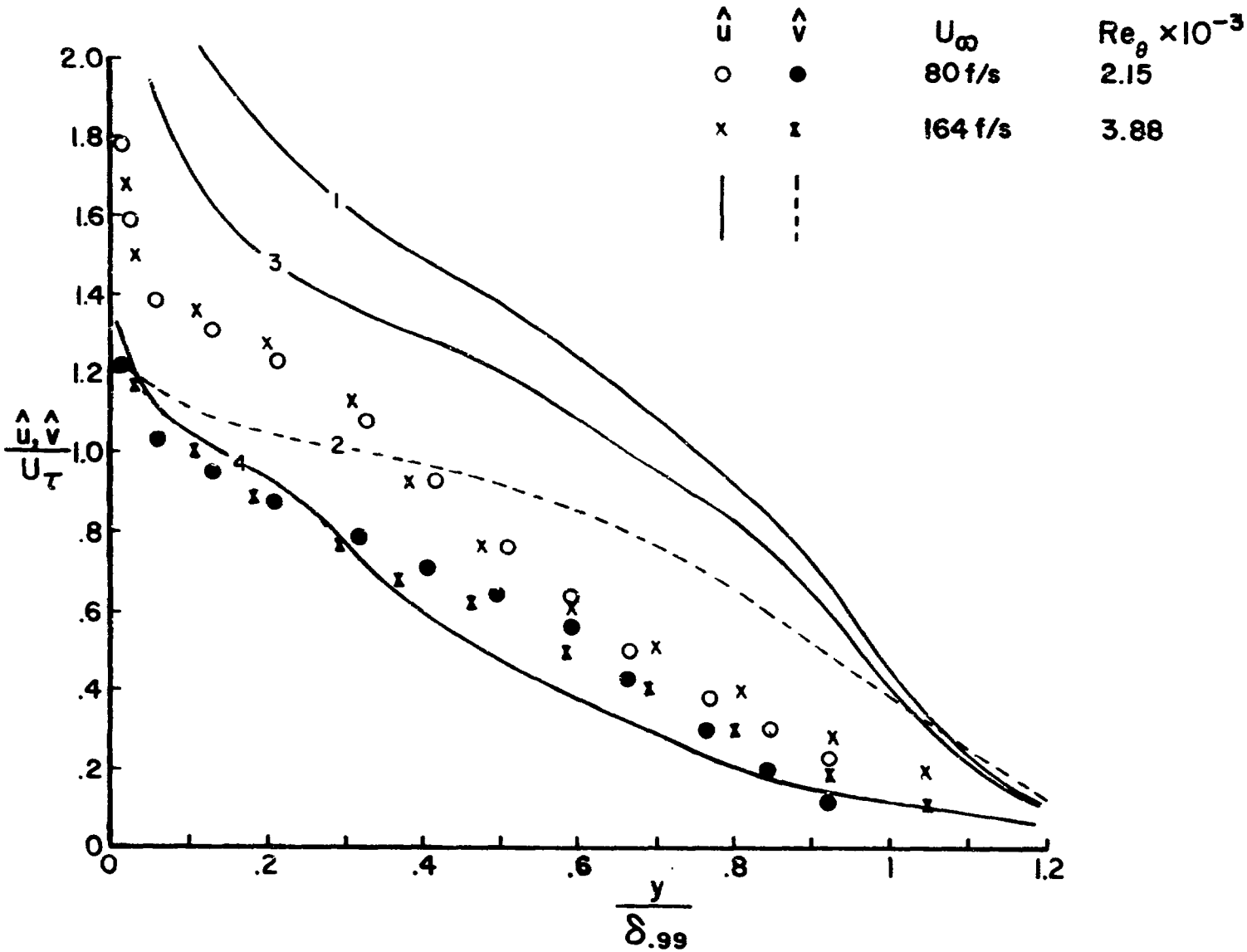

Figure 9. Turbulent Velocity Intensities over Smooth Walls. Symbols: Favorable Gradient:

(1) û no gradient, Blake (1970)

(2) v̂ no gradient, Blake (1970)

(3) û no gradient, Schloemer (1966)

(4) û favorable, Schloemer (1966)

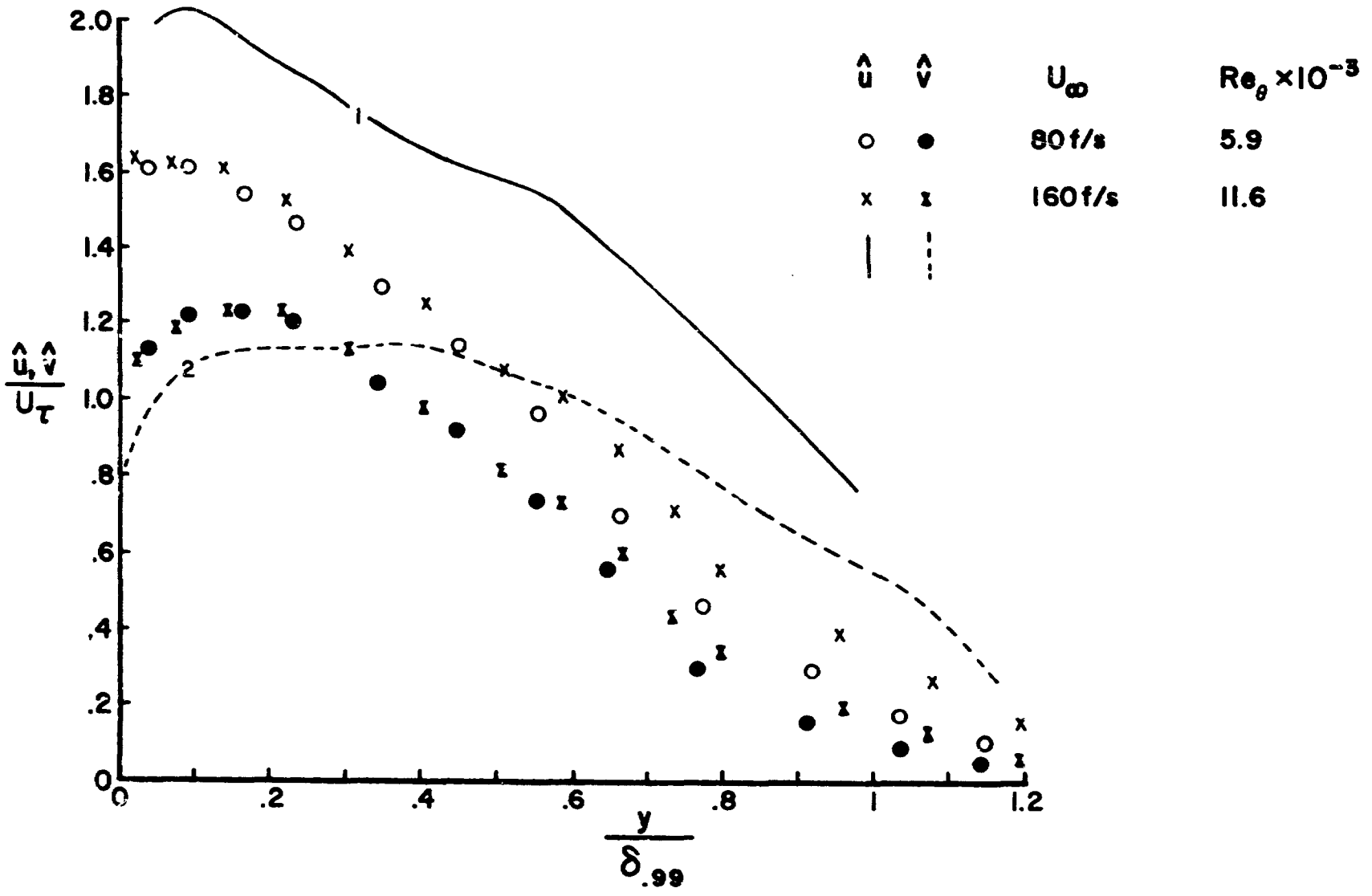

Figure 10. Turbulent Velocity Intensities over Rough Walls. Symbols: Favorable Gradients

(1) $\hat{u}$, no gradient, Blake (1970) (2) $\hat{v}$, no gradient, Blake (1970)

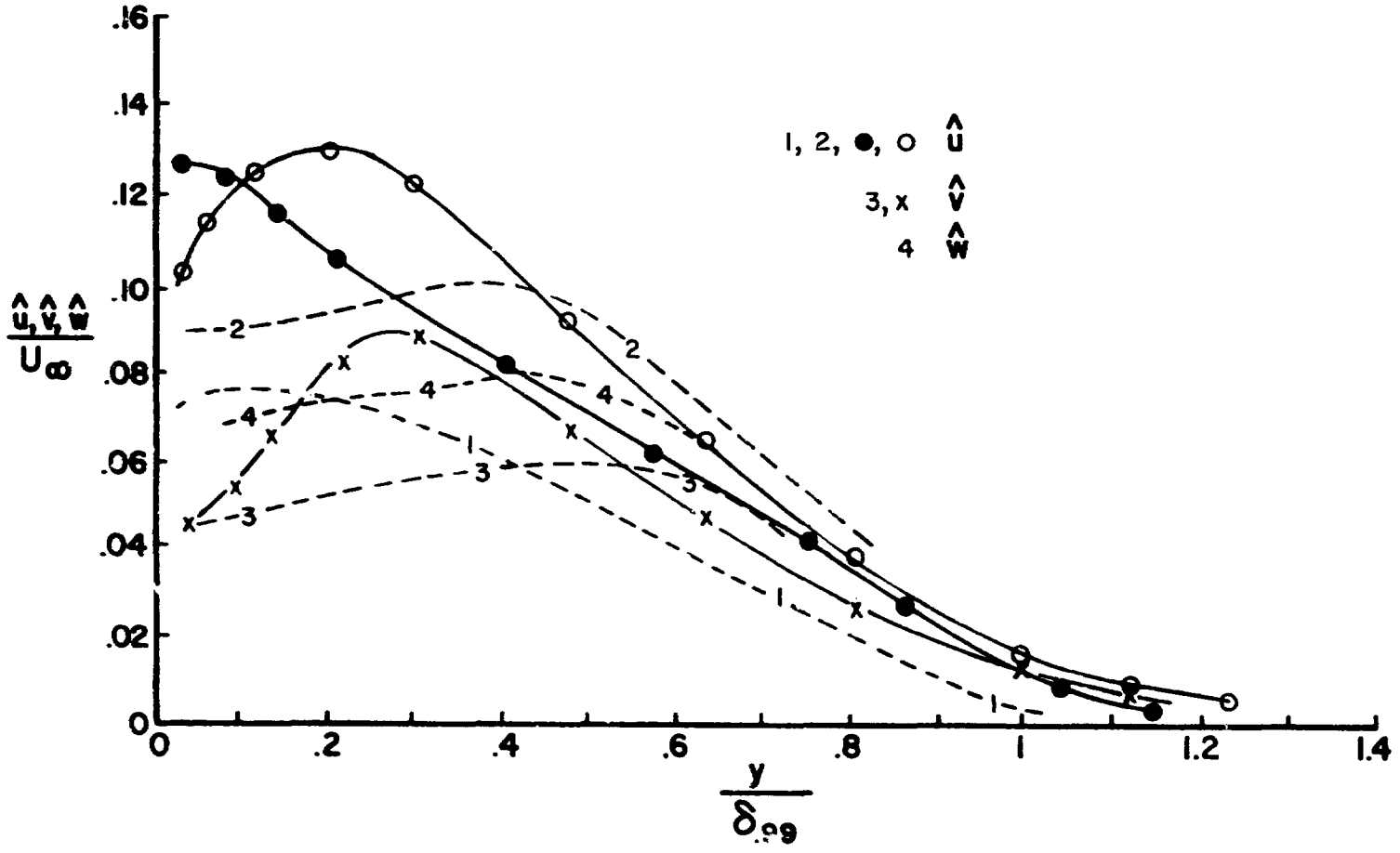

Figure 11. Turbulent Velocity Intensities over Smooth Walls with Adverse Gradients.

(1) $\hat{u}$, Schloemer (1966)
(2) $\hat{u}$, Bradshaw (1966)
(3) $\hat{v}$, Bradshaw (1966)
(4) $\hat{w}$, Bradshaw (1966)

Filled circles: $\xi = 0$. Other points: $\xi = 24.3$

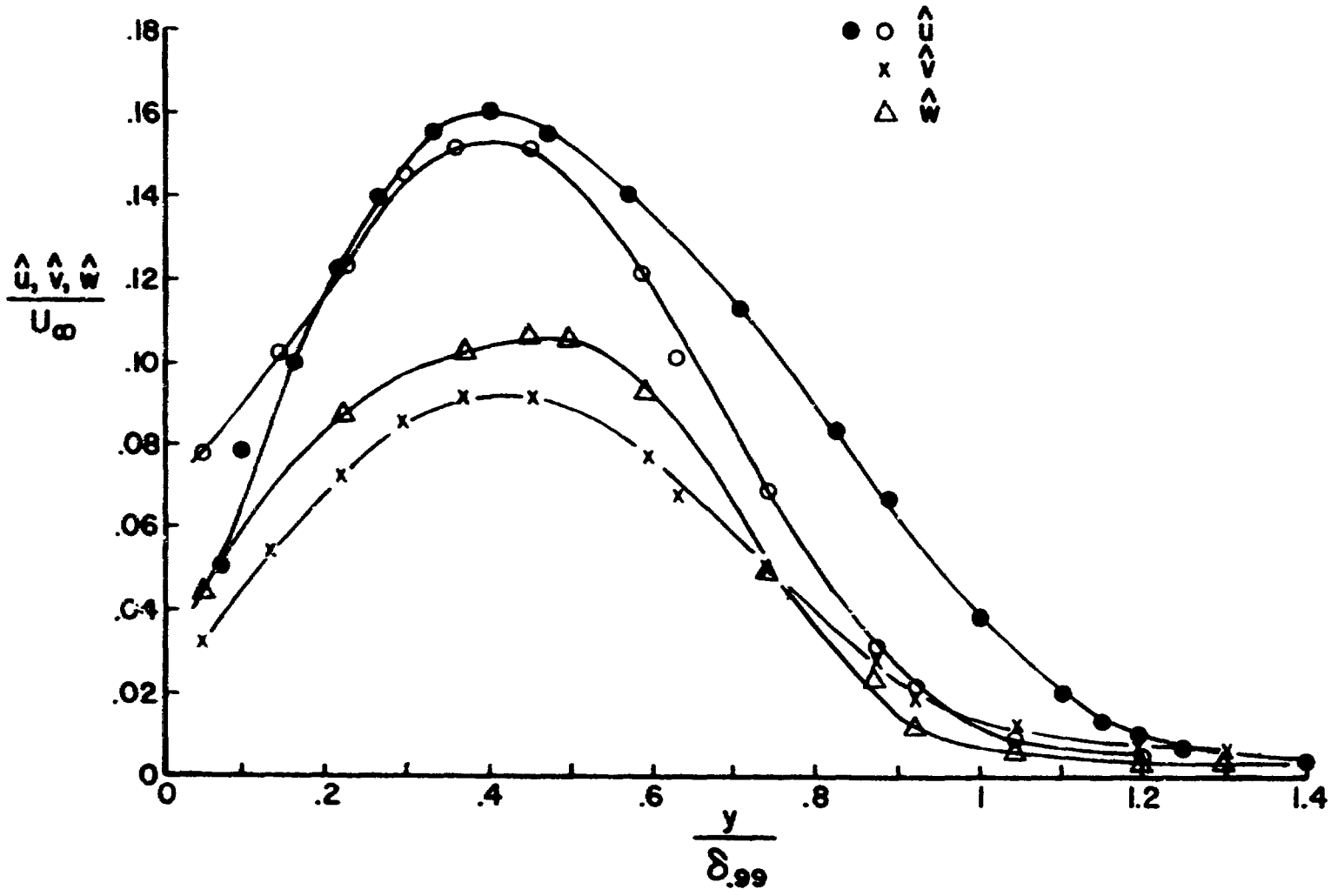

Figure 12. Turbulent Velocity Intensities over Rough Walls with Adverse Gradient

Filled circles: $\xi = 5.6$. Other symbols: $\xi = 10.2$.

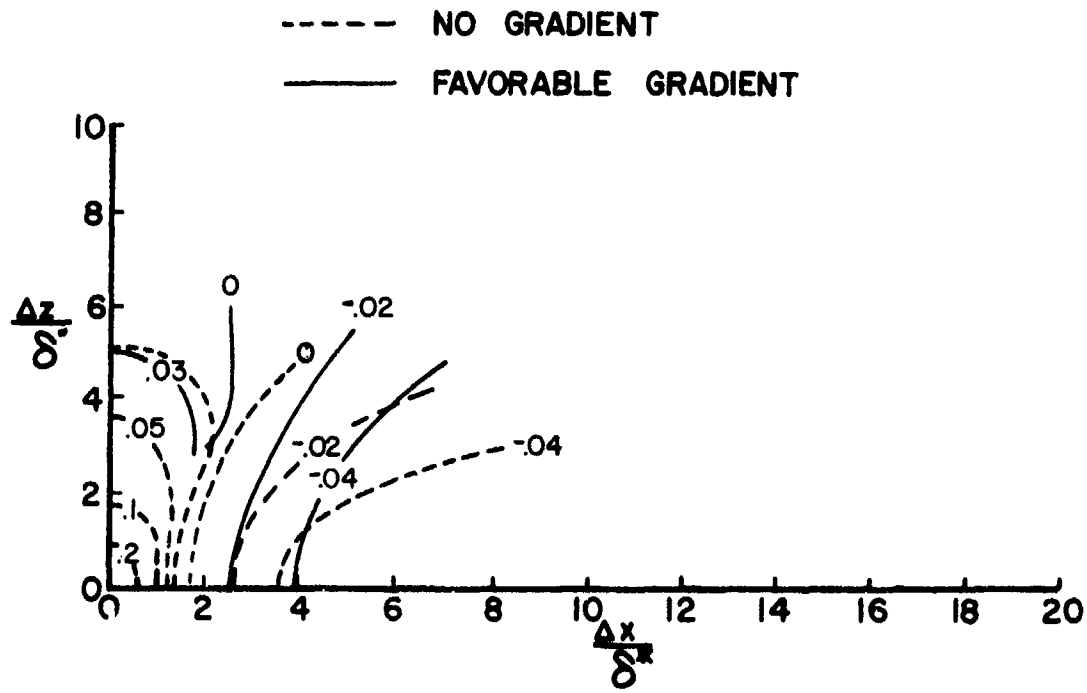

Figure 13a. Contours of Constant Spatial Correlations: $R(\Delta x, \Delta z, 0)$. Smooth walls.

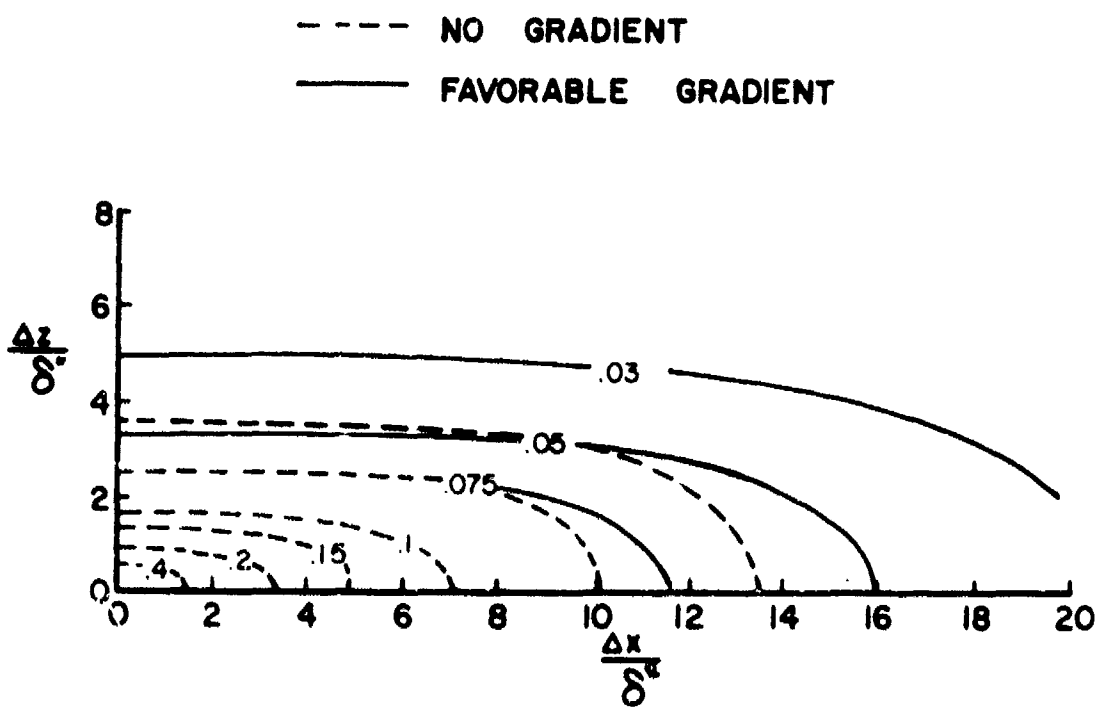

Figure 13b. Contours of Constant Convecting Correlation: $R(\Delta x, \Delta z, \tau m)$. Smooth walls.

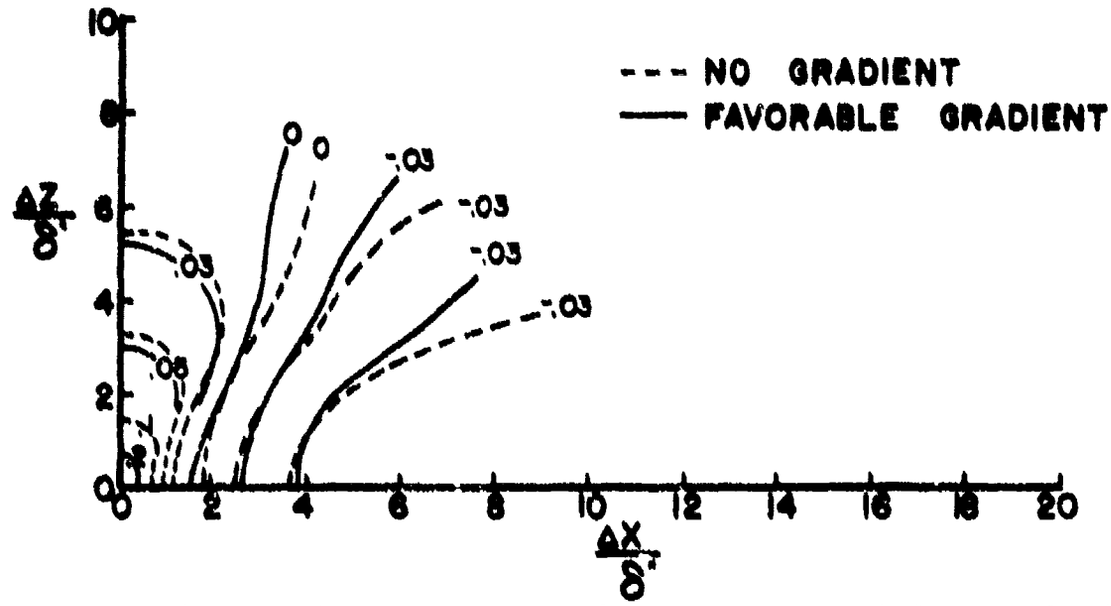

Figure 14a. Contours of Constant Spatial Correlation: $R(\Delta x, \Delta z, 0)$. Rough Walls.

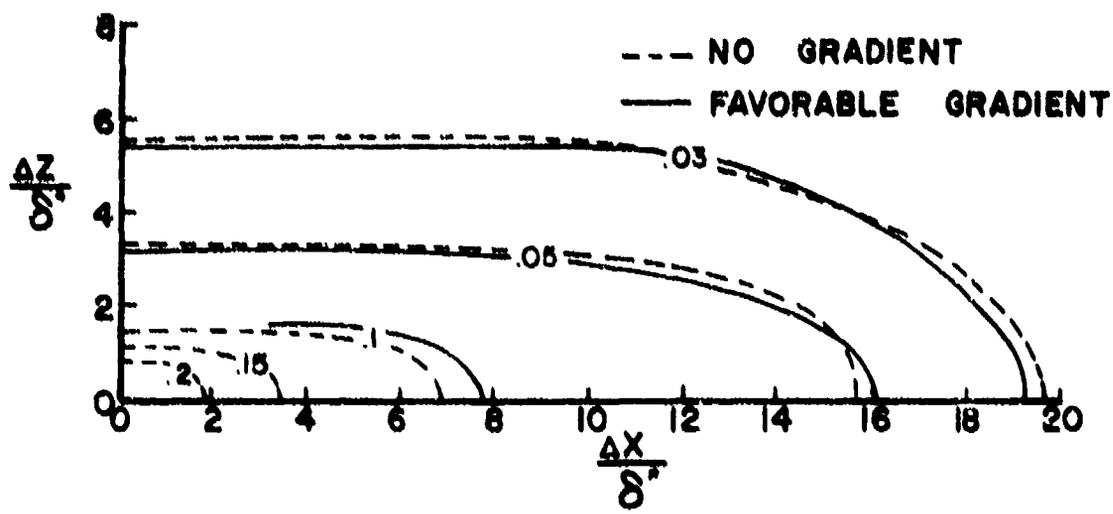

Figure 14b. Contours of Constant Convecting Correlation: $R(\Delta x, \Delta z, \tau m)$. Rough Walls.

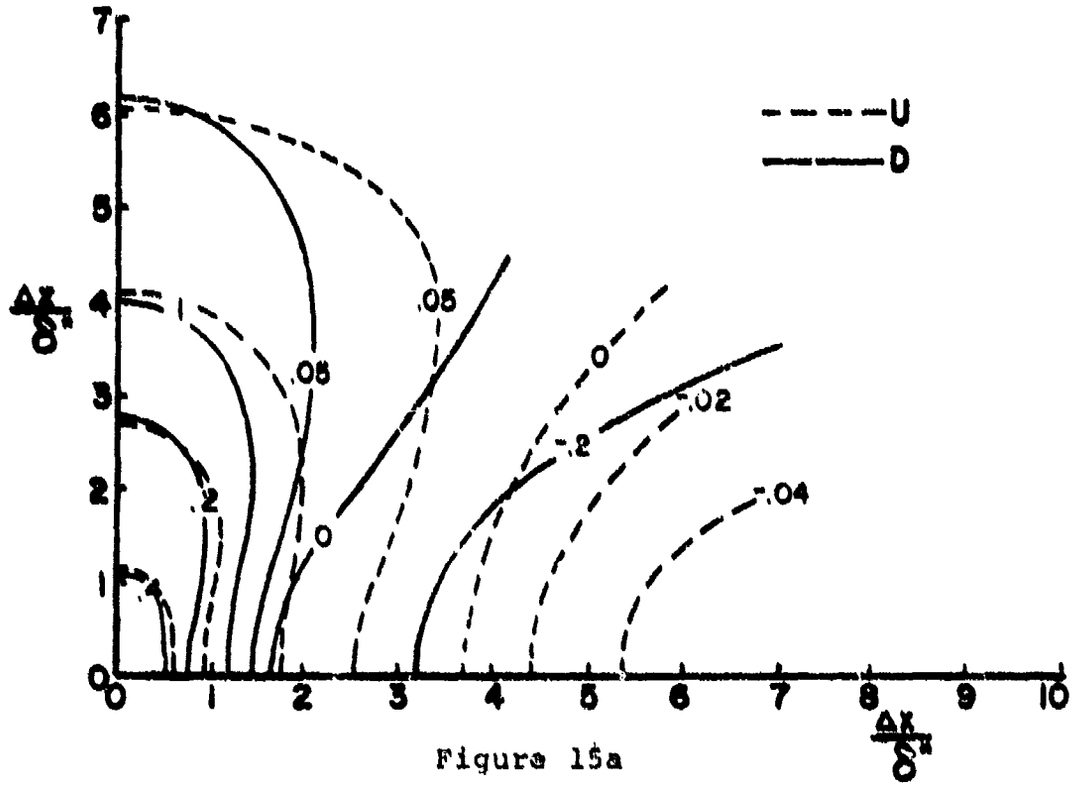

Figure 15a

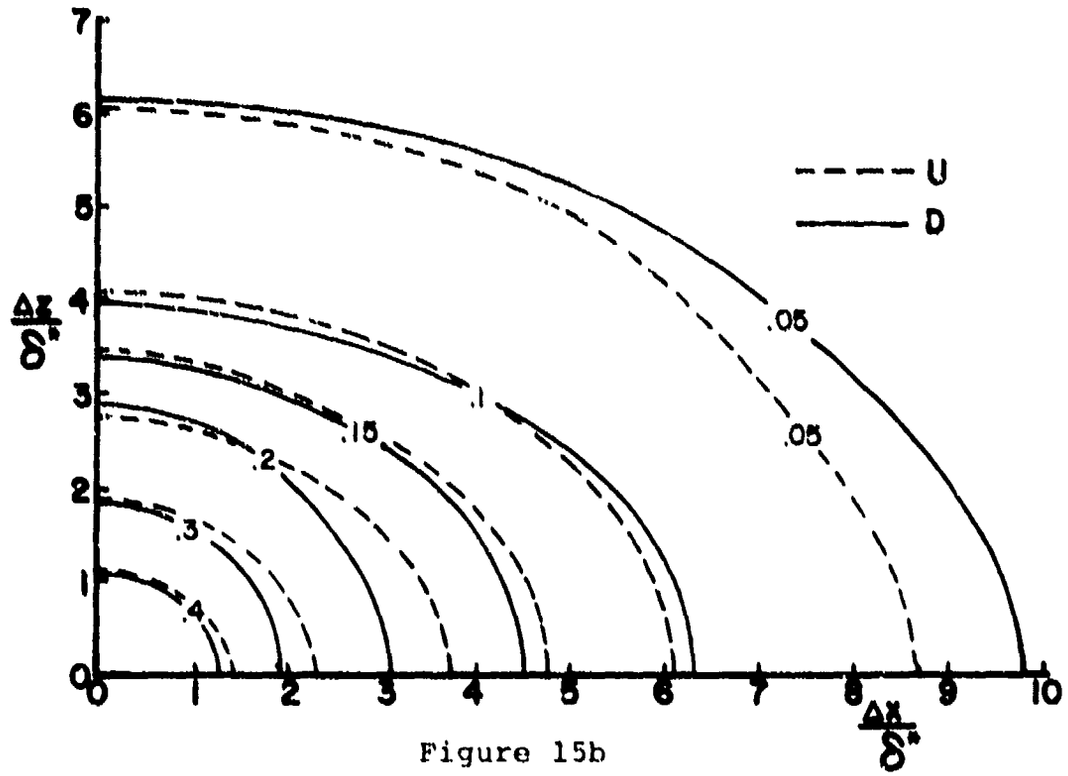

Figure 15b

Figure 15. Contours of Constant Spatial Correlation (15a) and Convecting Correlation (15b). Adverse Gradient and Smooth Wall. U : ξ ~ 8 ; D : ξ ~ 20.

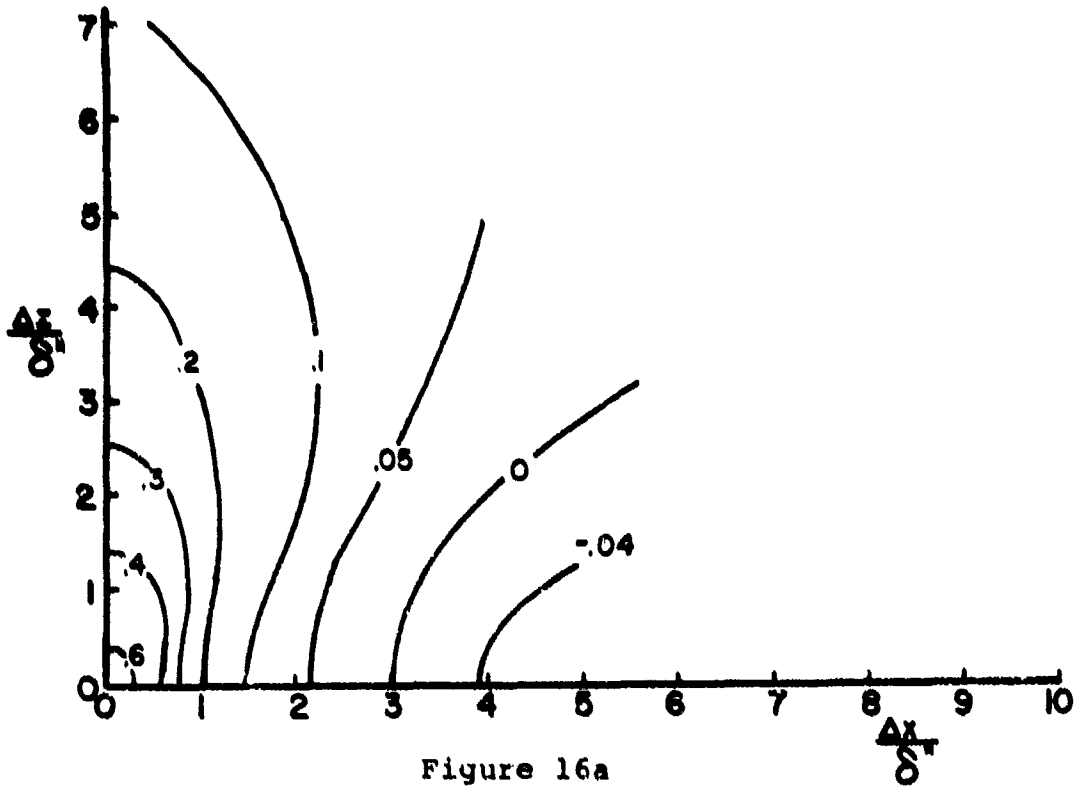

Figure 16a

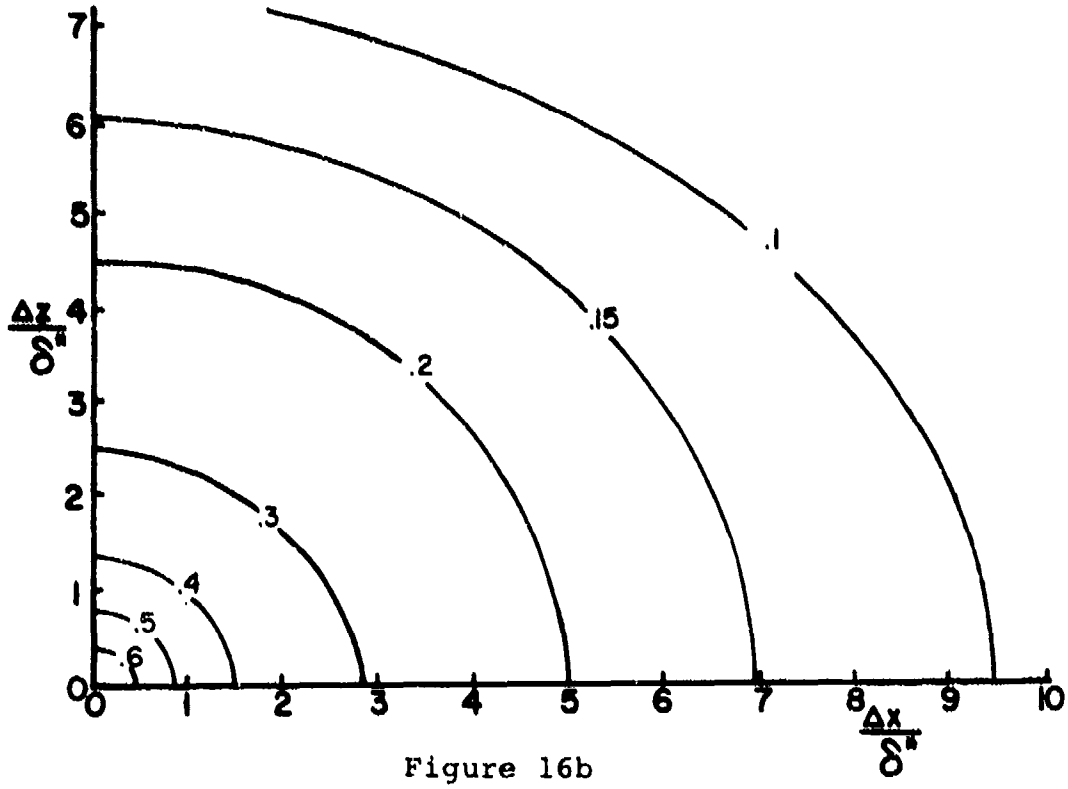

Figure 16b

Figure 16. Contours of Constant Spatial Correlation (16a) and Convecting Correlation (16b). Adverse Gradient and Rough Wall. $\xi \approx 7$.

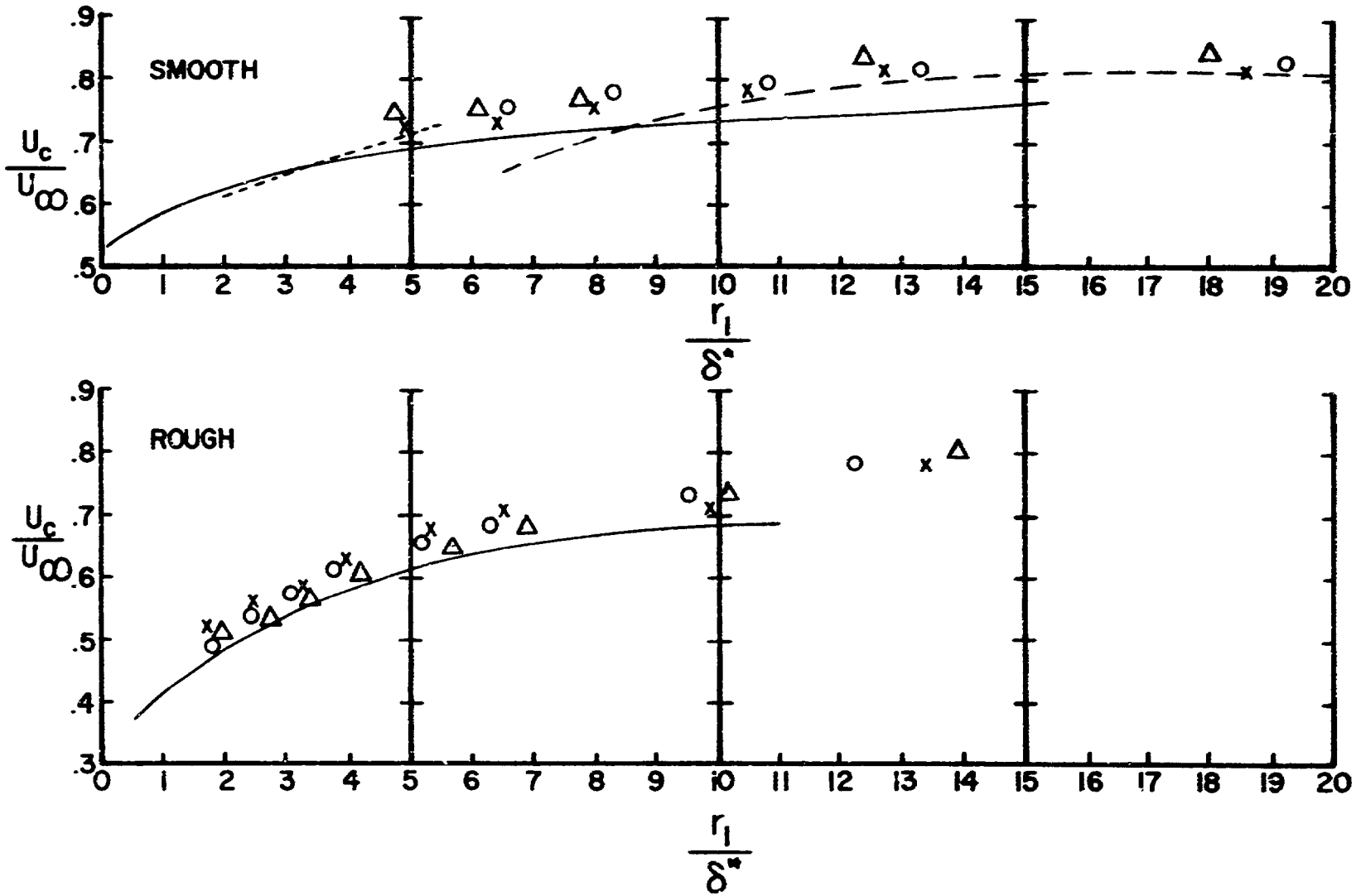

Figure 17. Broadband Convection Velocities. Symbols: Favorable Gradient. U_∞ = 80 ft/sec (O), 120 ft/sec (x), 160-164 ft/sec (Δ).
_____ No Gradient Blake (1970). ------ No Gradient Schloemer (1966).
— — Favorable Gradient Schloemer (1966).

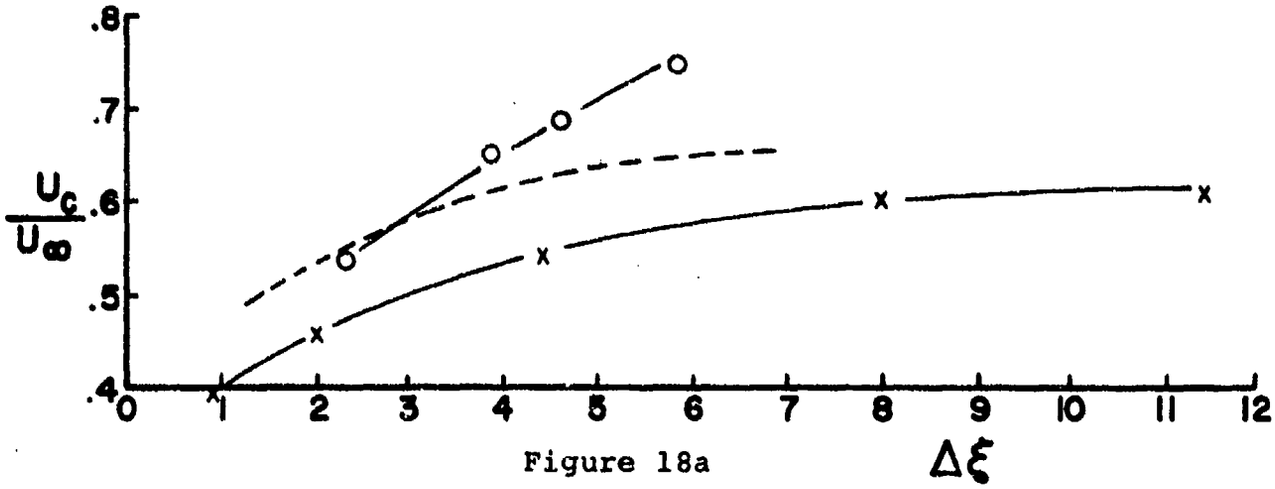

Figure 18a

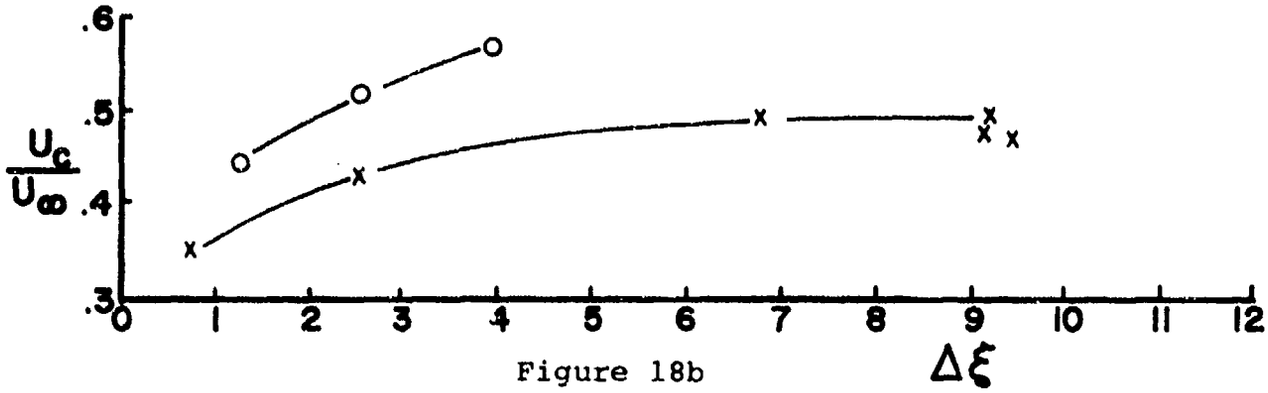

Figure 18b

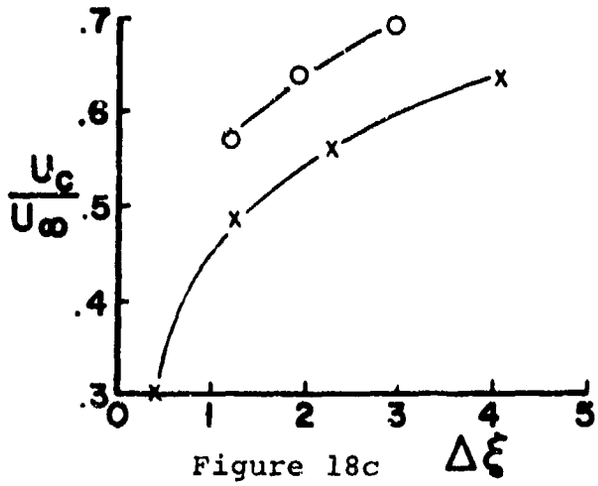

Figure 18c

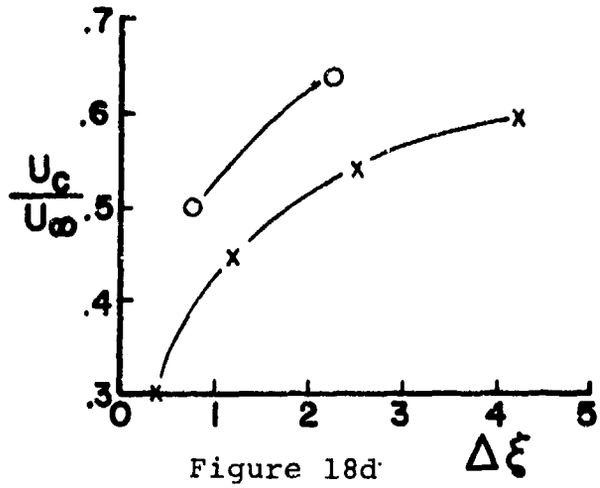

Figure 18d

Figure 18. Broadband Convection Velocities with Adverse Gradients. (18a) Smooth Wall, $\xi \approx 8$; (18b) Smooth Wall, $\xi \approx 20$; (18c) Rough Wall, $\xi \approx 5$; (18d) Rough Wall, $\xi \approx 8$. (X) Longitudinal Separations. (O) Diagonal Separation (see text).

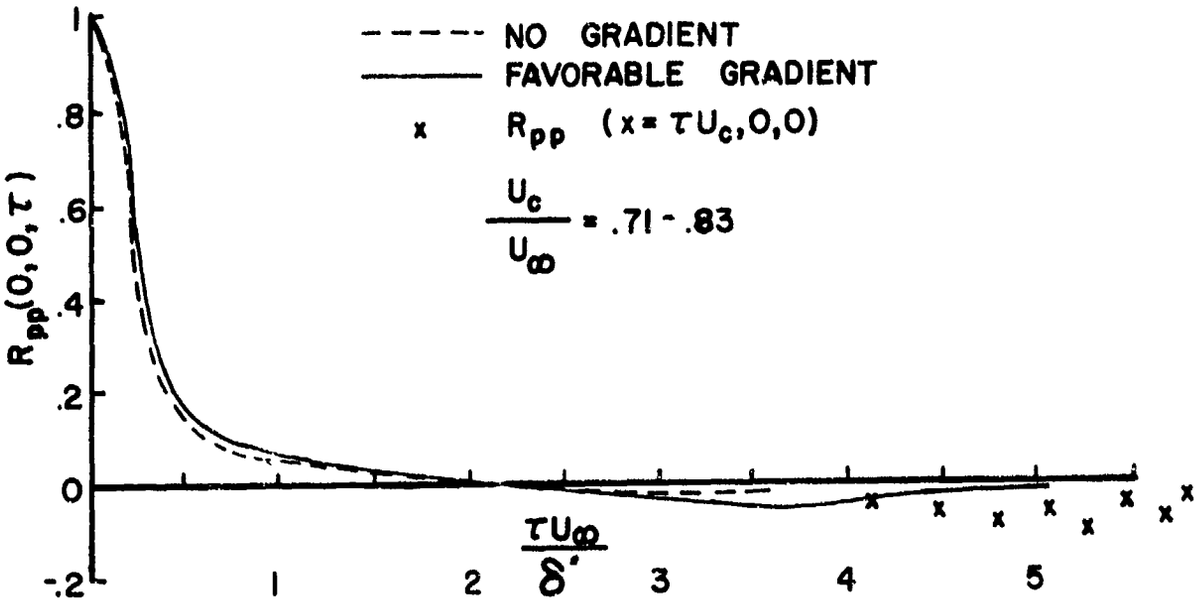

Figure 19. Time Autocorrelations over Smooth Walls.

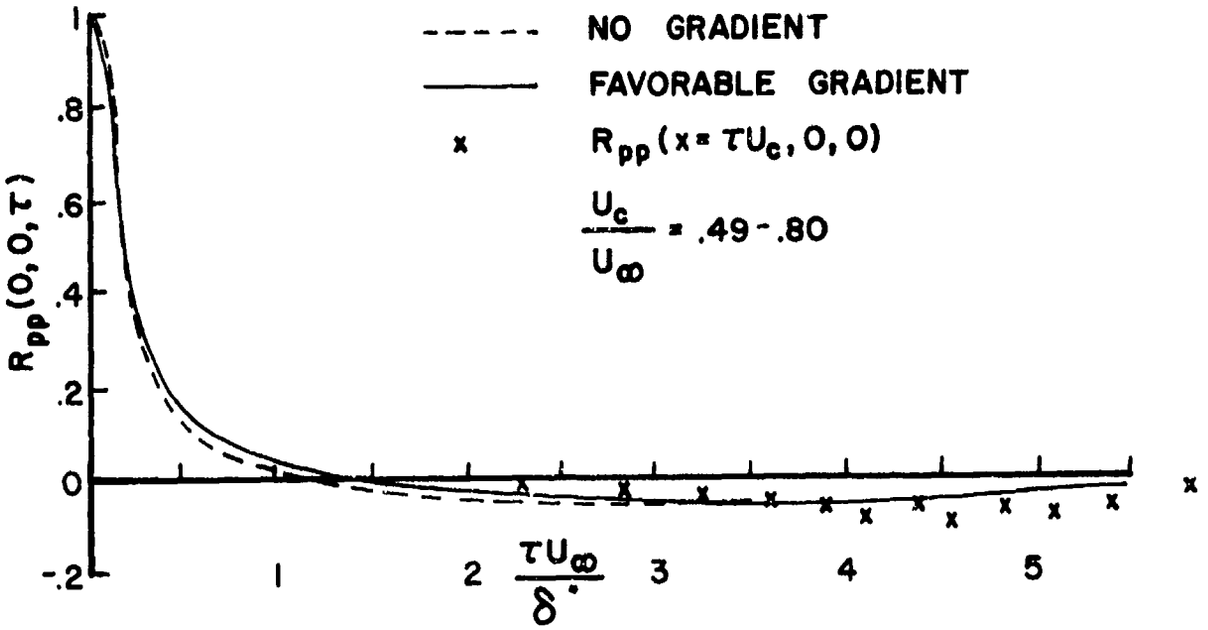

Figure 20. Time Autocorrelations over Rough Walls.

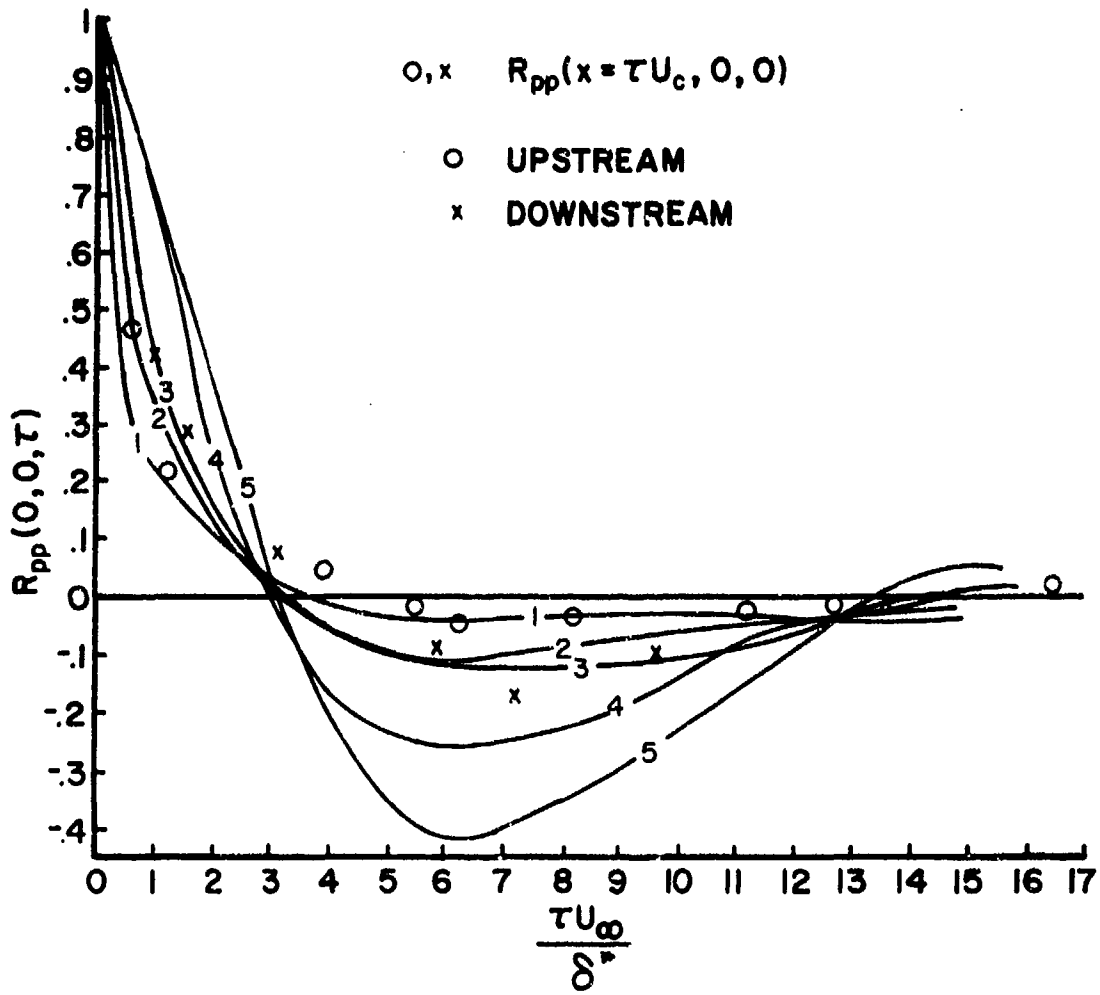

Figure 21. Time Autocorrelations over Smooth Walls with adverse gradient.

1	$\xi = 0$	O	$\xi \simeq 8$
2	10.7	x	$\xi \simeq 20$
3	15.3		
4	22.0		
5	24.6		

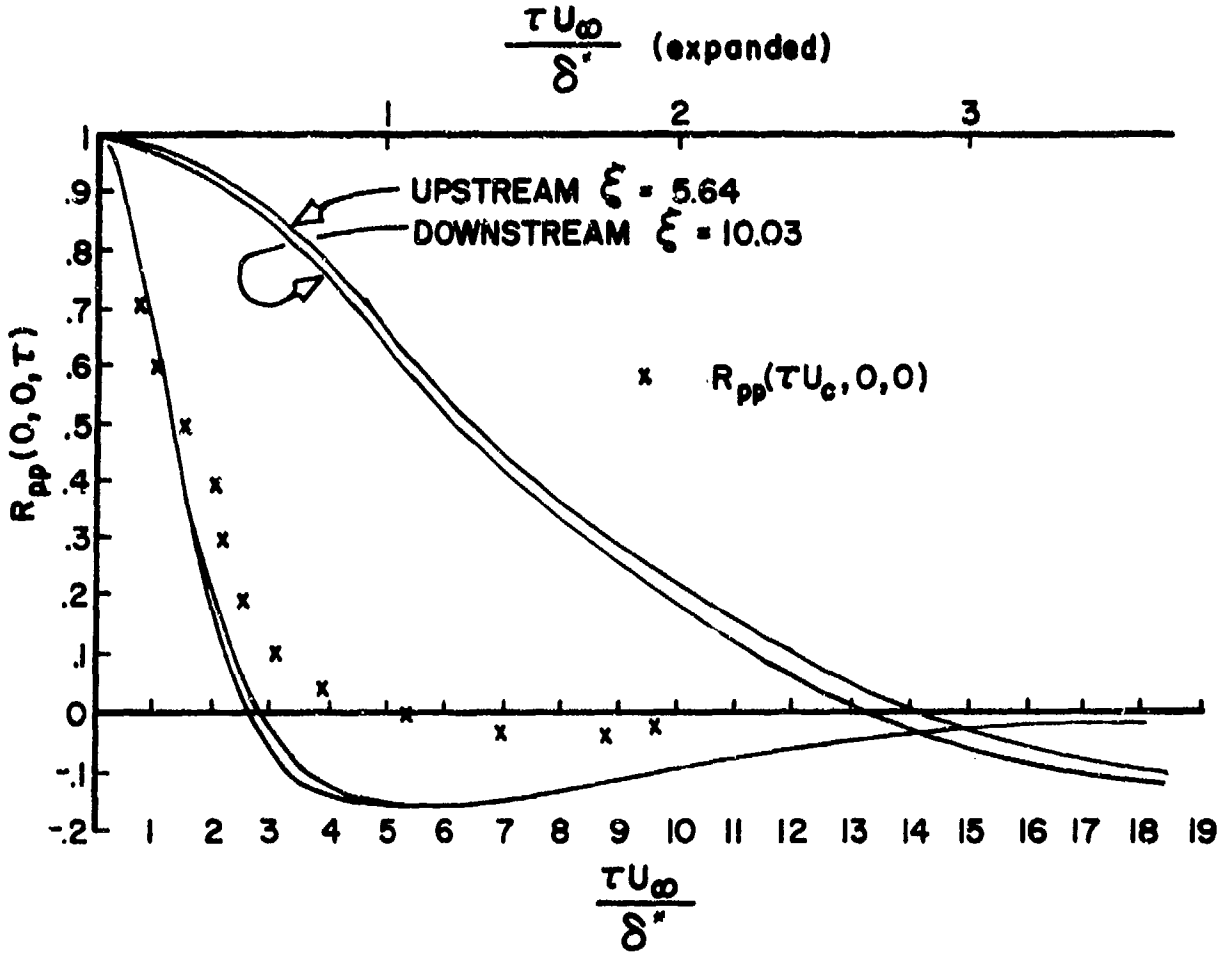

Figure 22. Time Autocorrelations over Rough Walls with Adverse Gradient.

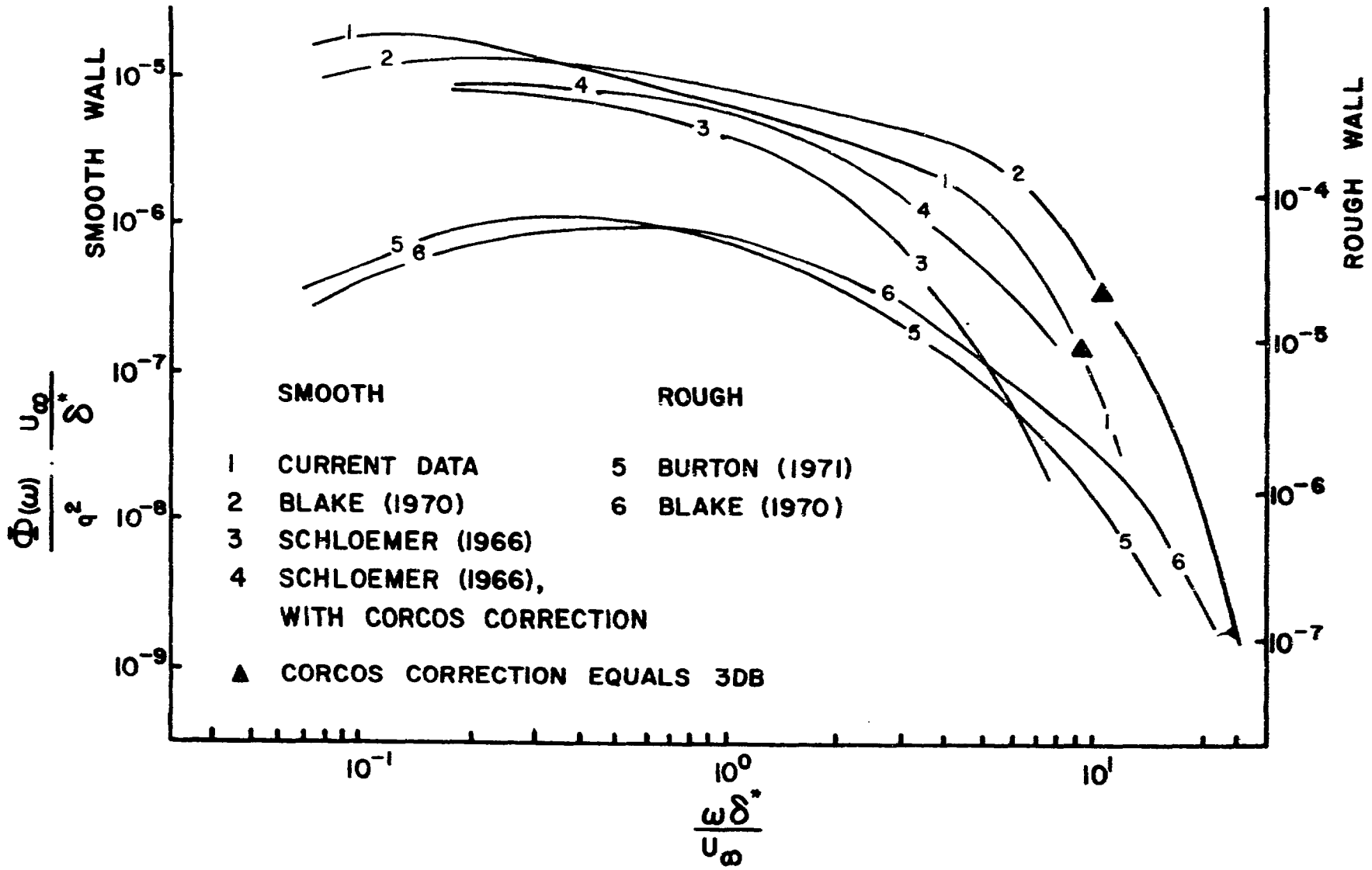

Figure 23. Wall Pressure Spectra. No Pressure Gradient. Outer Variable Scaling.

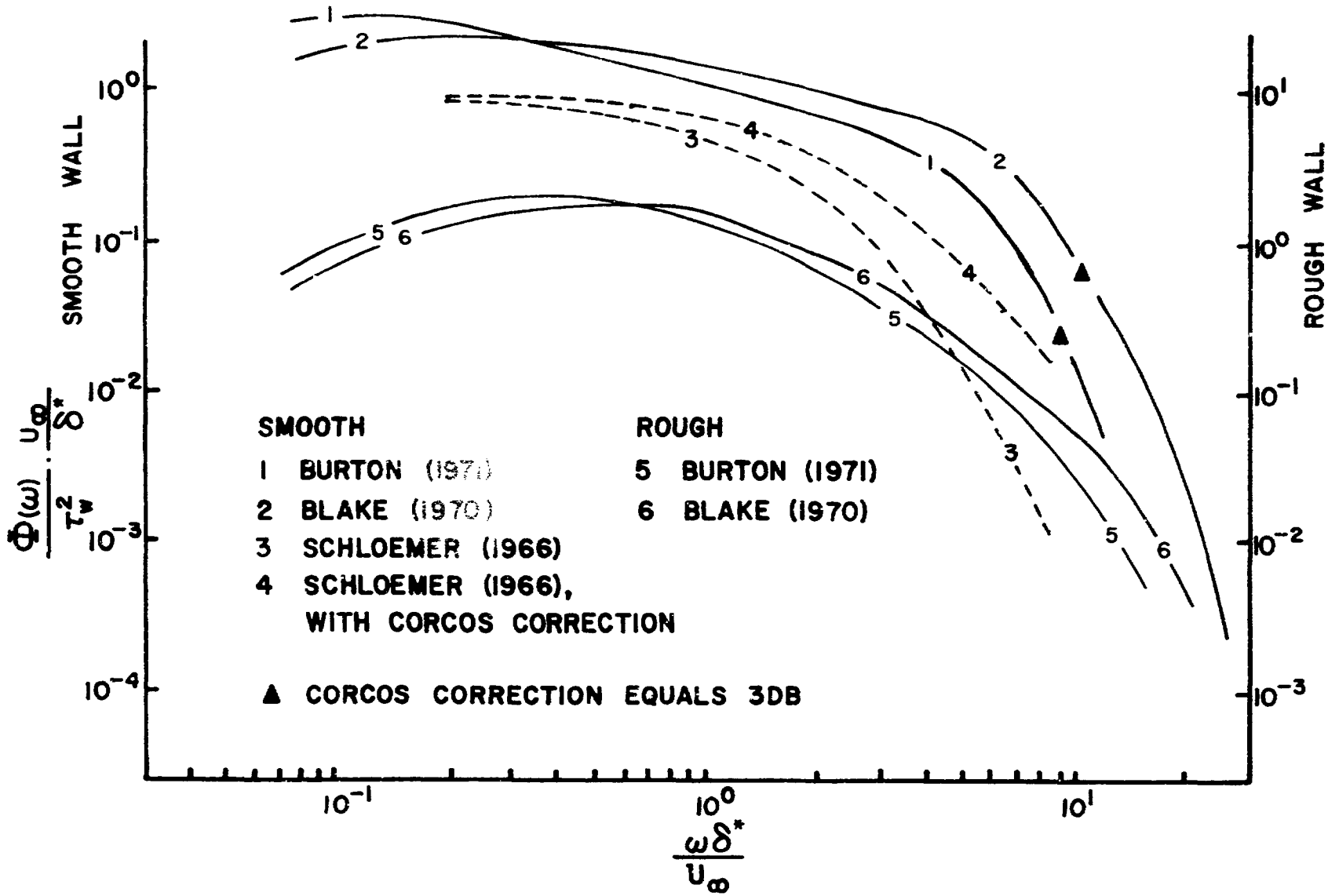

Figure 24. Wall Pressure Spectra. No Pressure Gradient. Pressure Amplitude Is Scaled on Mean Wall Shear Stress.

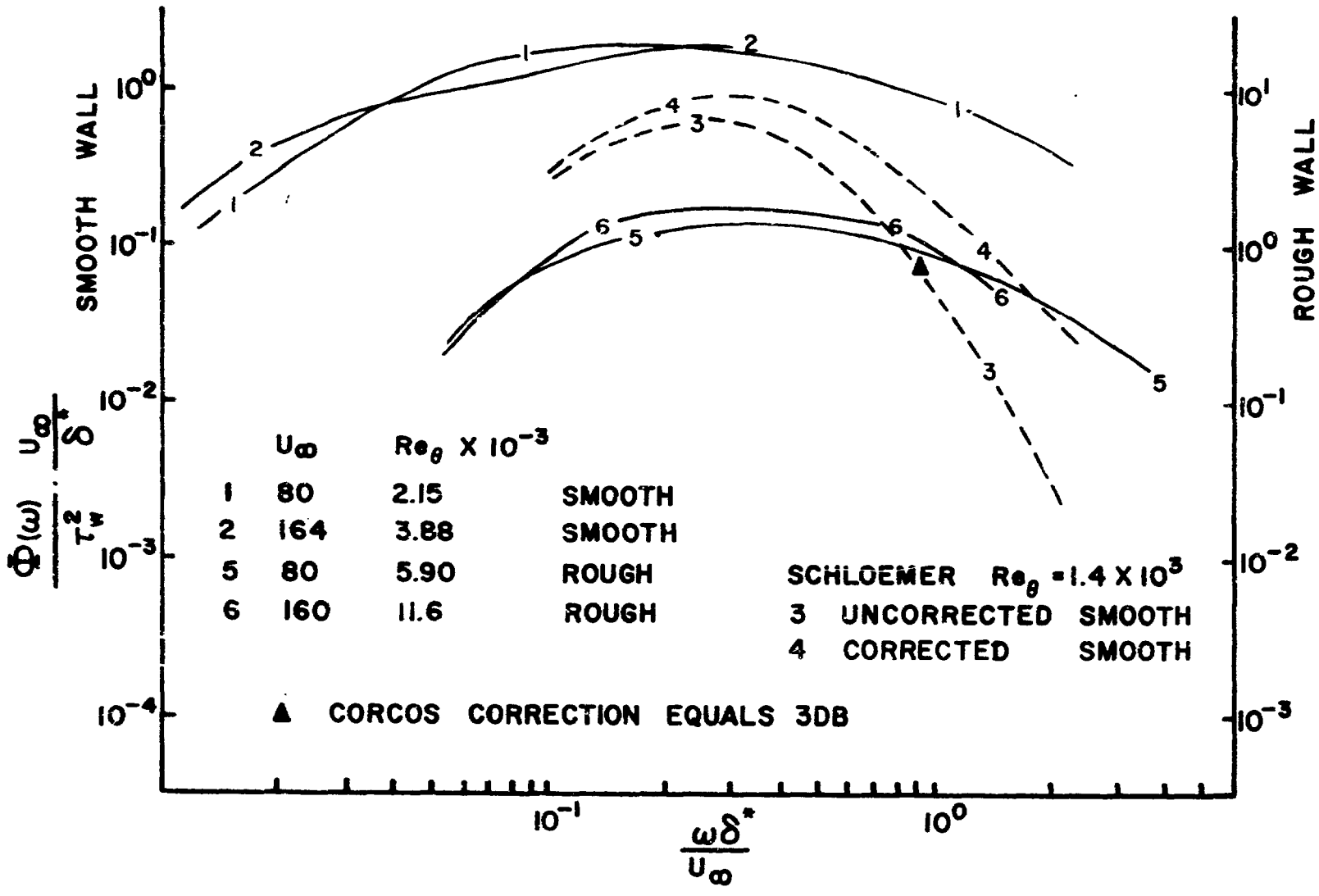

Figure 25. Wall Pressure Spectra. Favorable Pressure Gradient. Pressure Amplitude Is Scaled on Mean Wall Shear Stress.

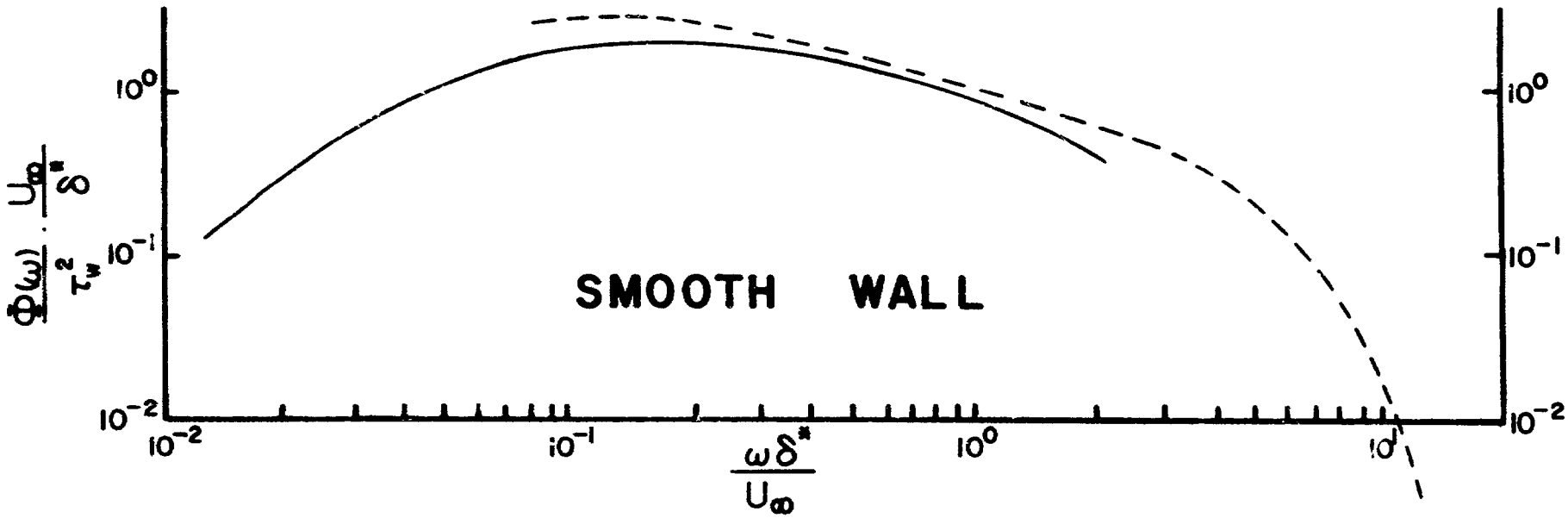

NEGATIVE GRADIENT

ZERO GRADIENT

WALL PRESSURE SPECTRA

Figure 26. Comparison of Smooth Wall Spectra for No-Gradient and Favorable (Negative) Gradient.

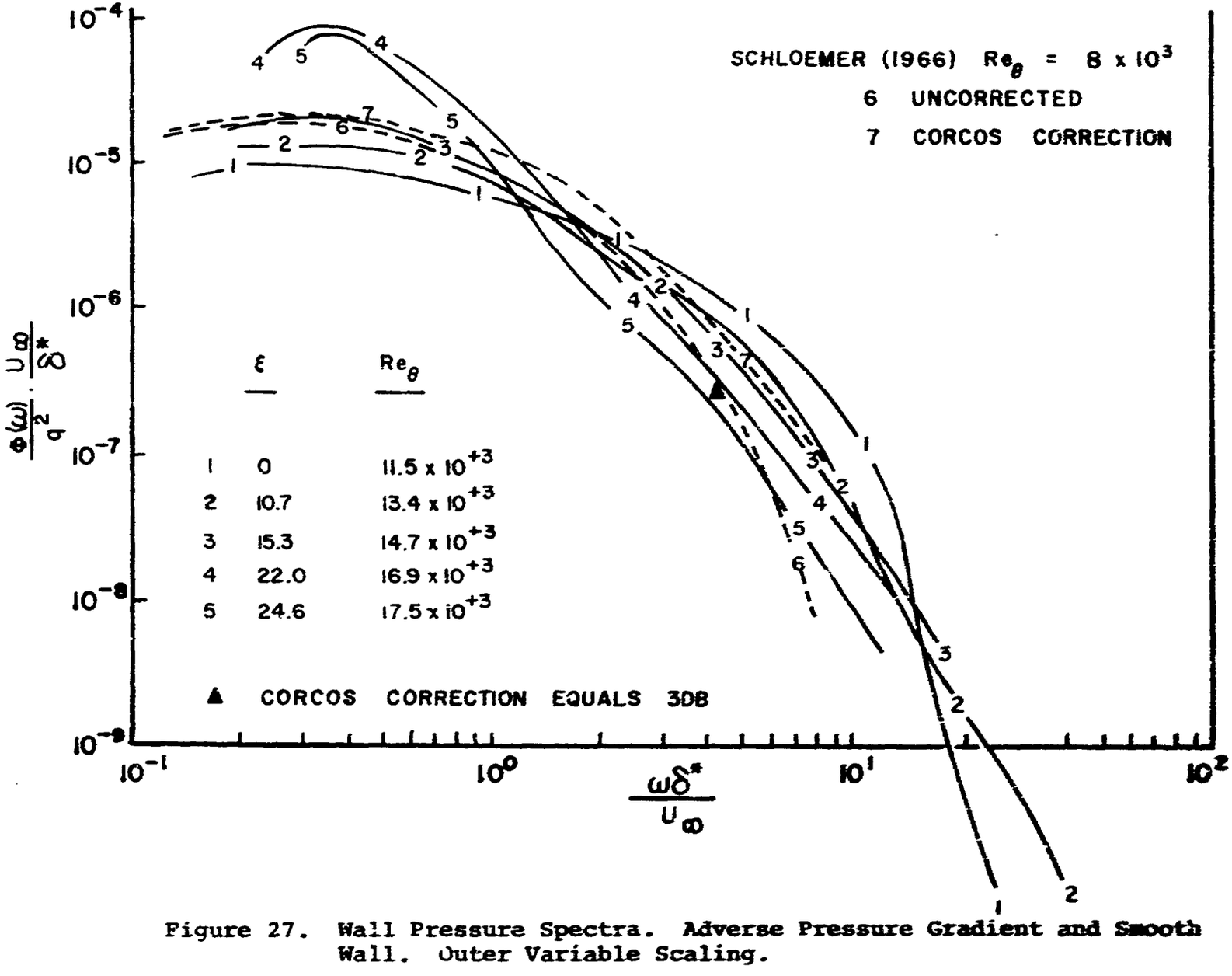

Figure 27. Wall Pressure Spectra. Adverse Pressure Gradient and Smooth Wall. Outer Variable Scaling.

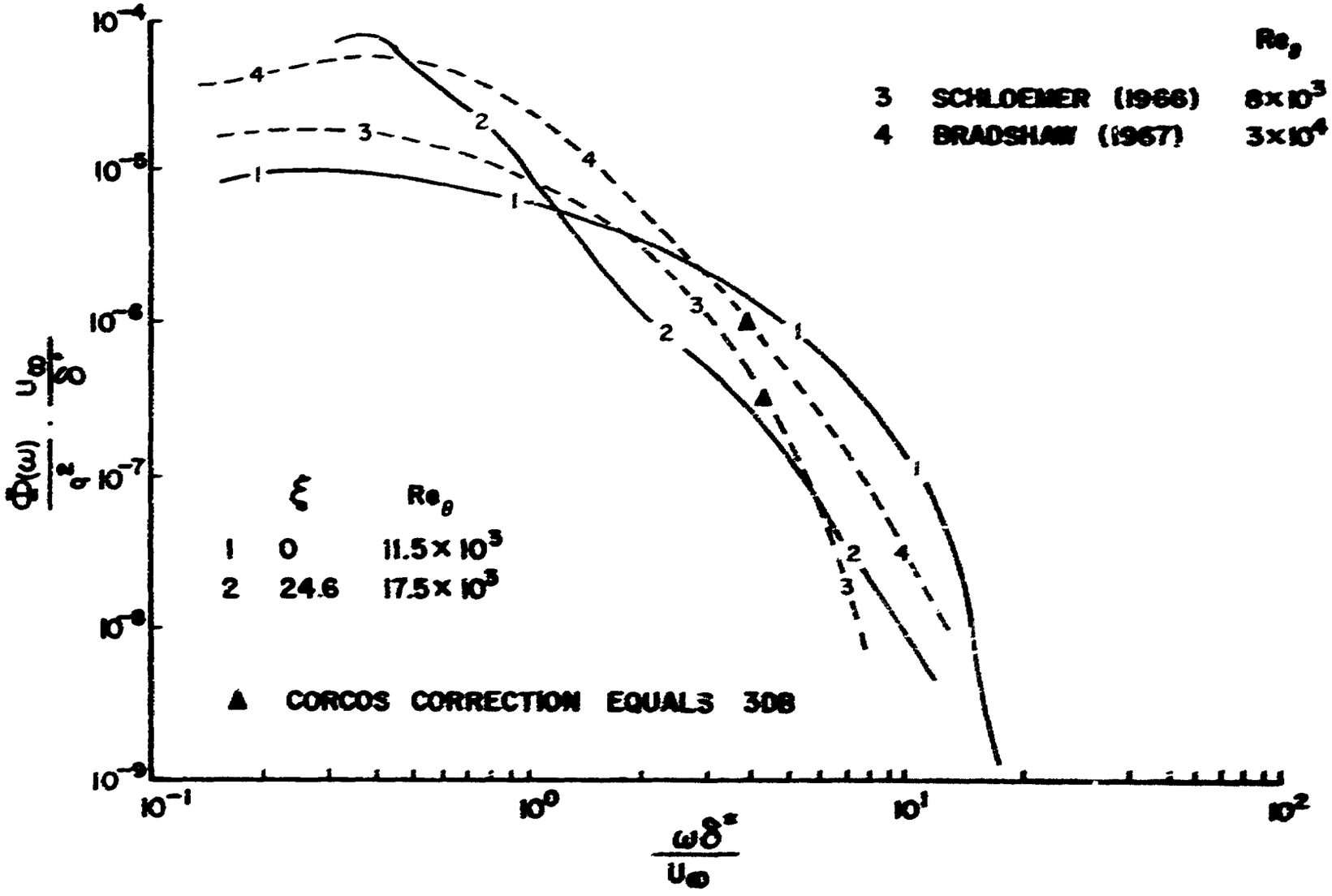

Figure 28. Wall Pressure Spectra. Adverse Pressure Gradient and Smooth Wall. Outer Variable Scaling.

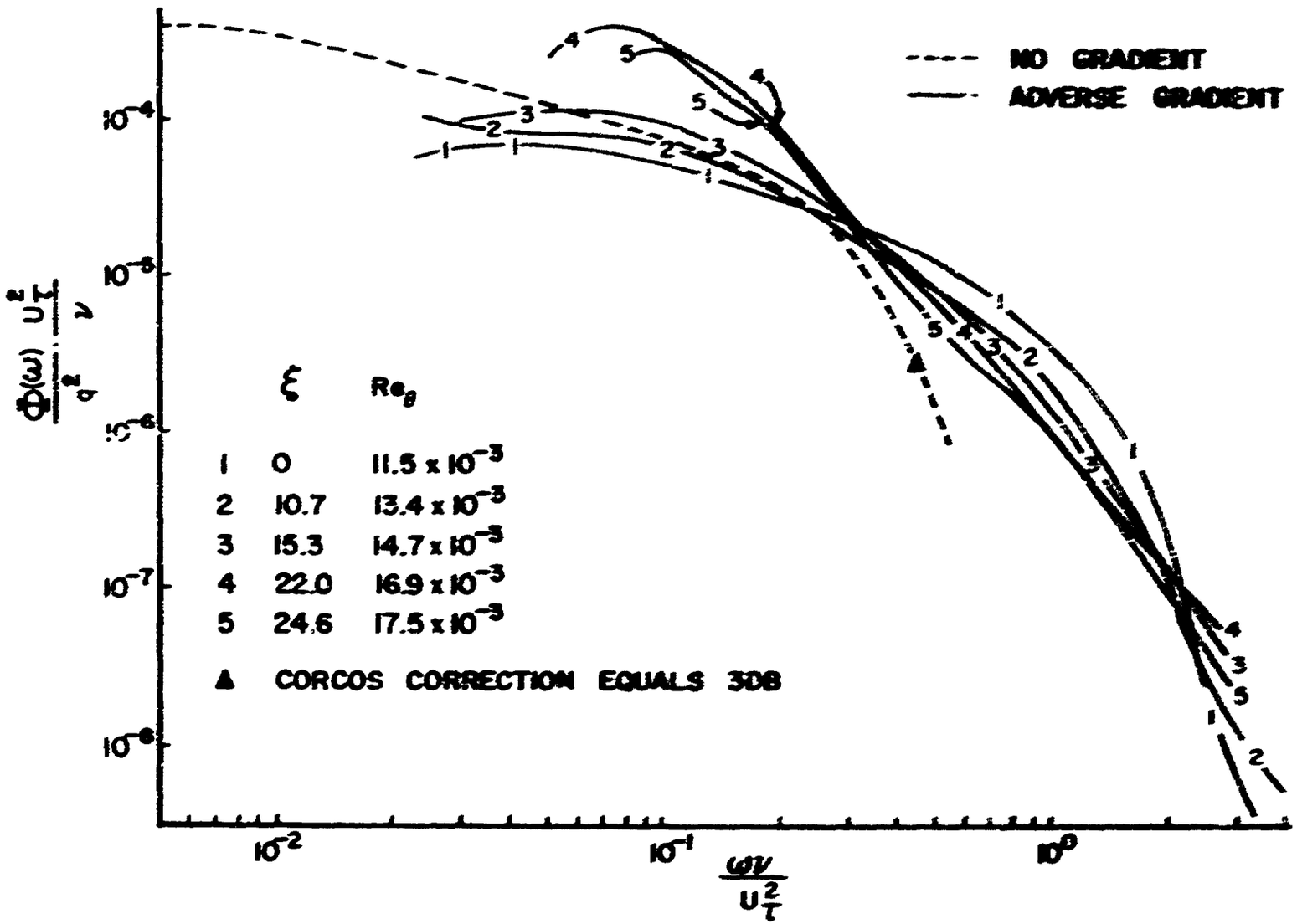

Figure 29. Comparison of Smooth Wall Spectra for No-Gradient and Adverse Gradient. Inner Variable Abscissa Scaling.

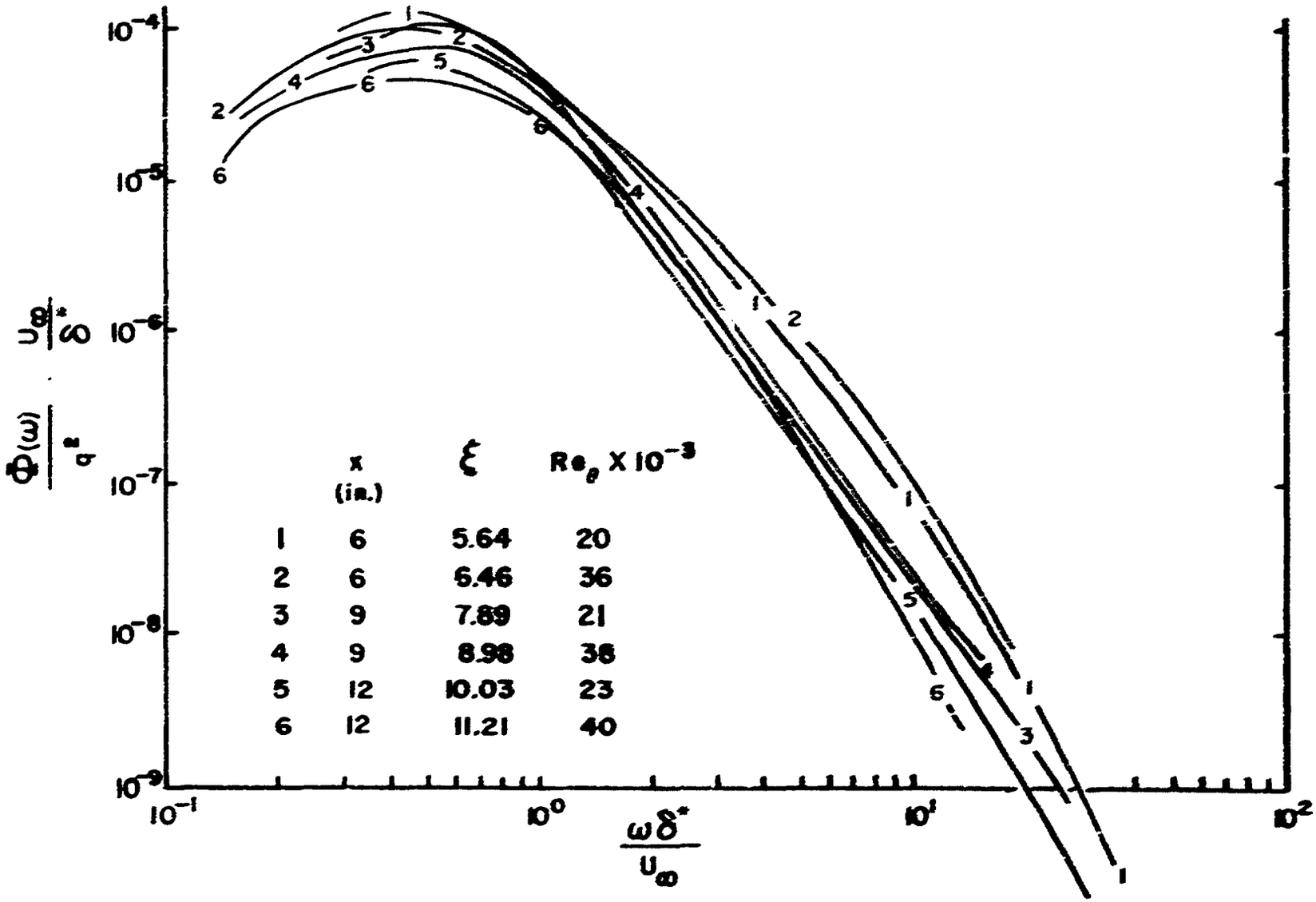

Figure 30. Wall Pressure Spectra. Adverse Pressure Gradient and Rough Wall.

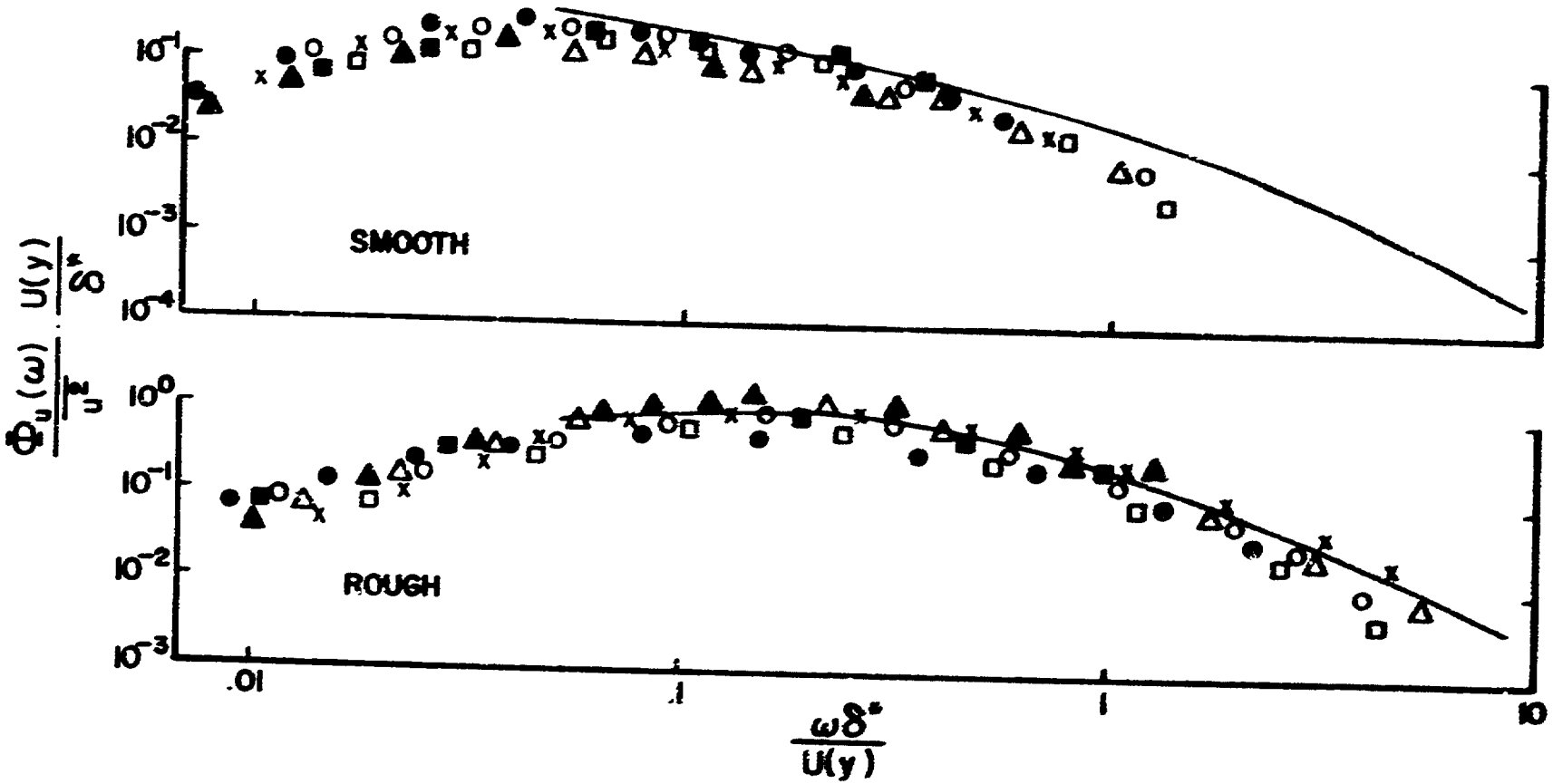

Figure 31. Longitudinal Turbulent Velocity Spectra. Solid Curves: No Gradient Blake (1970). Symbols: Favorable Gradient.

U_∞	y/δ^*	U_∞	y/δ^*	U_∞	y/δ^*
□ 80 ft/sec	.5			■ 160 ft/sec	.5
Δ 80	2.0	x 120 ft/sec	2	▲	2.0
O 80	6.4			●	6.4

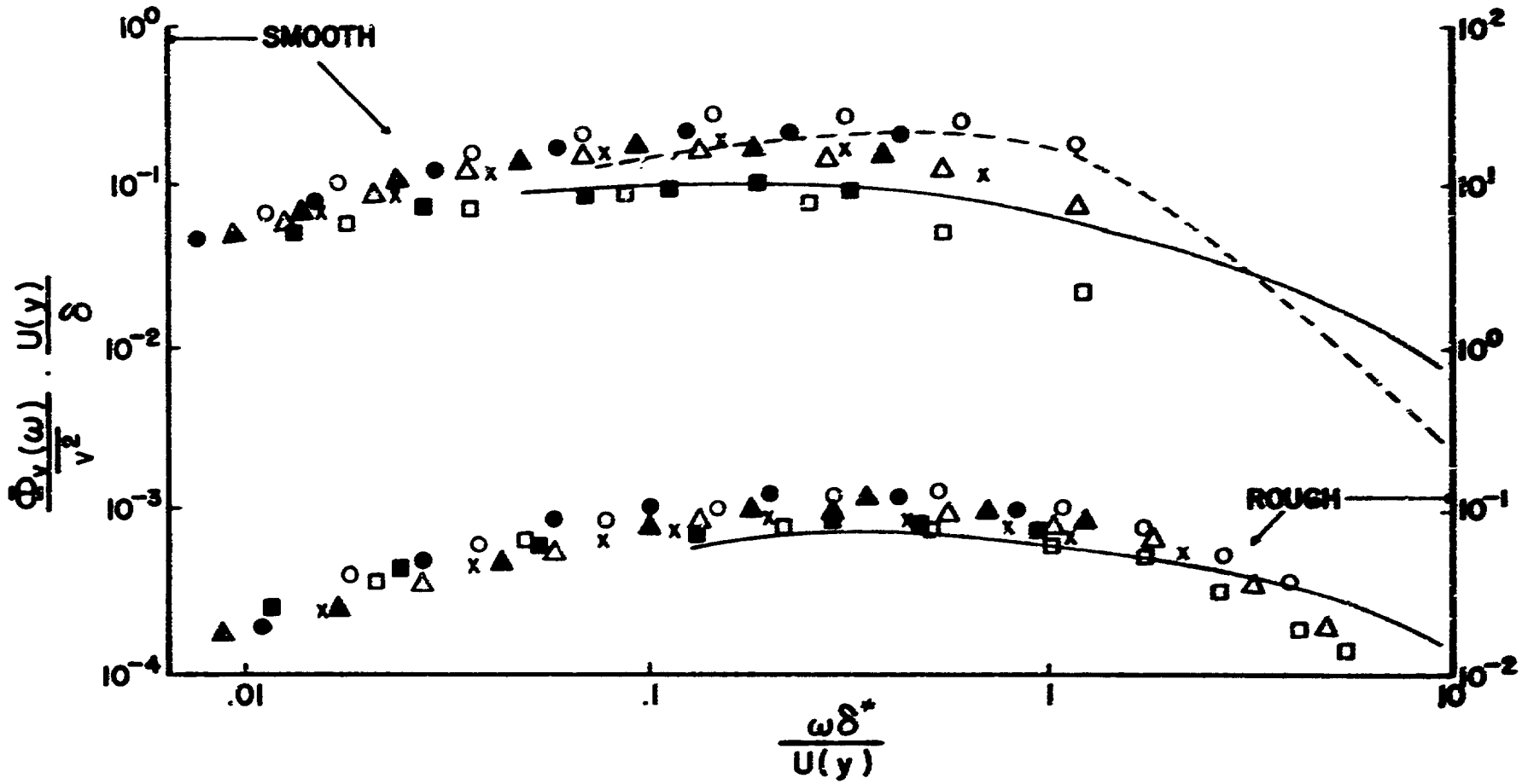

Figure 32. Normal Turbulent Velocity Spectra. Curves: No Gradient Blake (1970). Solid Curves: $y/\delta^*=2.5$ (rough), $=.6$ (smooth). Dashed Curve: $y/\delta^*=6.0$.

U_∞	y/δ^*	U_∞	y/δ^*	U_∞	y/δ^*
□ 80 ft/sec	.8			■ 160 ft/sec	.8
△ 80	2.0	x 120 ft/sec	2.0	▲ 160	2.0
○ 80	6.0			● 160	6.0

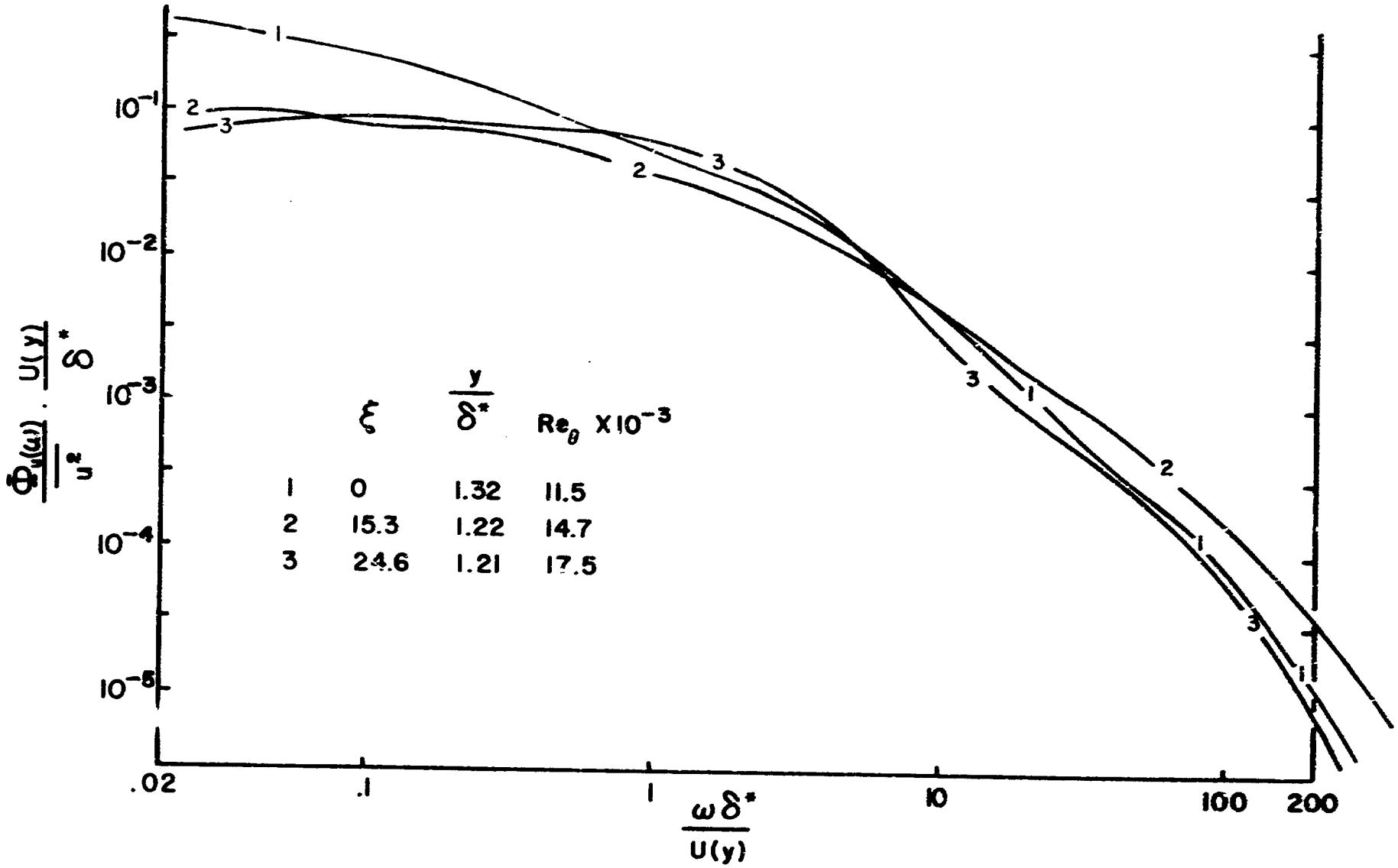

Figure 33. Longitudinal Turbulent Intensity Spectra. Adverse Pressure Gradient and Smooth Wall.

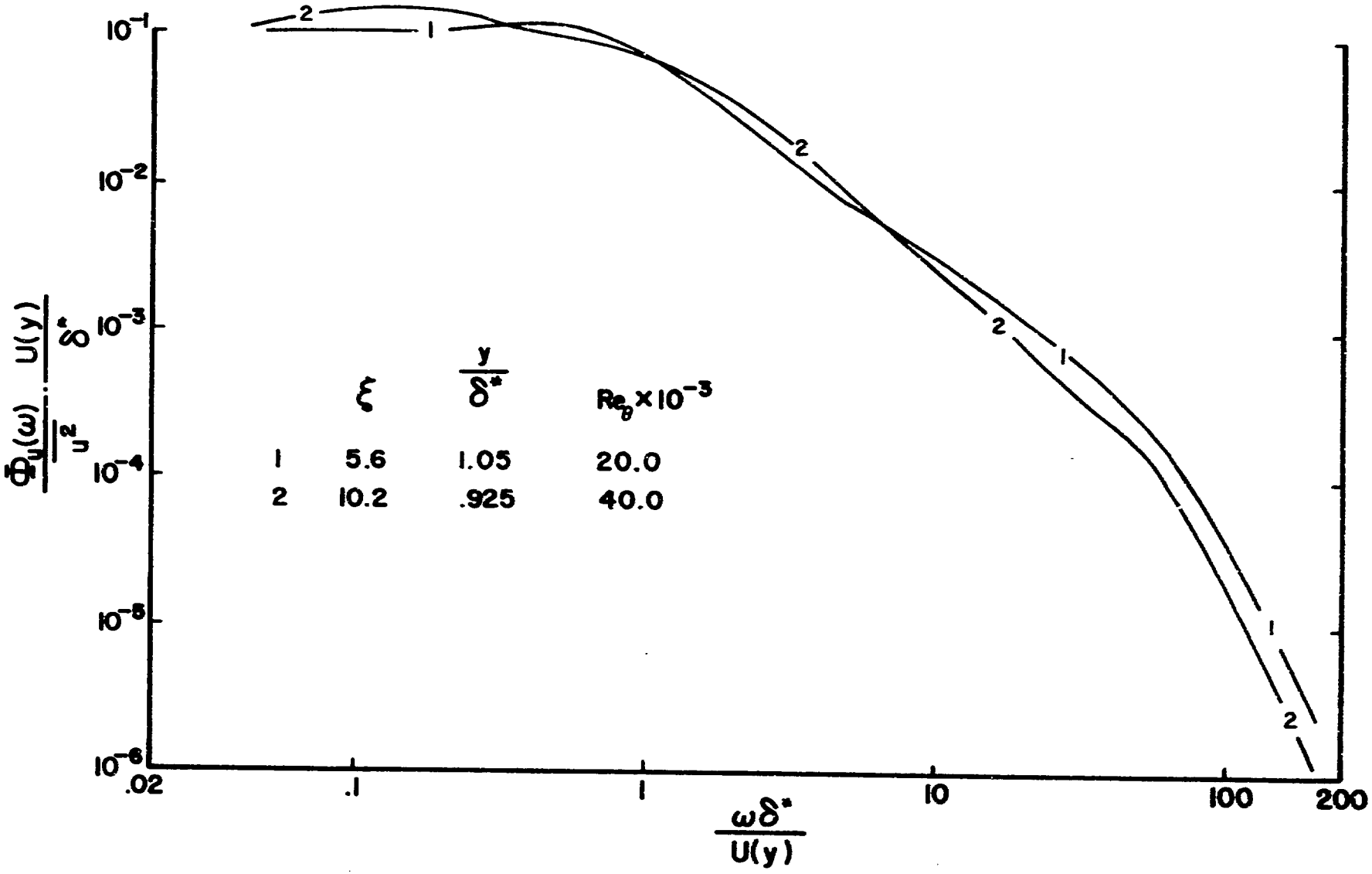

Figure 34. Longitudinal Turbulent Intensity Spectra. Adverse Pressure Gradient and Rough Wall.

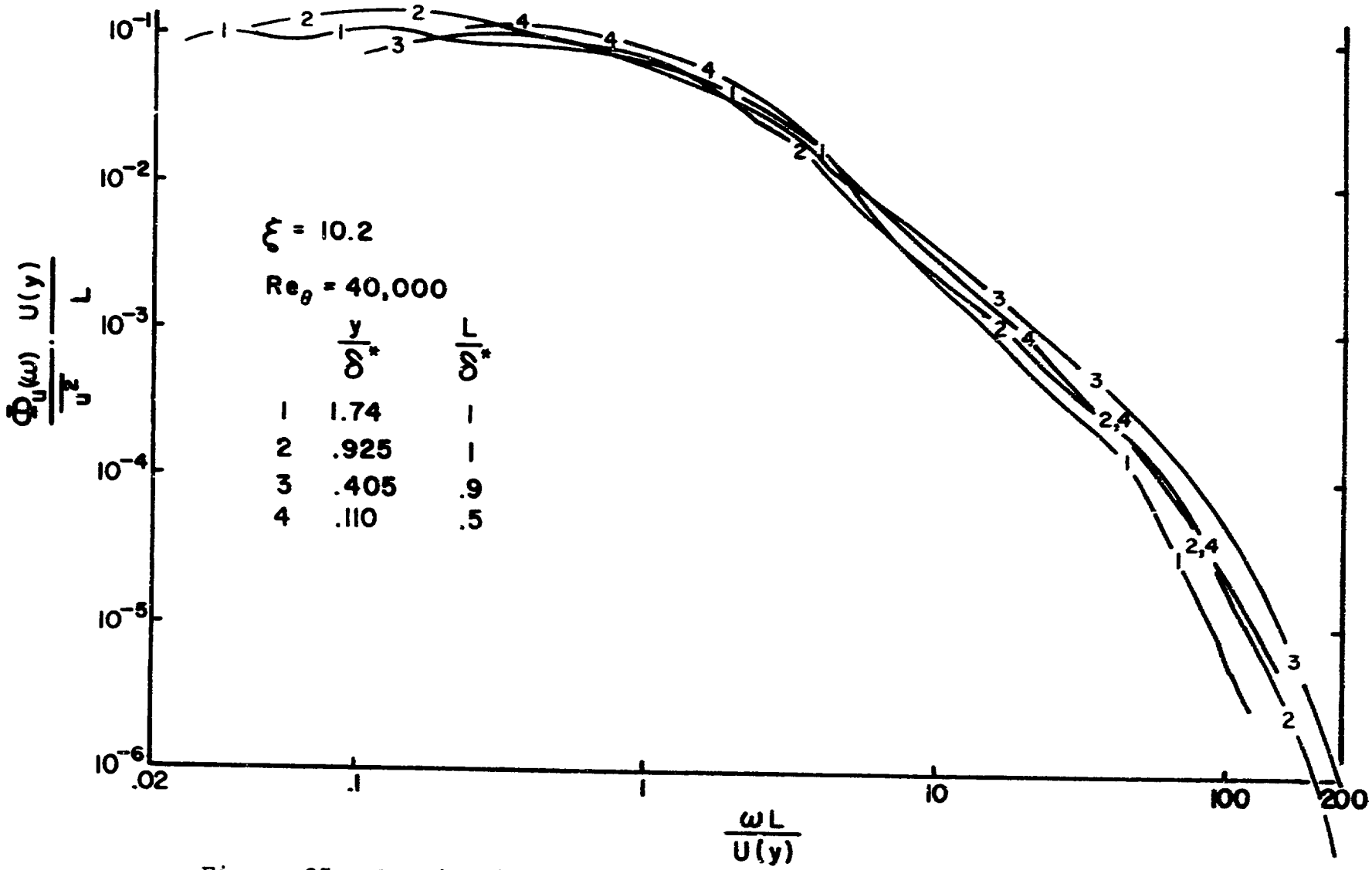

Figure 35. Longitudinal Turbulent Velocity Spectra. Adverse Gradient and Rough Wall.

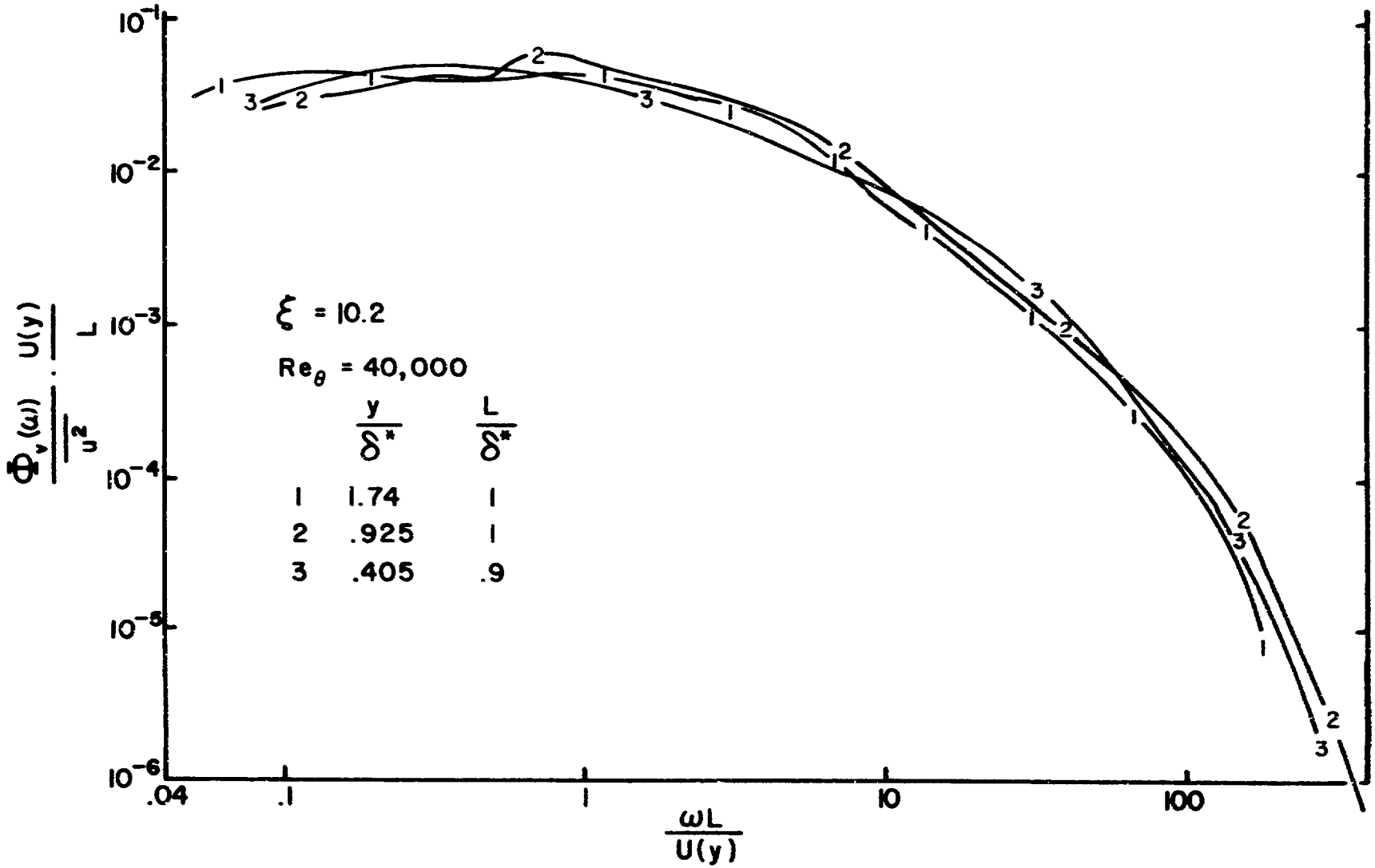

Figure 36. Normal Turbulent Velocity Spectra. Adverse Pressure Gradient and Rough Wall.

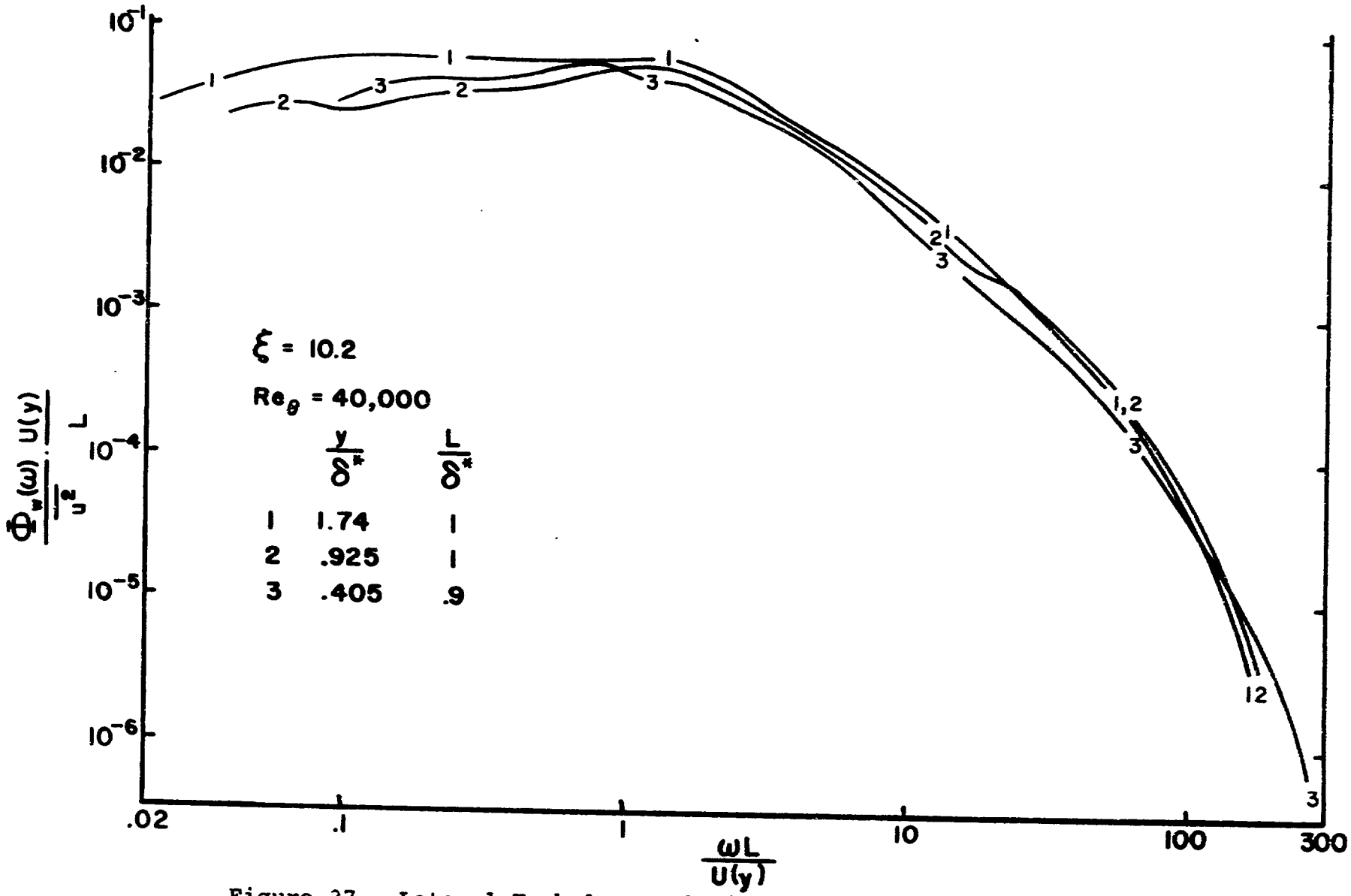

Figure 37. Lateral Turbulent Velocity Spectra. Adverse Pressure Gradient and Rough Wall.

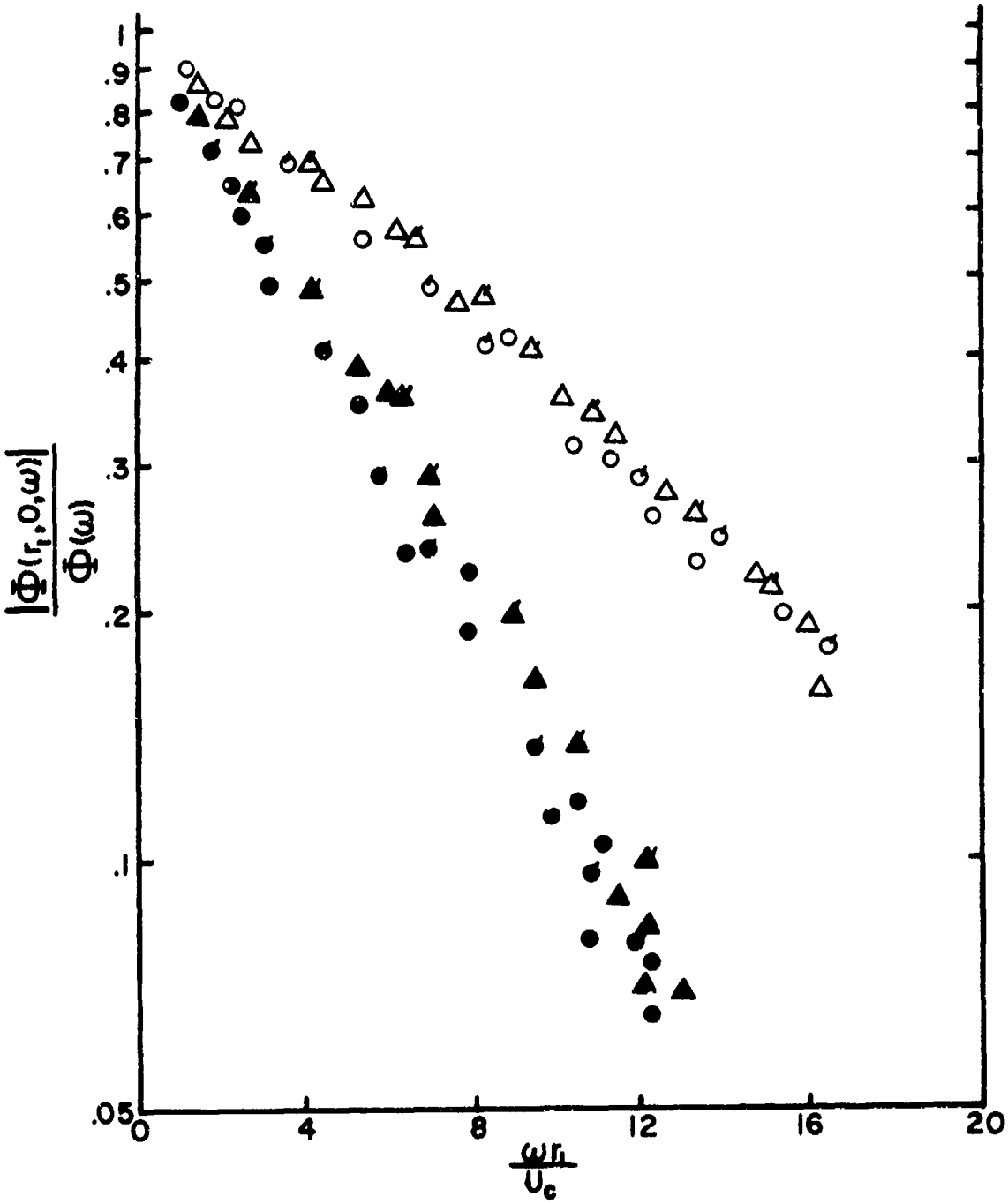

Figure 38. Longitudinal Cross-Spectral Density. Favorable Gradient. Circles: U_∞ = 120 ft/sec; Triangles: U_∞ = 80 ft/sec. Flagged Symbols: r_1= .875 in.; Unflagged Symbols: r_1 = .375 in. Filled Symbols: Rough Wall; Unfilled Symbols: Smooth Wall.

FIGURE 39 LEGEND

		AUTHOR	WALL TYPE	PRESSURE GRADIENT
———	1	Blake (1970)	smooth	none
------	2	Schloemer (1966)	smooth	none
———	3	Figure 38	smooth	favorable
———	4	Blake (1970)	rough	none
------	5	Schloemer (1966)	smooth	favorable
———	6	Figure 38	rough	favorable

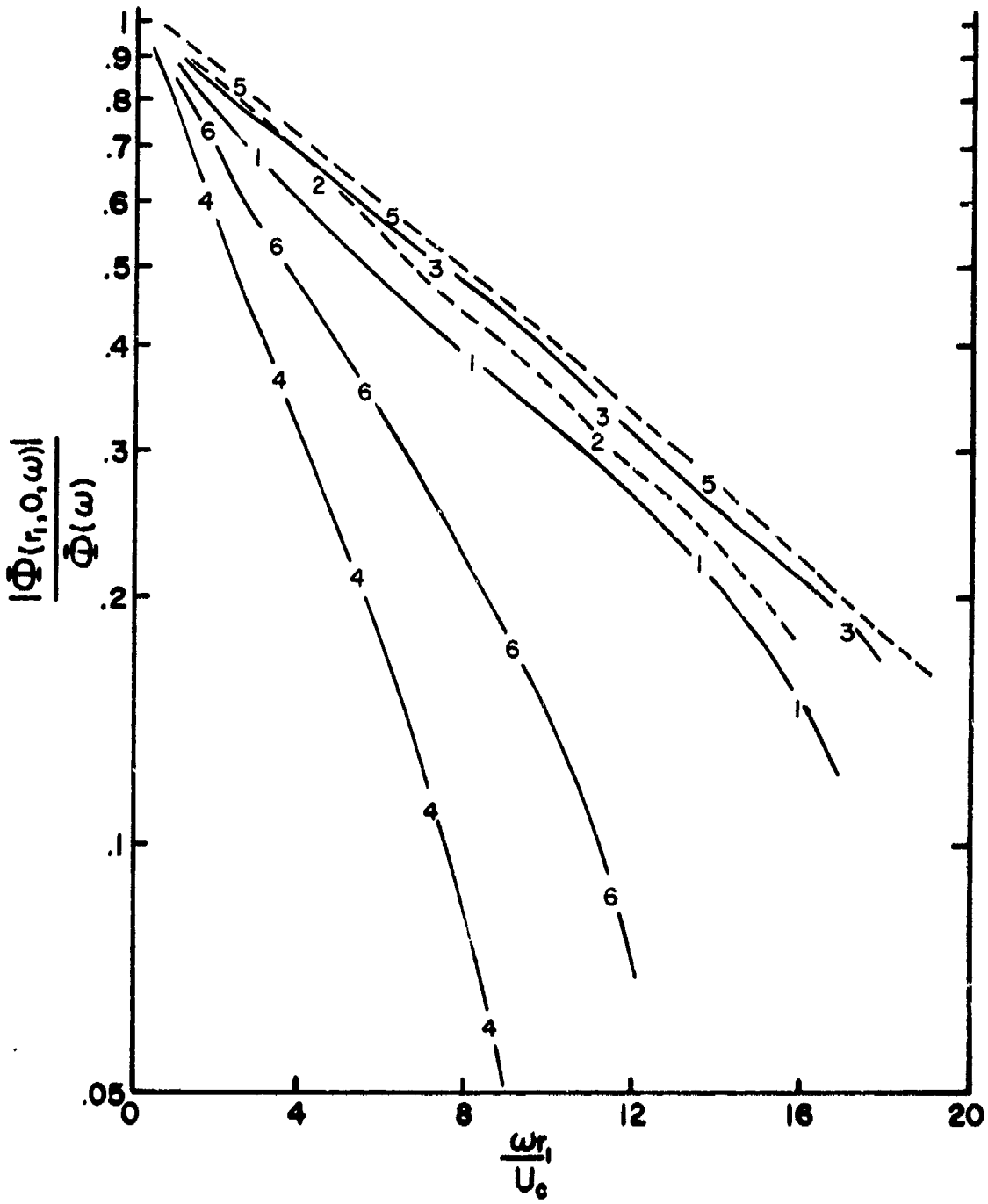

Figure 39. Longitudinal Cross-Spectral Density. Favorable Gradient and No-Gradient Comparison. The legend is on the facing page.

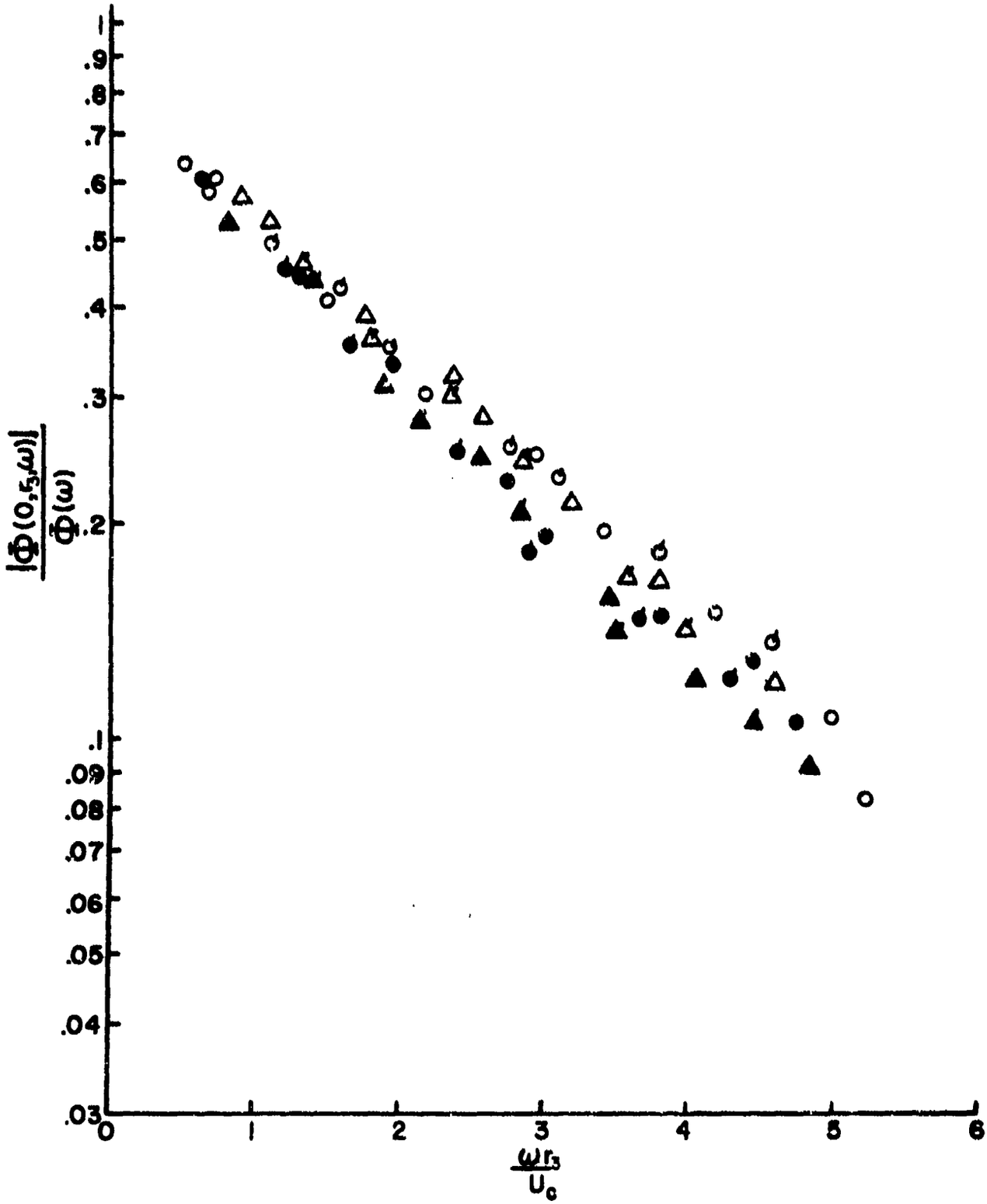

Figure 40. Lateral Cross-Spectral Density. Favorable Gradient. Circles: U_∞ = 120 ft/sec; Triangles: U_∞ = 80 ft/sec. Flagged Symbols: r_3 = .875 in.; Unflagged Symbols: r_3 = .375 in. Gilled Symbols: Rough Wall; Unfilled Symbols: Smooth Wall.

FIGURE 41 LEGEND

		AUTHOR	WALL TYPE	PRESSURE GRADIENT
— — — —	1	Blake (1970)	smooth	none
- - - - - -	2	Schloemer (1966)	smooth	none
————	3	Figure 40	smooth	favorable
————	4	Blake (1970)	rough	none
· - - - - -	5	Schloemer (1966)	smooth	favorable
————	6	Figure 40	rough	favorable

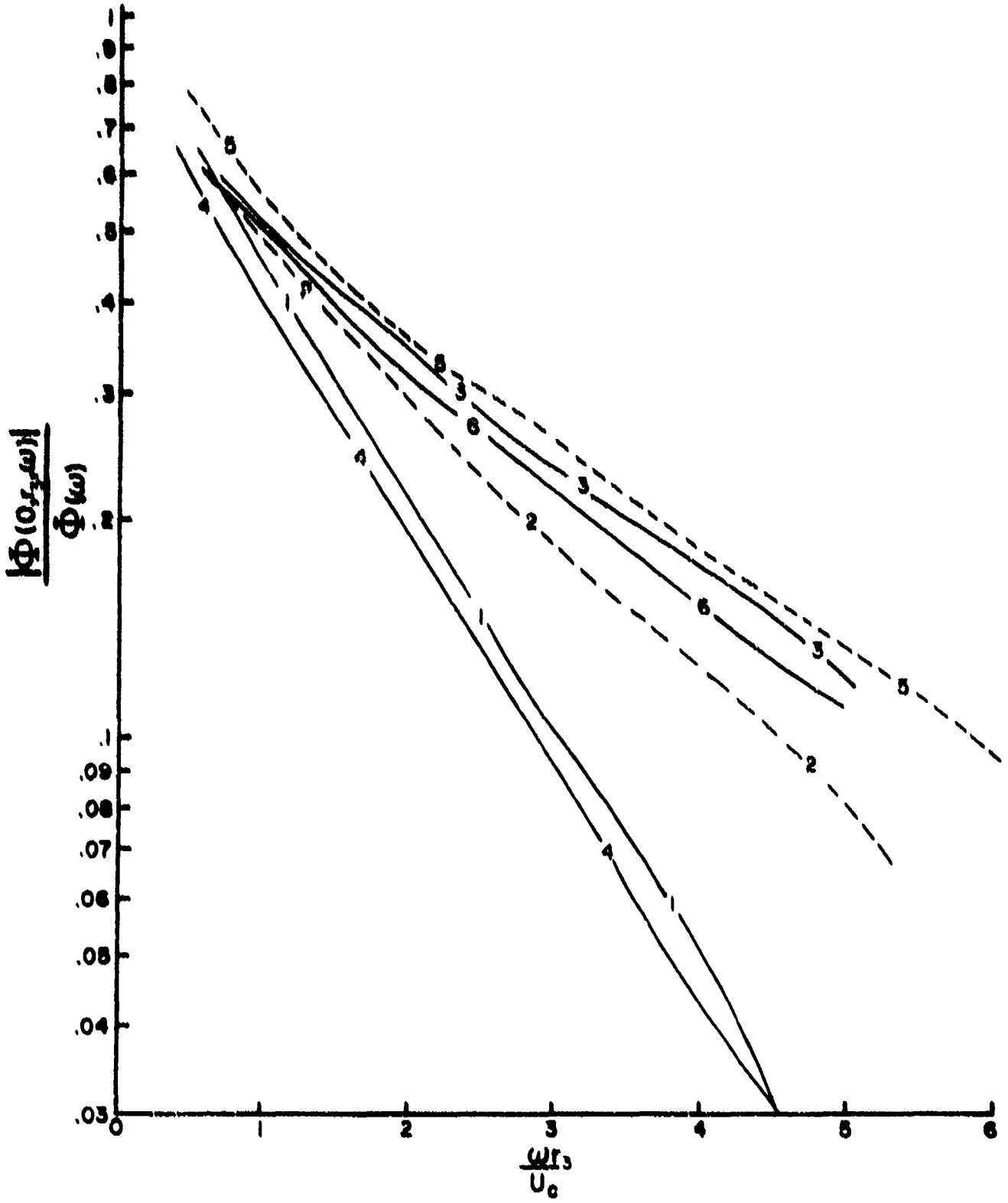

Figure 41. Lateral Cross-Spectral Density. Favorable Gradient and No-Gradient Comparison. The legend is on the facing page.

FIGURE 42 LEGEND

------- Schloemer (1966)

	ξ	$\Delta\xi$	$\Delta\omega$
A	13	4.7	4 Hz
B	11	1.2	4
C	22.1	.68	4
D	23.5	2.4	4
E	13.0	4.7	40

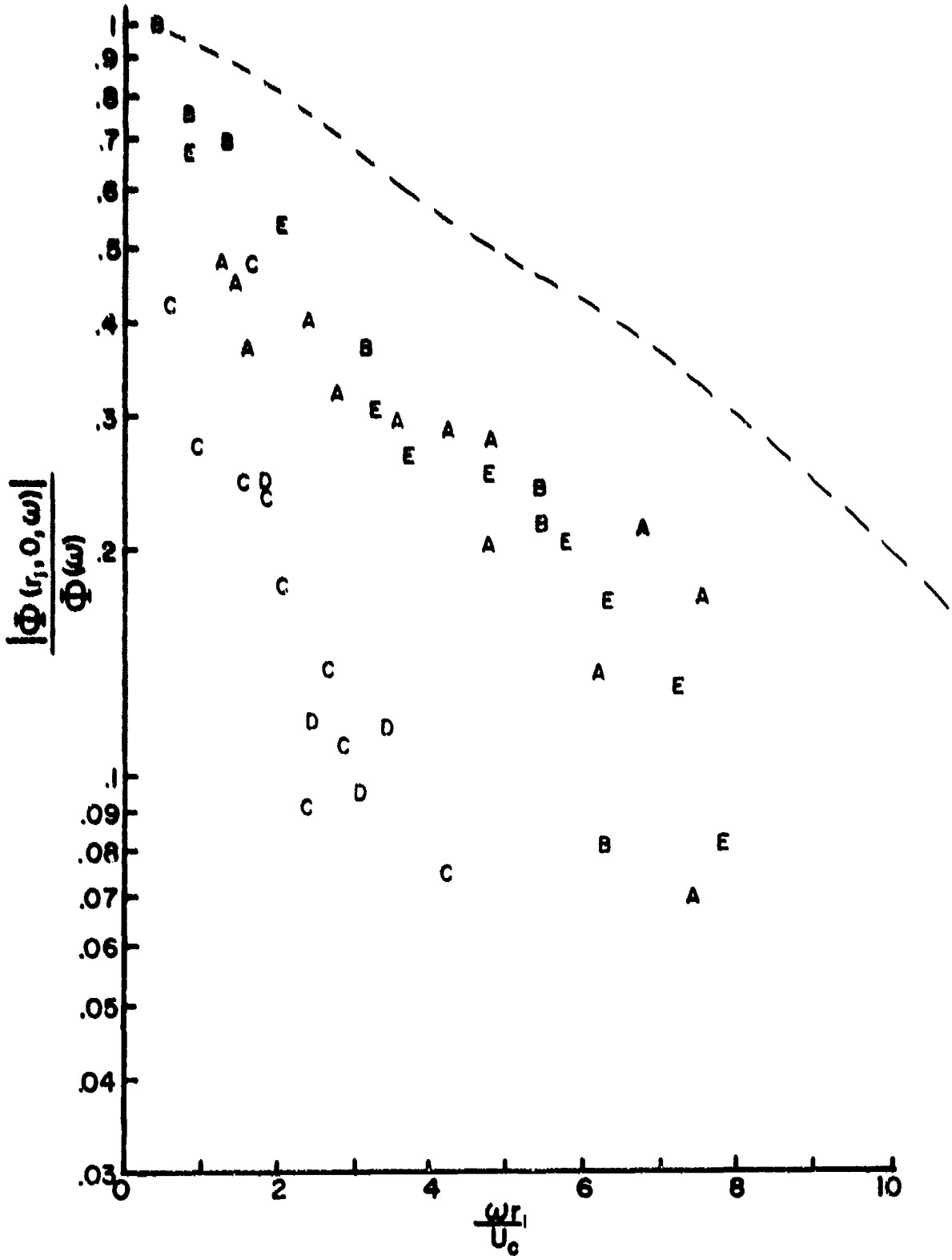

Figure 42. Longitudinal Cross-Spectral Density. Adverse Gradient and Smooth Wall. The legend is on the facing page.

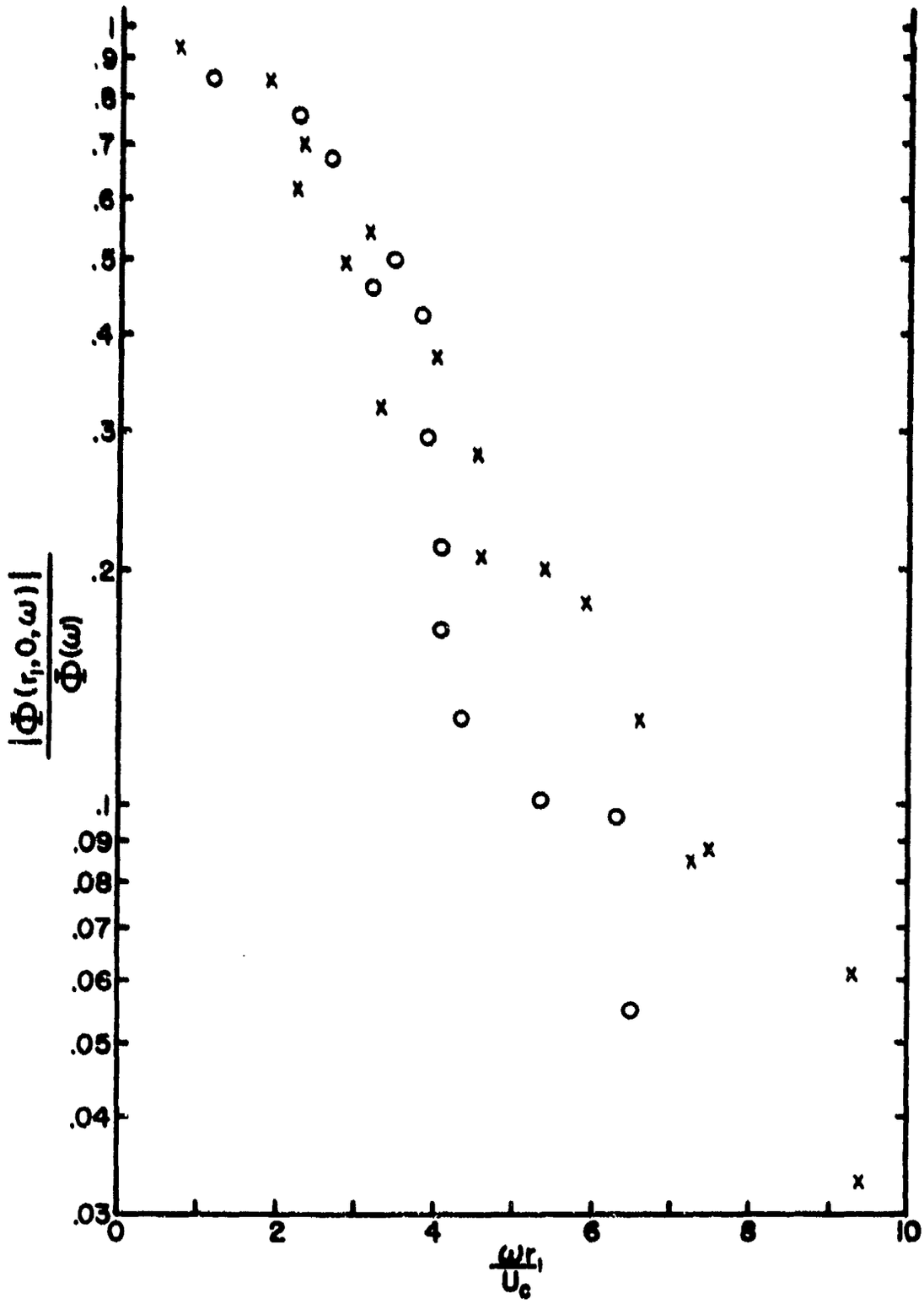

Figure 43. Longitudinal Cross-Spectral Density. Adverse Pressure Gradient and Rough Wall. $\xi \simeq 6$.

X $\Delta\xi = .45$

O $\Delta\xi = 1.6$

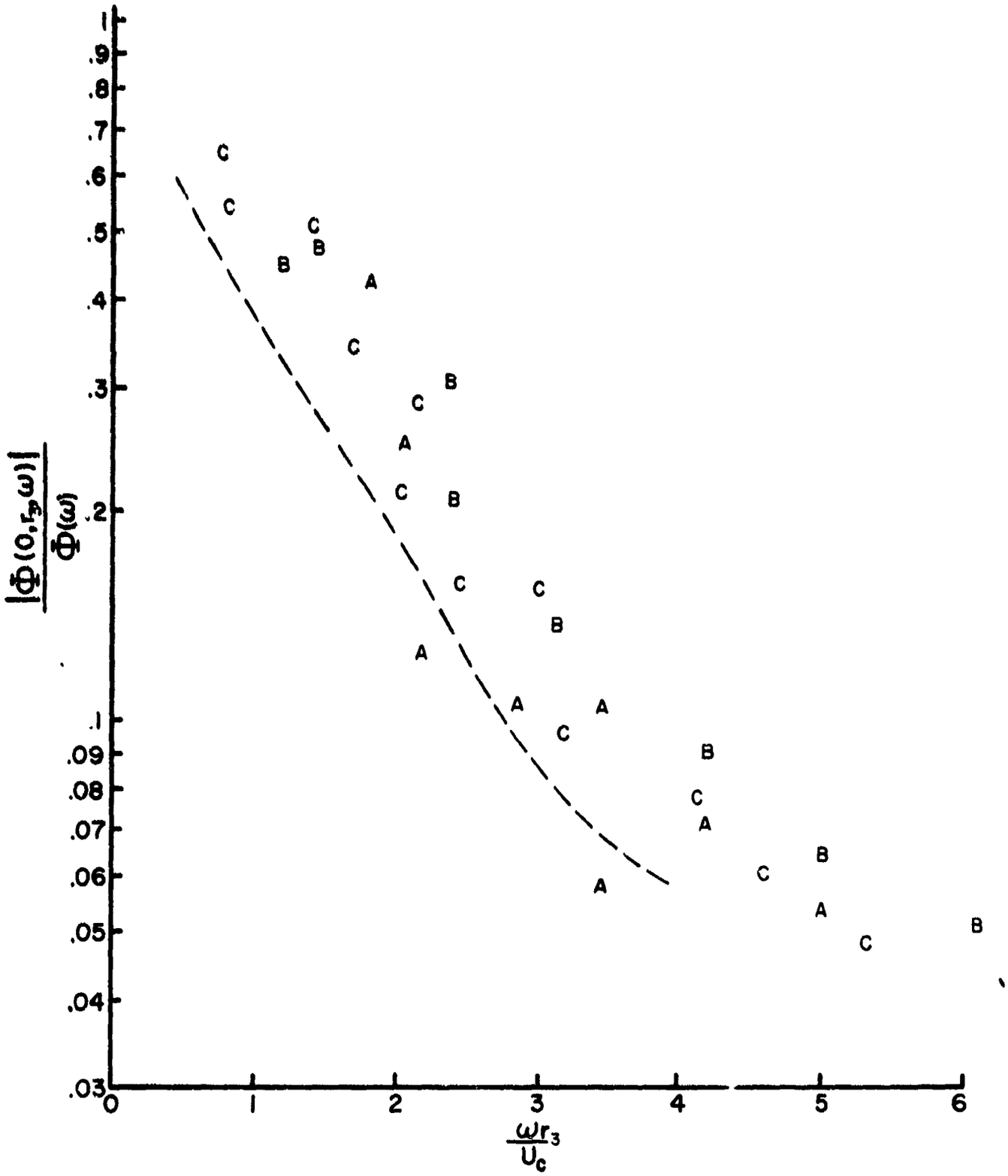

Figure 44. Lateral Cross-Spectral Density. Adverse Gradient.

(A) Smootn, $\xi \approx 24.6$, $\Delta\xi = 2.4$ (C) Rough, $\xi \approx 8$

(B) Smooth, $\xi \approx 15.3$, $\Delta\xi = 4.2$ -- Schloemer (1966), Smooth

TABLE 3

FAVORABLE GRADIENTS

This table shows nondimensional longitudinal separations in terms of the dimensional separations, freestream velocities, and wall condition. This table applies to Figures 45 and 46.

Wall Type	U_∞	δ^* \ r_1	.375 in	.875 in.	3.00 in.	5.50 in.
Smooth □	80 ft/sec	.064 in.	5.86	15.6	46.8	
O	120	.061	6.15	14.3	49.2	
X	164	.059	6.36	14.8	50.8	
Rough □	80	.234	1.60	3.74	12.8	23.5
O	120	.230	1.63	3.80	13.0	23.9
X	160	.226	1.66	3.87	13.2	24.3

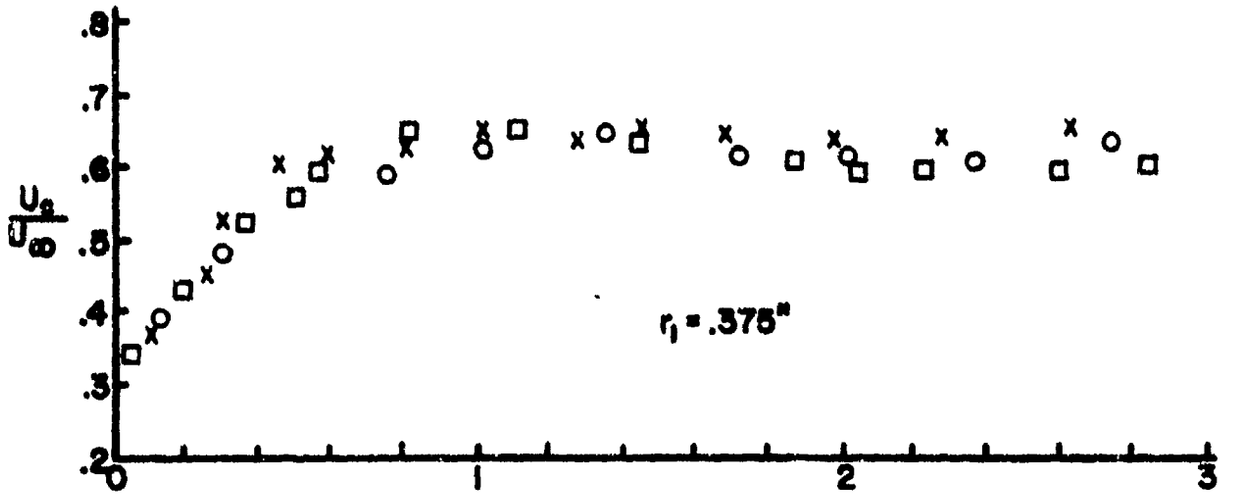

Figure 45a

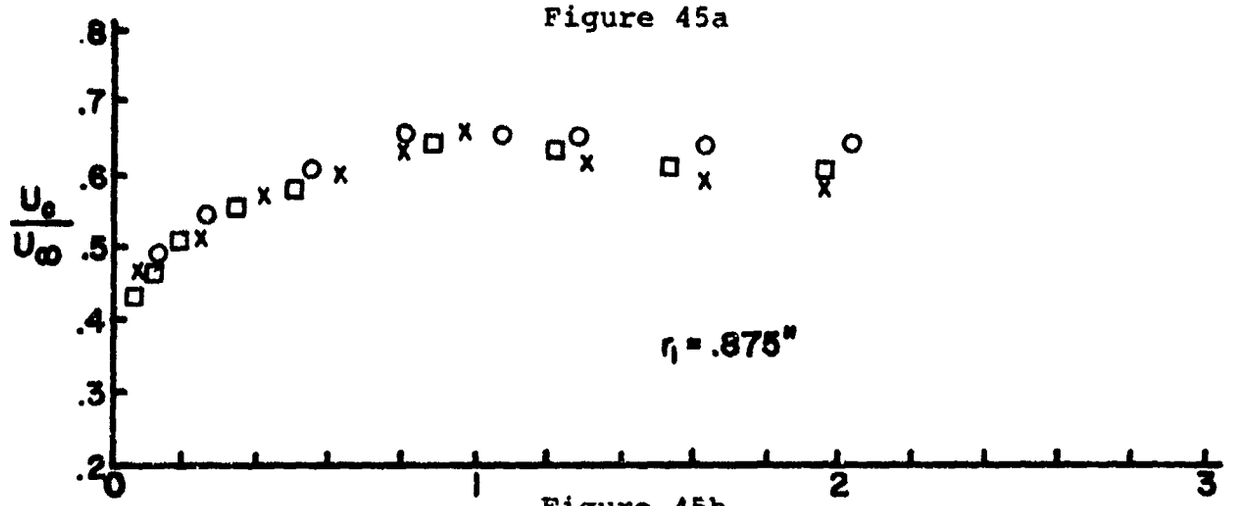

Figure 45b

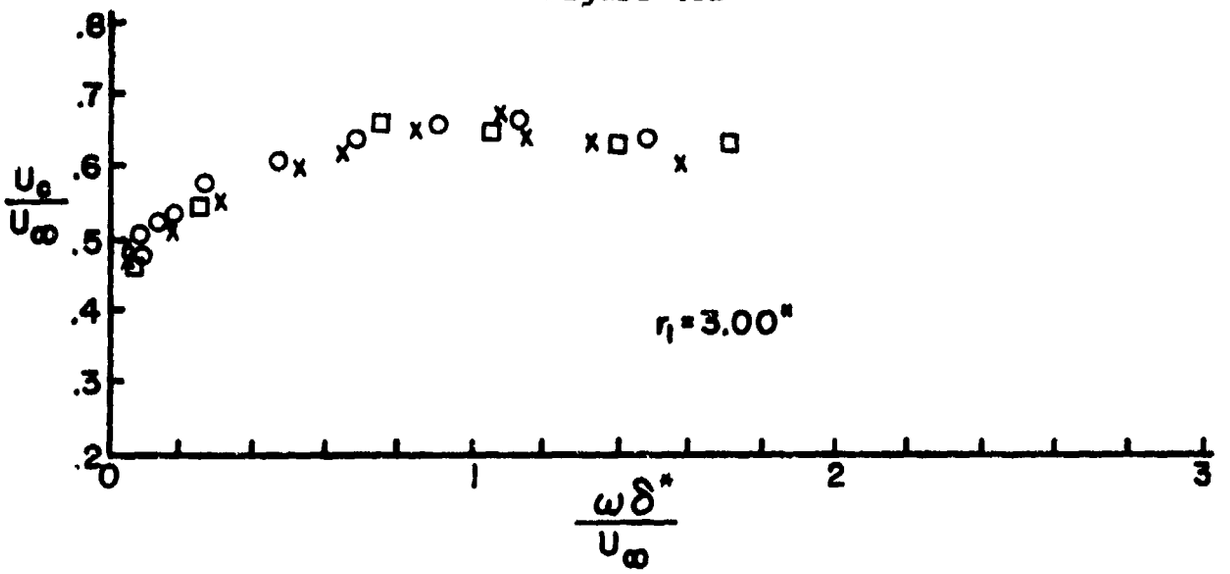

Figure 45c. Narrowband Convection Velocities. Favorable Gradient and Smooth Wall. For an explanation of symbols, see Table 3.

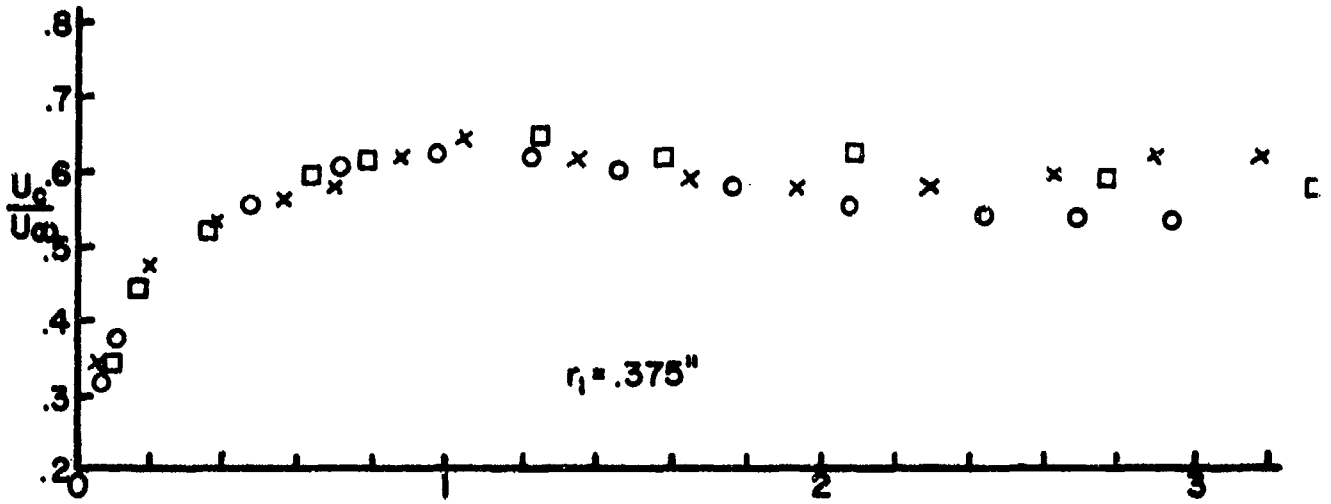

Figure 46a

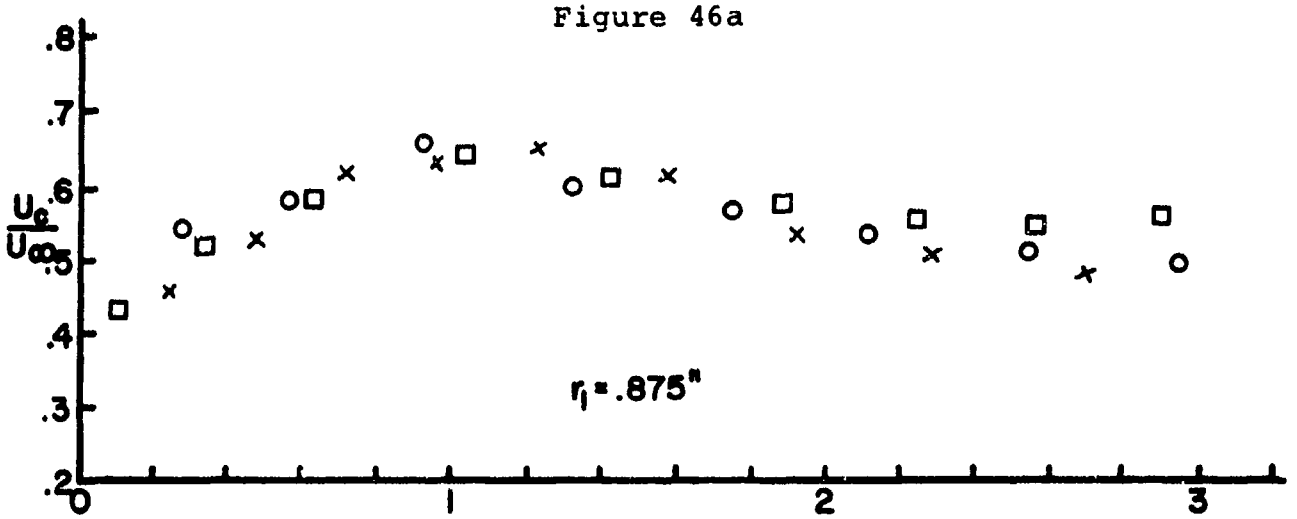

Figure 46b

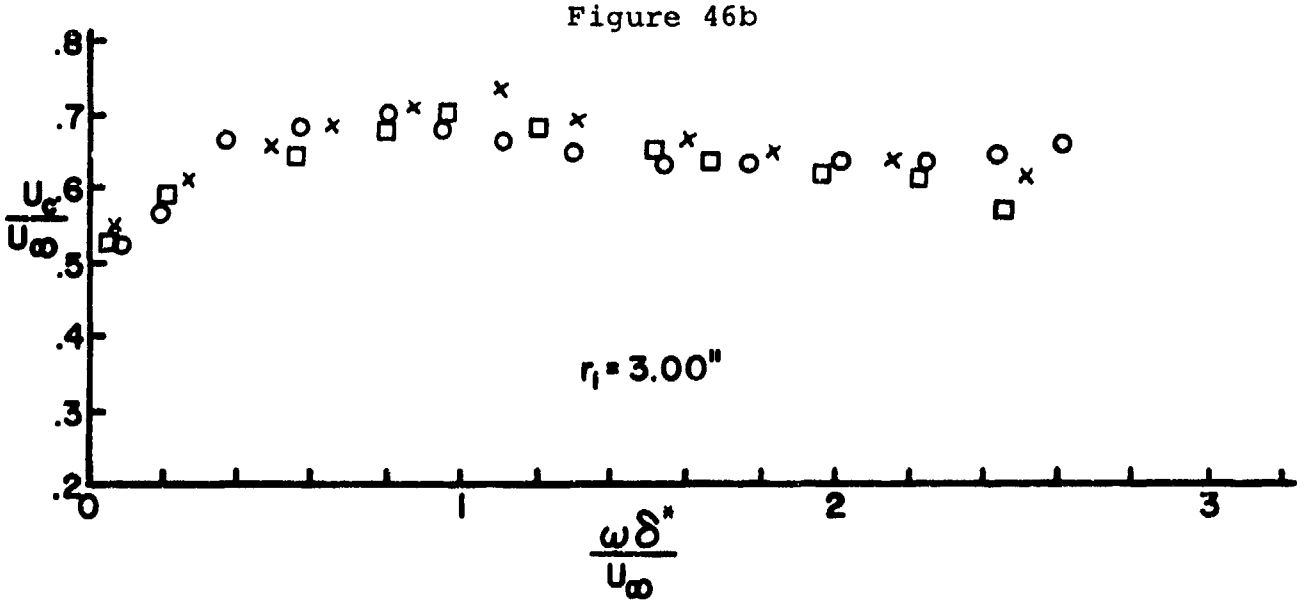

Figure 46c

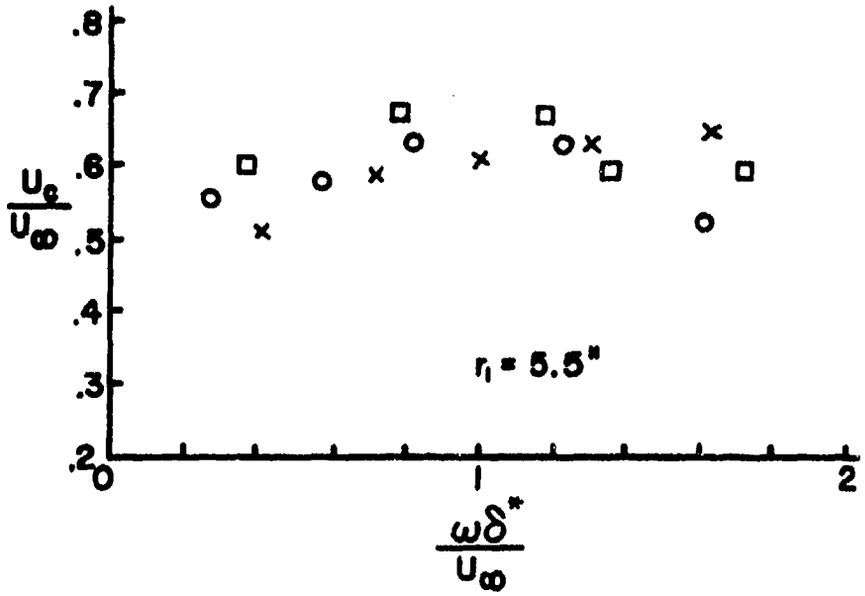

Figure 46d. Narrowband Convection Velocities. Favorable Gradient and Rough Wall. For an explanation of symbols, see Table 3.

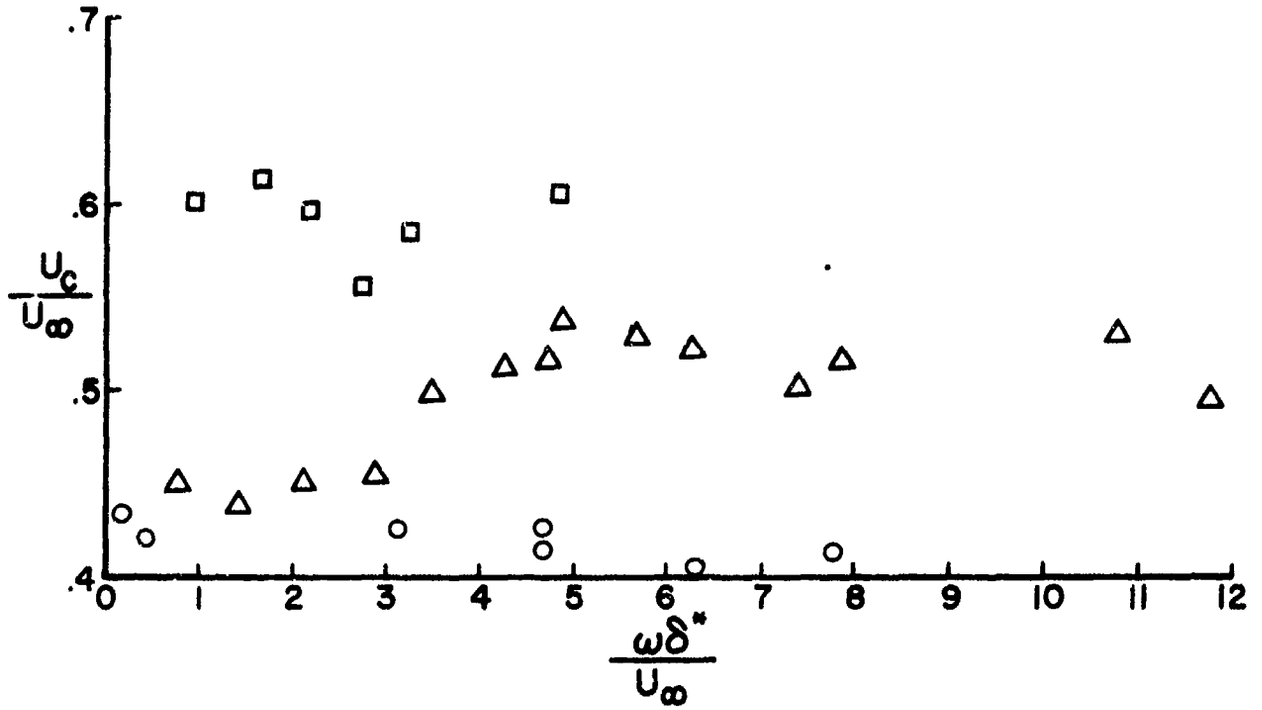

Figure 47a. Narrowband Convection Velocities. Adverse Pressure Gradient and Smooth Wall. $\xi \approx 12$.

○ $\Delta\xi=1.2$ △ $\Delta\xi=4.7$ □ $\Delta\xi=4.7$ (diagonal)

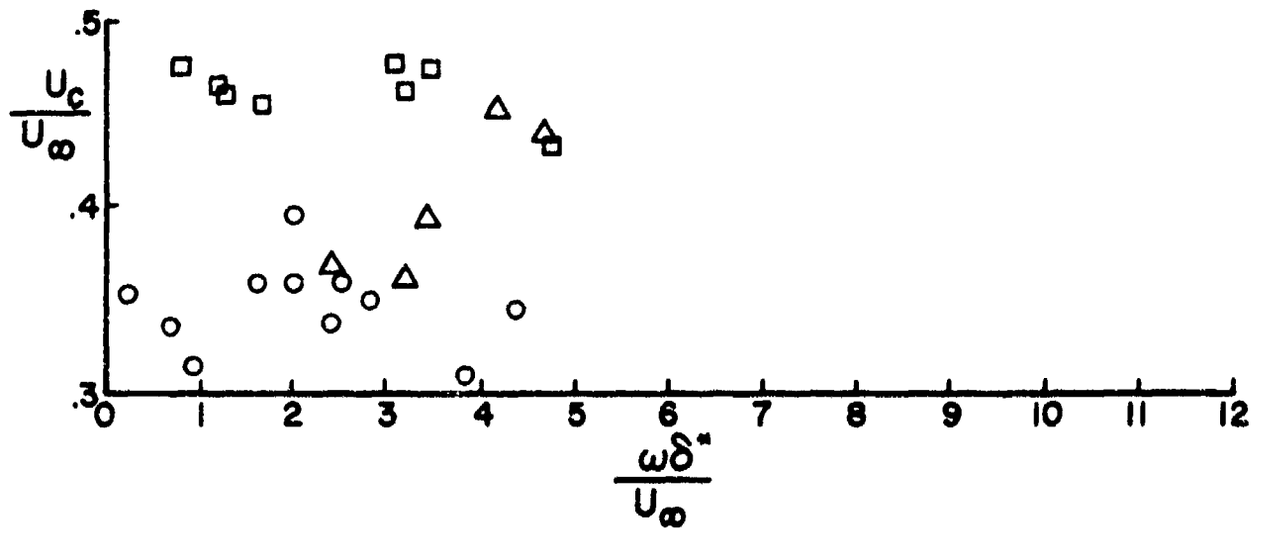

Figure 47b. Narrowband Convection Velocities. Adverse Pressure Gradient and Smooth Wall. $\xi \approx 23$.

○ $\Delta\xi=.68$ △ $\Delta\xi=2.4$ □ $\Delta\xi=2.4$ (diagonal)

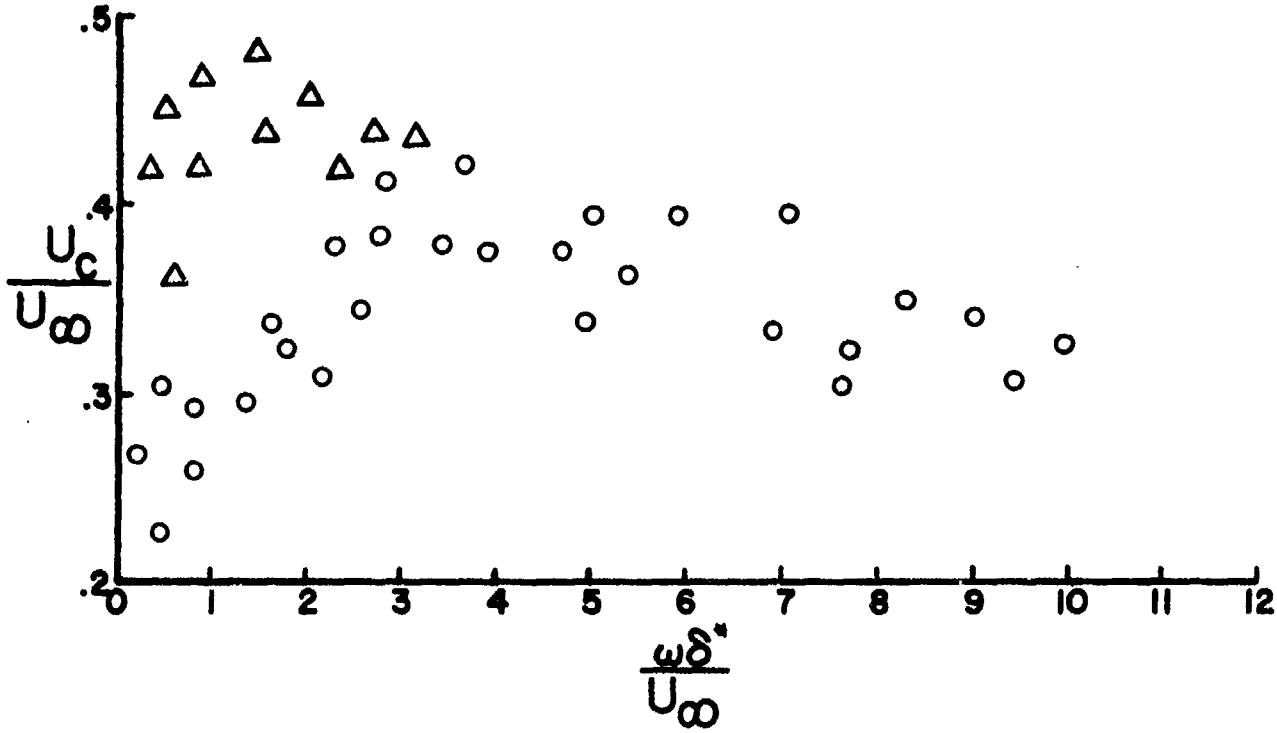

Figure 48. Narrowband Convection Velocities. Adverse Gradient and Rough Walls. $\xi \approx 6$.

O $\Delta\xi = .45$ Δ $\Delta\xi = 1.6$

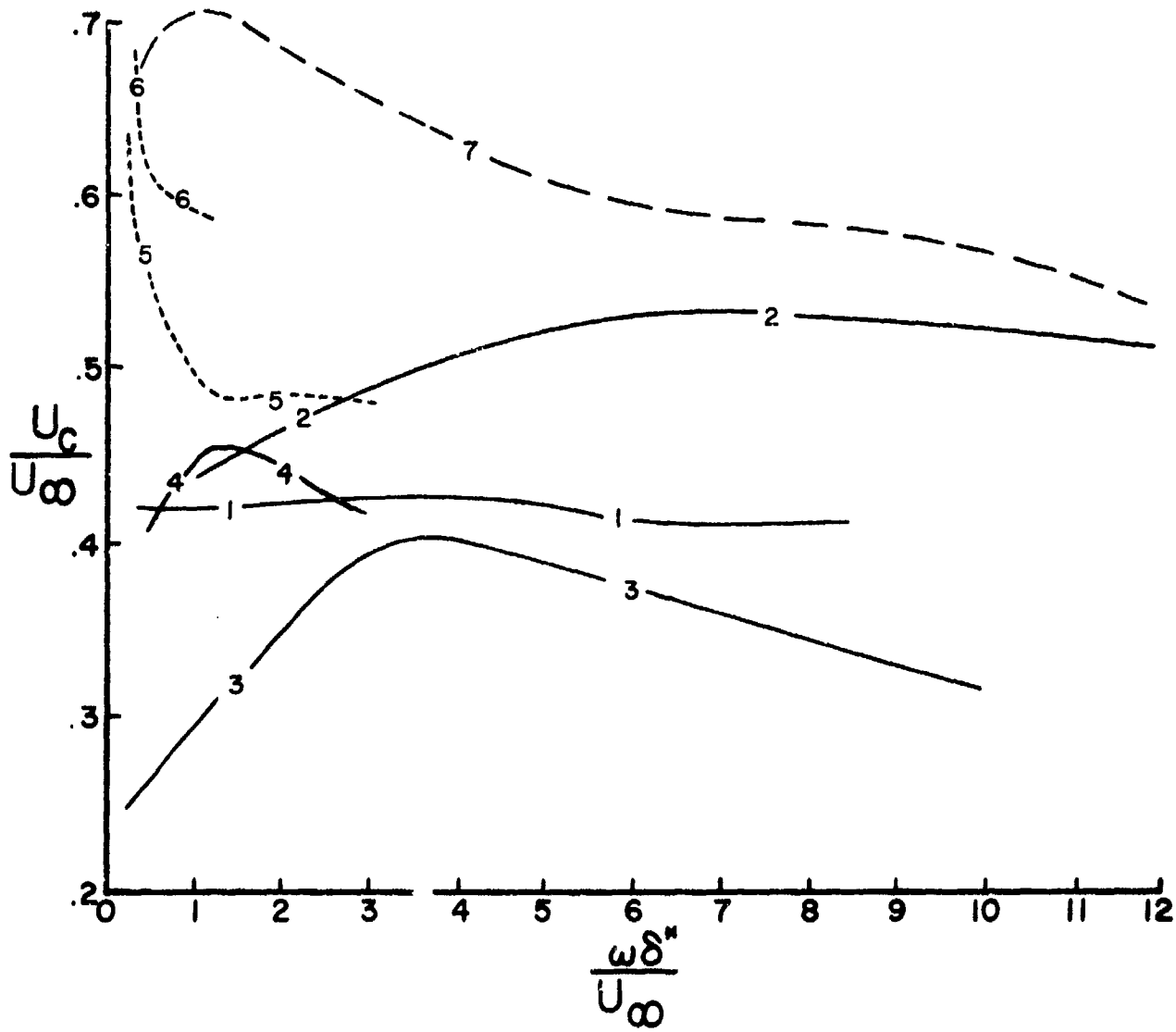

Figure 49. Narrowband Convection Velocities. Adverse Gradient.

(1) smooth wall $\xi \approx 12$, $\Delta\xi = 1.2$
(2) smooth wall $\xi \approx 12$, $\Delta\xi = 4.7$
(3) rough wall $\xi \approx 6$, $\Delta\xi = .45$
(4) rough wall $\xi \approx 6$, $\Delta\xi = 1.6$
(5) smooth wall $\Delta\xi = 1.47$, Schloemer (1966)
(6) smooth wall $\Delta\xi = 5.6$, Schloemer (1966)
(7) smooth wall Bradshaw (1967)

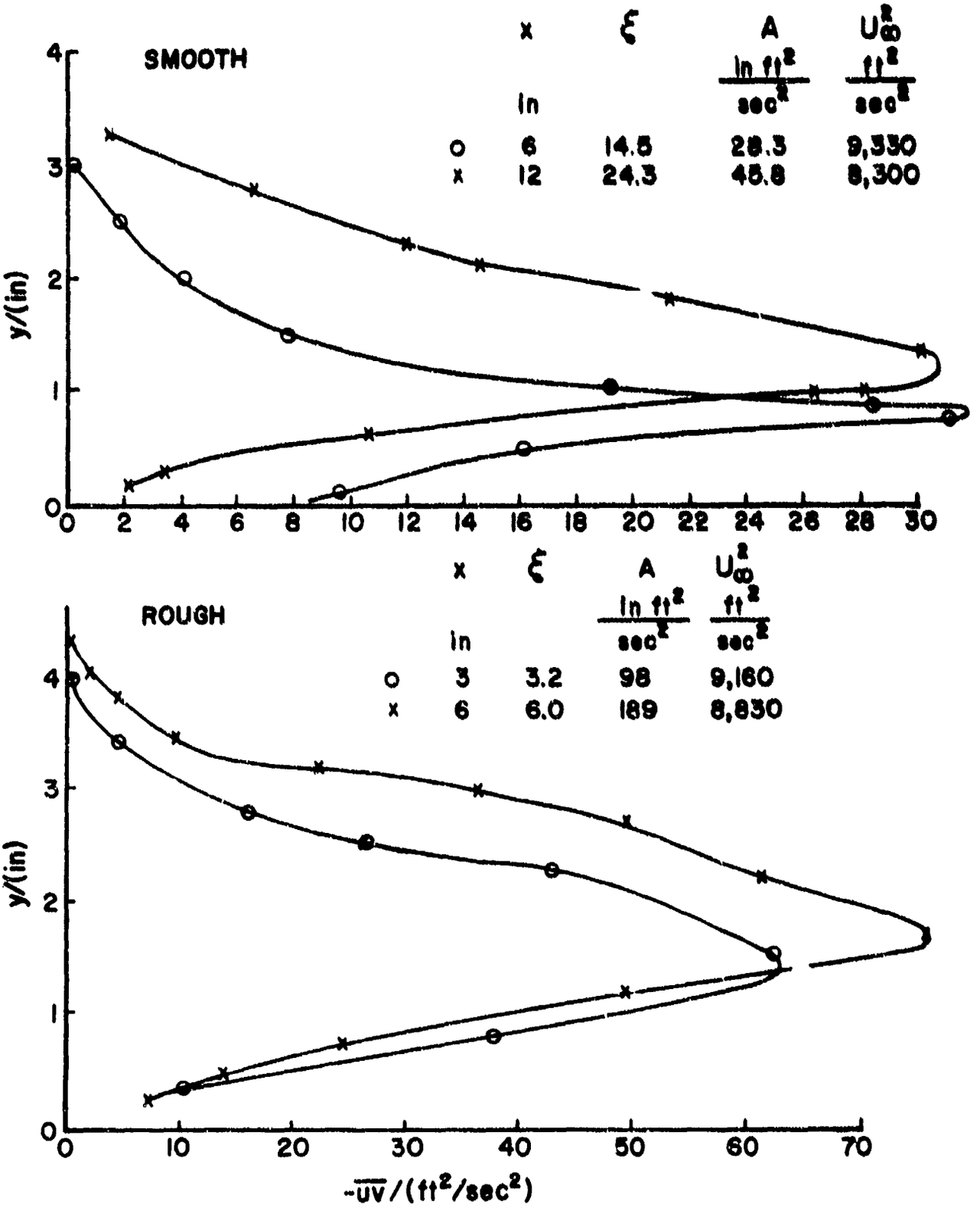

Figure 50. The $\overline{uv}$ product for two adverse gradient flows.